LIGA CAVITY RESONATORS AND FILTERS FOR MICROWAVE AND MILLIMETRE-WAVE APPLICATIONS

A Thesis Submitted to the College of

Graduate Studies and Research

In Partial Fulfillment of the Requirements

For the Degree of Doctor of Philosophy

In the Department of Electrical and Computer Engineering

University of Saskatchewan

Saskatoon

by

Zhen Ma

PERMISSION TO USE

In presenting this thesis in partial fulfilment of the requirements for a Postgraduate degree from the University of Saskatchewan, I agree that the Libraries of this University may make it freely available for inspection. I further agree that permission for copying of this thesis in any manner, in whole or in part, for scholarly purposes may be granted by the professor or professors who supervised my thesis work or, in their absence, by the Head of the Department or the Dean of the College in which my thesis work was done. It is understood that any copying or publication or use of this thesis or parts thereof for financial gain shall not be allowed without my written permission. It is also understood that due recognition shall be given to me and to the University of Saskatchewan in any scholarly use which may be made of any material in my thesis.

Requests for permission to copy or to make other use of material in this thesis in whole or part should be addressed to:

Head of the Department of Electrical and Computer Engineering
University of Saskatchewan
Saskatoon, Saskatchewan, Canada
S7N 5A9

ABSTRACT

High performance microwave cavities for various circuits in the front-end of transceivers such as filters, diplexers, and oscillators have conventionally been built with rectangular or cylindrical metallic waveguides, which typically have low loss, high quality (Q) factor, and higher power handling capability. However, such waveguide cavity based circuits made by traditional metal machining techniques tend to be costly, particularly for complex multiple cavity based circuits, and not well suited to high volume commercial applications and integration with planar microwave integrated circuits. As commercial transceiver applications progress toward higher microwave and millimetre-wave frequencies, the use of waveguide based circuits for compact, highly integrated transceivers is becoming feasible, along with an increasing need for cost effective batch fabrication processes for realizing complex metallic cavity circuits without sacrificing structural quality and performance. It is expected that significant advancements in both microwave performance and integration will be achieved through the development of novel technologies for realizing vertically oriented three-dimensional (3-D) structures.

Although improvement has been made on increasing the resonator Q factor by exploiting silicon micromachining and low-temperature cofired ceramics (LTCC) techniques, there are some drawbacks inherent to silicon cavity micromachining and LTCC technology, including non-vertical sidewalls, depth limitations, and surface roughness for the silicon resonator, and dielectric and radiation loss for LTCC resonator.

Polymer-based fabrication is a promising alternative to silicon etching and LTCC technologies for the batch fabrication of ultra-deep microwave cavity structures. In particular, deep X-ray lithography (XRL), as part of the LIGA process, is a microfabrication technology for precisely structuring polymers, and is increasingly being applied to RF/microwave microstructures. In addition to precise patterning capabilities, deep XRL is able to structure ultra-deep cavities due to the penetration ability of hard X-rays. Cavities of several millimetres are possible in a single lithographic exposure, and with excellent sidewall quality, including verticality near 90 degrees and surface roughness on the order of tens of nanometres. These structured polymers are subsequently used as electroforming templates for fabricating metal structures with correspondingly good sidewall quality.

This thesis investigates the possibility of realizing high-Q cavity resonators and filters at microwave frequencies using the LIGA microfabrication process. Fi-

nite element method (FEM) electromagnetic simulation results based on the cavity models representing different fabrication conditions show that smooth LIGA cavity structures result in promising Q improvement over silicon and LTCC structures. And the potential advantages of LIGA resonators are more dramatic with cavity greater height and increasing operating frequency. Deep polymer cavity structures (1.8 mm) fabricated using deep XRL demonstrate excellent sidewall verticality in the PMMA structure, with only slight shrinkage at the top surface of 8.5 $\pm$ 2.5 μm in either lateral dimensions. This corresponds to sidewalls with verticality between 89.82^o and 89.9^o. The structured polymers are subsequently used as templates for metal electroforming to produce cavity resonators. The performance of the resonator is measured in a planar environment. A RT/duroid^{TM} 6010 soft substrate patterned with coupling structures forms the sixth side, and thus completes the cavity. Despite the rather crude test assembly for the sixth side made by clamping, the measured resonator has a high unloaded Q of 2122.2$\pm$85 at the resonant frequency of 24 GHz, indicating that LIGA cavities are especially promising for high performance applications.

The relatively simple, single-step lithographic exposure also facilitates extension to more structurally complicated waveguide and multiple cavity-based circuits. This research work also proposes a high performance "split-post" 3-pole cylindrical post coupled Chebyshev bandpass filter suitable for LIGA fabrication. In addition to potentially batch fabricating such a filter lithographically by exposing the entire waveguide depth in a single exposure, the filter structures composed of three cavities with metallic multi-post coupling would be extremely difficult to fabricate using traditional machining techniques due to the extremely fine post structure and high vertical aspect ratio required. However, these types of structures could be ideal for LIGA fabrication, which offers sub-micron features, aspect ratios of 100:1 or higher, resist thicknesses of up to 3 mm, and almost vertical and optically smooth sidewalls. Also, representative LIGA sidewall roughness is used to predict very low loss and high performance, suggesting that complicated structures with multiple resonator circuits and high internal components with high aspect ratios are possible.

ACKNOWLEDGEMENTS

I would like to express my sincere appreciation and gratitude to my supervisor, Dr. David M. Klymyshyn, for his guidance, support and encouragement throughout this project and the preparation of this thesis.

I would also like to thank the personnel at the Institute for Microstructure Technology (IMT), Forschungszentrum Karlsruhe in Germany, especially Dr. Sven Achenbach, Dr. Martin Börner, Dr. Timo Mappes, and Dr. Nina Dambrowsky, for all their efforts supporting device fabrication.

I would also like to thank NSERC and TRLabs for providing financial assistance for this project. In addition, I appreciate the support from TRLabs by providing the personnel and facilities. In particular, I wish to express my gratitude to Garth Wells for testing assistance.

Finally, I would like to thank my parents and sister. Without their consistent encouragement and unselfish support at all my difficult times, I would never be able to become current me.

Contents

List of Tables

List of Figures

LIST OF ABBREVIATIONS

2-D	two-dimensional
3-D	three-dimensional
ADS	Advanced Design System
C	capacitor
CPW	coplanar waveguide
dB	decibel
EBG	electromagnetic band-gap
FEM	finite element method
GHz	gigahertz
HFSS	High Frequency Structure Simulator
IC	integrated circuit
IEEE	Institute of Electrical and Electronics Engineers
IMT	Institute for Microstructure Technology
L	inductor
LTCC	low-temperature cofired ceramics
MAN	Metropolitan Area Network
MEMS	microelectromechanical systems
MHz	megahertz
MIC	microwave integrated circuit
mm	millimetre
MMIC	monolithic microwave integrated circuit
nm	nanometre
Q	quality factor

R	resistor
RF	radio frequency
RIE	reactive ion etching
r.m.s	root-mean-square
SEM	scanning electron microscope
SOL	short/open/load
TE	transverse electric
TM	transverse magnetic
μm	micrometre
VNA	vector network analyzer
XRL	X-ray lithography

Chapter 1

INTRODUCTION

1.1 Background

Communication systems at microwave and millimetre-wave frequency bands grew rapidly in recently years as there is high bandwidth available at these frequencies compared to the conventional spectrum. Because of the advantages offered at high frequencies, many broadband wireless communication systems are under development at microwave and millimetre-wave bands, such as Wireless Metropolitan Area Networks (MANs) defined by IEEE Standard 802.16, in which frequencies from 10 to 66 GHz are addressed for the physical layer specification [1].

With the increasing demands for high performance broadband services, the need for low loss and compact size passive devices operating at microwave and millimetre-wave frequencies becomes more critical. One of the most important components for the broadband communication systems is the bandpass filter, which is used in transceivers to reject the unwanted signals and provide isolation between different channels. In order to achieve excellent performance required by such communication systems, bandpass filters constructed with high quality factor (high-Q) resonators are in high demand.

High performance microwave resonators are conventionally built with metallic machined rectangular or cylindrical waveguides, which are characterized by a high quality factor and excellent power handling capacities. However, structures made by metal machining are large in size, and difficult to integrate with planar Microwave Integrated Circuits (MICs). Moreover, with increasing frequency and

as cavity size decreases, it is difficult to maintain small fabrication tolerances and good structural and sidewall surface quality for cavities, particularly with batch fabrication processes required for volume commercial applications. To meet the reduced size and weight requirements for emerging mobile and satellite applications, new techniques for fabricating low loss microwave and millimetre-wave components need to be developed.

1.2 Techniques for Batch Fabrication of Resonators

1.2.1 Silicon Micromachining

Micromachining techniques are often silicon-based manufacturing processes, which include two main approaches: bulk micromachining and surface micromachining.

Bulk micromachining creates 3-D structures in the bulk of a substrate by selective removal of the unwanted substrate material. Bulk micromachining is enabled by the process called etching. Two types of etching approaches are used: anisotropic etching and isotropic etching. Anisotropic etching removes the substrate selectively in certain directions, while isotropic etching removes material in all directions of the substrate. By exploiting one or a combination of etching processes, a wide variety of three-dimensional structures can be sculpted within the confines of the wafer. Furthermore, multiple wafers can be integrated by fusion bonding to build up a stacked structure.

As opposed to the bulk micromachining techniques, which involves material removal in the substrate, surface micromachining is performed by adding thin film material layer by layer on a substrate. The thin film material, which is deposited on the substrate but is removed later to create void space in the depth, is called the sacrificial layer. The material, which forms the free standing microelectromechanical systems (MEMS) structure, is called the structural layer. The 3-D structure is built up by adding and removing structural and sacrificial layers in the right sequence.

1.2.2 LTCC Technology

Multilayer LTCC [2] is one approach for fabricating 3-D circuits and modules with compact size, reduced weight, and relatively high Q. LTCC is a glass-ceramic composite that has low dielectric losses comparable to that of 99% pure alumina, a common high performance microwave dielectric material. The typical metals for LTCC are those with high conductivity, such as gold, copper, and silver. The low loss characteristics of the dielectric and conductors make LTCC a promising technology for high performance applications up to the millimetre-wave frequency range.

The LTCC systems are developed using a dielectric tape provided in rolls and shrinkage-matched metallization pastes. The tape is initially blank. Via holes for conducting between layers are formed in the tape by punching or drilling, and the conductive lines are screen-printed on the tape. Then the printed and punched tape layers are stacked and laminated. By firing the dielectric and conductor together, a fully integrated multilayer component can be obtained. Each layer can be inspected prior to stacking, resulting in high yields and cost effectiveness. Unlike thick-film processes where sequential lamination and firing steps are required, LTCC technology processes all the different layers in a single step, producing minimum distortion and line degradation. Furthermore, LTCC technology allows the integration of all passive circuits without the need of a mechanical mechanism to hold them together, and thus eliminating the air gaps or other discontinuities caused by assembly.

1.2.3 LIGA

LIGA is one of the micro-fabrication techniques to produce miniature 3-D structures. The term LIGA is an acronym for the German terms for Lithography, Electroplating and Moulding. Combining X-ray lithography and electrodeposition was first carried out at IBM in 1975. The modern LIGA process was developed at Nuclear Research Center Karlsruhe in Germany in the 1980's by adding moulding

to the lithography and electroplating [3].

This technique utilizes synchrotron X-ray radiation as the lithographic light source. The extremely short X-ray wavelength, on the order of 0.1-1.0 nanometres (nm), and the high penetration ability arising from transparency of most materials in the X-ray region of the spectrum allows patterning of precise structures in polymer photoresist with feature sizes from tenths of micrometres (μm) to centimetres, and with optical quality sidewall surface roughness (typically 20 to 30 nm). One major advantage of synchrotron lithography over other techniques is the ability to define high resolution images in thick materials up to several millimetres and even centimetres in depth [4]. The resist structure after development could be the end product of the fabrication process, or be used as a template for deposition of metal structures. The pattern created on the resist can also be used to electroplate a mould insert, and the mould insert structure used for mass producing plastic devices by injection moulding or hot embossing.

1.3 Literature Review

As described in Section 1.1, low loss bandpass filters, which are constructed with high Q resonators, are one of the most important components in a wireless communication system. In this section, alternative techniques for implementing high Q factor resonators and filters are investigated.

1.3.1 Membrane Supported Microstrip Transmission Line Resonator

A simple method of resonator realization is to use microstrip structures [5]. However, for the resonators using microstrip lines on conventional substrates, thinner substrates must be used to suppress the higher order substrate modes with increasing frequency. This results in narrow line dimensions for a given impedance, which greatly increases the conductor loss because of the greater surface resistance of narrow microstrip lines [6]. Thus, the resonator Q factor is dramatically reduced.

One way to increase the Q of a resonator is to integrate the resonator using micromachining techniques. Membrane supported microstrip structures can be formed by etching the silicon substrate from beneath using a backside etching process up to a thin dielectric membrane about 1 to 1.5 μm thick supporting the microstrip structures [7]. The thin dielectric membrane has a dielectric constant close to unity. For this membrane supported microstrip structure, the dielectric loss is dramatically reduced by using the air dielectric, and conductor loss is considerably reduced by the wider transmission line geometry. A drawback of the structure is that there is no intrinsic ground plane. This can be overcome by forming a ground plane by adding another micromachined substrate on the top of circuit (see Figure 1.1 [8]). The radiation loss can be reduced by shielding the structure on all sides using thick via grooves. By diminishing the dielectric and conductor losses, a measured resonator unloaded Q factor around 600 at 60 gigahertz (GHz) was reported [8].

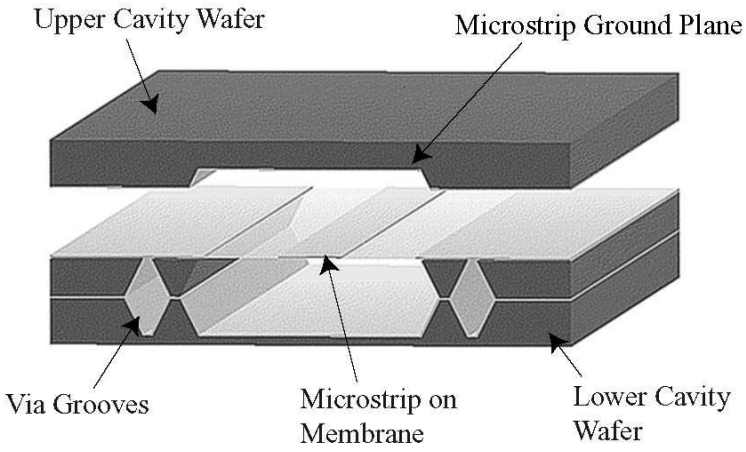

Nguyen, et al., "Micromachined devices for wireless communications," *in Proceedings of the IEEE*, August 1998.

Figure 1.1 Transverse section of the suspended microstrip line [8].

1.3.2 Silicon Micromachined Cavity Resonator

Cavity resonators made by entirely enclosed metallic rectangular or cylindrical waveguides can achieve unloaded Q values as high as thousands because little energy is lost over time [9]. However, conventional waveguide cavity resonators are heavy in weight, large in size, and costly to fabricate. It is difficult to maintain a good fabrication tolerance when the cavities are operating at upper microwave bands due to the small physical dimensions at high frequency. Furthermore, they have traditionally been difficult to integrate with planar microwave circuits prevalent in modern microwave circuit design, and are difficult to fabricate with lithographic batch type processing.

The development of micromachining techniques makes it possible to fabricate miniature cavity components with high precision.

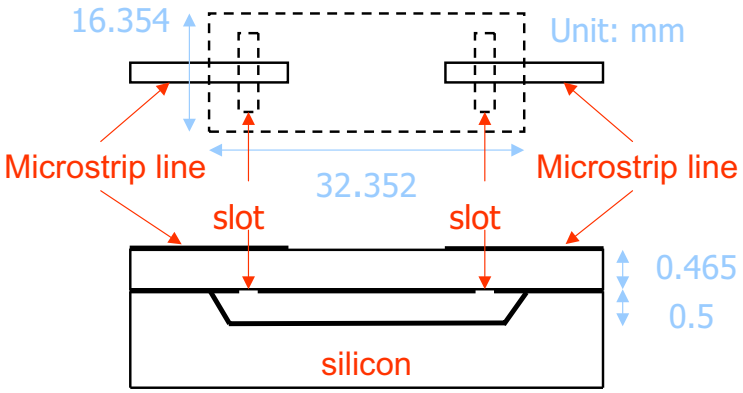

Papapolymerou, et al., "A micromachined high-Q X-band resonator,"
IEEE Microwave and Guided Wave Letters, June 1997.

Figure 1.2 X-band Micromachined cavity resonator [10].

A micromachined resonant cavity was first demonstrated for X-band (10.4 GHz) applications [10]. The structure of the resonator is shown in Figure 1.2 [10]. The cavity was coupled by two microstrip lines via slots in the ground plane of the microstrip lines, which provided an easy way to integrate microwave integrated circuit and monolithic microwave integrated circuit (MMIC) structures. The cavity demonstrated an unloaded Q of 506 with dimensions of 16×32×0.465

millimetres (mm). The cavity was fabricated on a single silicon wafer by using an anisotropic etching process, which results in non-vertical sidewalls at 54.7^o relative to the horizontal plane. This sidewall slope decreases the Q factor compared with perfect rectangular cavities. To achieve higher Q factors, deeper cavities are needed. However, due to the thickness limitation of standard silicon substrates, which is typically 525 μm or 650 μm [11], the cavity fabricated on a single silicon wafer by etching cannot easily be made deeper.

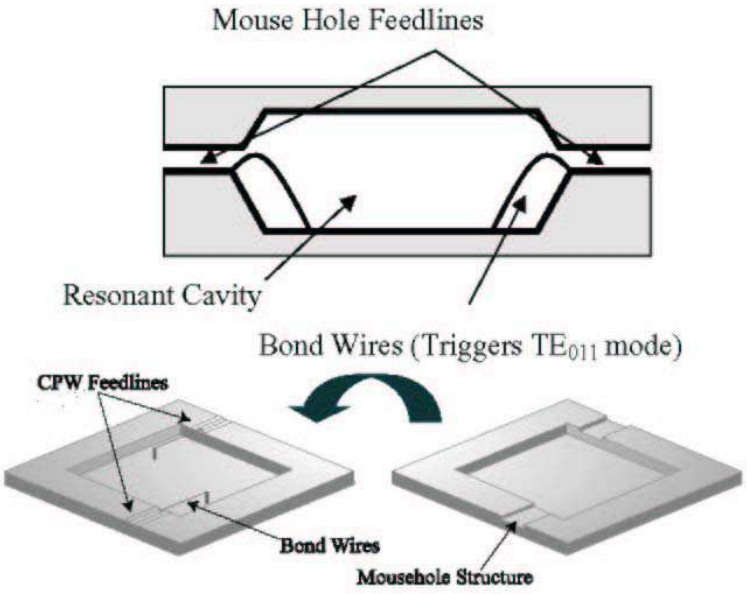

Brown, et al., "Microwave and millimetre-wave high-Q micromachined resonators," *International Journal of RF and Microwave Computer-Aided Engineering*, July 1999.

Figure 1.3 Micromachined cavity resonator formed by a top and a bottom cavities [12].

Several efforts were made to develop new approaches for obtaining higher Q factors. A micromachined cavity structure formed by top and bottom cavities bonded together as shown in Figure 1.3 [12] was presented. A coplanar waveguide (CPW) line was defined on the bottom wafer to the edge of the cavity, and bond wires were placed from the end of the CPW line to the base of the cavity to excite the resonator. With this resonator topology, much higher unloaded quality factors

of 1117 at 24 GHz and 1163 at 38 GHz were achieved due to the double depth of the cavity. Another geometry for obtaining deeper cavities was presented by the utilization of several stacked standard silicon wafers, as shown in Figure 1.4 [13]). The cavity was constructed of five sections of wafers etched from both sides. The five identical wafers were then bonded together using a sodium silicate paste and electroplated with a thin layer of copper. The stacked cavity was fabricated at 30 GHz, and showed an unloaded Q factor of 2155. Although the performance is quite good, this stacking technique presents fabrication challenges that could be problematic, including precise alignment, gaps between wafers, and the "saw-tooth" varying vertical cross section. All of these could lead to higher loss and overall Q factor reduction, especially at higher frequencies and also in realizing more complex multiple resonator based circuits.

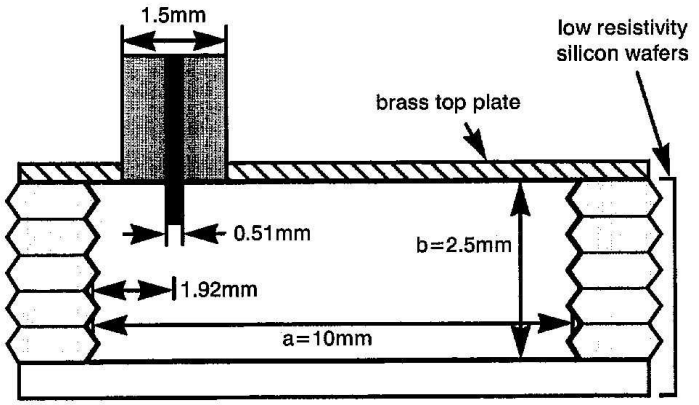

Stickel, et al., "High-Q bulk micromachined silicon cavity resonator at Ka-band," *Electronics Letters*, March 2001.

Figure 1.4 Micromachined cavity formed by several stacked silicon wafers [13].

A cavity structure with more vertical sidewalls was presented in [14] accomplished with the use of deep reactive ion etching (RIE) (Bosch process) technology on a standard silicon wafer. However, this dry anisotropic plasma etching method results in rough sidewall surfaces, which leads to high conductor loss, and therefore, reduced Q at high frequency applications.

1.3.3 LTCC Cavity Resonator

Unlike cavity structures that have solid metal walls built by silicon micromachining process, the LTCC cavity resonators are implemented using rows of metallized via holes as sidewalls. LTCC cavity resonators using rows of stacked vias as sidewalls were realized at Q band [15] and V band [16], respectively. In order to reduce the radiation loss, multiple layers of vias were employed, which results in a larger overall resonator structure than an equivalent metallic cavity resonator. Although the LTCC material has a low loss tangent, the dielectric loss is still the major limiting factor for achieving higher Q. To maximize the Q factor of a LTCC resonator, an enhanced resonator structure with an air cavity inside it was proposed in [15]. With the total cavity height of 0.7 mm, which was formed by seven LTCC layers of 100 μm each, an unloaded Q of 1200 was obtained at 19.8 GHz.

The LTCC technique was also employed to improve resonator compactness at 42.6 GHz, which was realized by adding a capacitive post in the middle of the cavity [17]. Simulation results showed 52% size reduction by employing capacitive loading techniques, at the expense of Q reduction by 20% compared to the unloaded cavity operating at the same frequency.

1.3.4 Cavity Filter

As an extension of the planar integrated cavity resonator concept, bandpass filters employing the silicon micromachined and LTCC cavities as the building blocks were investigated.

A vertically integrated bandpass filter structure was presented in [18]. The 10 GHz filter consists of three 500 μm thick vertically integrated resonant cavities, which are etched in silicon using wet chemical anisotropic etching, and are coupled by thin slots etched in 100-μm silicon wafers. Another application of a silicon micromachined resonant cavity was demonstrated in [14], which is a four-pole linear phase filter operating at 27 GHz, consisted of four horizontally integrated

resonators placed side by side and coupled by evanescent waveguide sections. In order to achieve higher Q, a deep RIE etching process was used to provide more vertical sidewalls, and two 500-μm wafers are stacked to create the 1-mm-high micromachined cavities.

In addition to the silicon micromachining method, LTCC technique has also been applied to produce 3-D cavity filters. Low-loss two-pole filters based on capacitive loaded cavities were reported at Q band [17]. Narrow-band two-pole filters, which can be embedded inside packaging, were implemented in LTCC by employing capacitive loading techniques at X-band [19]. A three-pole bandpass filter using LTCC technology was demonstrated in [16] for 60 GHz wireless local area network narrow-band applications.

1.4 Research Objectives

Although improvement has been made on increasing the resonator Q factor by exploiting silicon micromachining and LTCC techniques, there are some drawbacks inherent to silicon cavity micromachining and LTCC technology, including non-vertical sidewalls, depth limitations, and surface roughness for silicon resonators, and dielectric and radiation loss for LTCC resonators. These can potentially be overcome by non-silicon based micro-fabrication techniques.

The LIGA fabrication process is different from the silicon and LTCC techniques. Highly vertical cavities with solid metal sidewalls having verticality better than 89.9^o are possible. The sidewalls of the LIGA structures exhibit optical planarity with surface roughness of about 20 to 30 nm. These low undulations on the interior surface of the cavity walls are transferred to the conductor surface during metallization. The current, concentrated in the metal surface on the inside cavity walls due to the skin depth effect, follows the uneven surface of the cavity, which increases the conductor loss compared to the case of a perfectly smooth surface [6]. As the surface roughness increases, the current encounters greater resistance, and therefore, the conductor loss increases. The optical quality surface roughness of

LIGA products minimizes the conductor loss effectively, and makes high quality factor resonators possible. The materials of the final products are not confined to silicon. LIGA offers the potential of manufacturing microstructures with a variety of materials such as polymers and plastics, as well as metals. The most important feature of the LIGA process is that deep rectangular cavities with height up to several millimetres can be obtained, which increases the Q factor dramatically. Furthermore, batch fabrication with potentially low cost could be realized using LIGA replication techniques. A metal structure produced by the LIGA process can serve as a mould insert. For mass production, moulding techniques such as hot embossing and injection moulding are employed to produce plastic devices without going back to the expensive lithography step.

The advantages that LIGA offers allow the development of new microwave and millimetre-wave circuits. By exploiting the metal height, new 3-D planar transmission line structures can be realized using LIGA fabrication techniques [20] [21]. LIGA - micromachined transmission lines offer several advantages over conventional structures in microwave and millimetre-wave applications. The tall metal transmission lines provide high power handing capacity when bonded by a good thermal conductor due to the increased conduction interface. The high aspect conductor sidewalls and nearly perfect slope results in very high coupling levels that are impossible to obtain with conventional planar integrated transmission lines. Employing the advantages of 3-D transmission line structures, microwave and millimetre-wave circuits requiring very high coupling have been developed, such as stepped-impedance low-pass filters [20] [21], coupled-line bandpass filters [20] [21] [22] [23], a 6-dB CPW coupler [23], and a 3-dB CPW coupler [24].

This research is aimed at the investigation of the feasibility of developing high performance cavity resonators and filters using the LIGA fabrication process. The main objectives of the research are summarized as follows:

1. Investigate the advantage of realizing high Q cavity resonators using the LIGA technique over silicon micromachining and LTCC techniques.

2. Design one-port rectangular cavity resonator structures suitable for LIGA implementation at upper microwave and millimetre-wave frequencies, such as 24 GHz and 37 GHz.

3. Fabricate the resonators, which involves creating the suitable layout of the mask for LIGA cavities, a top substrate, and the assembly of the resonators.

4. Test the resonators and determine the unloaded Q, and compare with the simulation results.

5. Investigate the feasibility of realizing high performance filters as an extension of the LIGA cavity concept.

1.5 Thesis Organization

The thesis is organized into seven chapters.

In Chapter 2, resonator basics, which establishes the theoretical background for the design are discussed. The characteristics of the resonators are presented by the lumped RLC resonator models. The properties of rectangular waveguide cavities, a form of implementation of resonator circuits at microwave frequencies, are discussed. Also, typical coupling techniques used to excite the fields inside the cavity are illustrated.

Chapter 3 presents the software and techniques used to design, model, and evaluate the resonator and filter structures presented in this thesis work. A brief introduction is given to the two commercially available simulation tools, Ansoft High Frequency Structure Simulator (HFSS) and QZERO, employed to analyze the performance of the resonator. The additional power dissipation in the conductor due to the surface roughness is approximated by an equation assuming equilateral triangular surface grooves, which will be used to analyze the surface roughness effect on the performance of the circuit models presented in the later designs.

Chapter 4 investigates the properties of the rectangular resonant cavity, including both hollow cavity and dielectric-filled cavity. Cavity models representing

available fabrication techniques, such as silicon machining, LTCC, and LIGA technologies, are simulated. Based on these results, a completed one-port resonator suitable for LIGA fabrication is proposed and simulated using HFSS.

In Chapter 5, the steps taken in the fabrication of resonant cavities using the LIGA technique are demonstrated. A 1800 μm deep metal cavity fabricated using the LIGA process is presented. The cavity has an impressive structure, including extremely vertical and smooth sidewalls, resulting in low conductor loss. A high unloaded Q of 2122$\pm$85 is measured at the resonant frequency of 23.892 GHz. Also, the possible reasons for the discrepancy between the HFSS simulated and measured results are discussed.

Chapter 6 presents a narrow band microwave filter suitable for LIGA fabrication, as an extension of the LIGA cavity concept. The simulation results from the HFSS model incorporating the practical fabrication tolerances measured from a LIGA fabricated PMMA resonator structure suggest that LIGA fabrication introduces only minor deterioration and high performance microwave filters with deep cavities are possible in a single lithography exposure process.

In Chapter 7, conclusions of this research are presented and future research directives are suggested.

Chapter 2

MICROWAVE RESONATORS

Resonators are circuits that allows the exchange of electric and magnetic energies with low loss. Resonators can be of either lumped or distributed. Lumped elements such as resistors, inductors, and capacitors are usually employed for resonators at frequencies below 300 Megahertz (MHz) [25]. At higher frequencies, the dimensions of the general lumped elements are comparable to the wavelength in size. Smaller devices are possible to fabricate with the advantage of integrated circuit (IC) technology. But small sizes result in poor power handling capacity. Therefore, resonators consisting of distributed components are usually constructed for applications in the microwave frequency range.

Distributed resonator circuits utilize the resonant properties of standing waves, and thus are generally of a size comparable to wavelength. Microstrip and cavity resonators are commonly used at microwave frequencies. Although lumped circuits are not generally applicable at high frequencies, they are good models to present the basic operation of resonators.

2.1 Lumped Resonant Circuits

The circuit theory of distributed microwave resonators is similar to that of the resistor (R), inductor (L), capacitor (C) lumped element resonators. At frequencies near resonance, microwave resonators can be modelled by series or parallel RLC resonators. A parallel RLC lumped element resonator circuit is shown in Figure 2.1. In this configuration, lumped elements R, L, and C share a

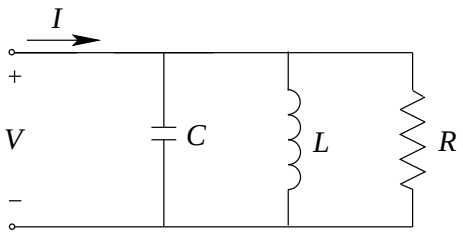

Figure 2.1 Parallel resonant circuit.

common voltage V. The magnetic energy, W_m, is stored in the inductor L. The electric energy, W_e, is stored in the capacitor C. The only power absorptive device is the resistor R, and the average dissipated power by R can be expressed as

$$P_l = \frac{1}{2}\frac{|V|^2}{R}. \tag{2.1}$$

At resonance the input impedance is purely real and equal to R. From the point of view of energy exchange, resonance occurs when the stored average magnetic and electric energies are equal, namely $W_m = W_e$. The frequency at which the resonance appears is referred to as resonant frequency ω_0, which is defined as

$$\omega_0 = \frac{1}{\sqrt{LC}}. \tag{2.2}$$

An important parameter of a resonant circuit is its quality factor, Q. Q is defined as the ratio of stored energy to dissipated energy per cycle. Q is a dimensionless number. At resonance, Q can be expressed in terms of the energy ratio for lumped element resonators as well as microwave resonators as [5]

$$Q = \omega_0 \frac{W_m + W_e}{P_l}, \tag{2.3}$$

where ω_0 is the resonant frequency in radians. For the parallel resonant circuit, Q can be evaluated in terms of the lumped element values as

$$Q = \omega_0 RC = \frac{R}{\omega_0 L}. \tag{2.4}$$

Q is a measurement of loss of a resonator circuit: higher Q implies lower loss.

The input impedance of the parallel resonant circuit is

$$Z_{in} = \left(\frac{1}{R} + \frac{1}{j\omega L} + j\omega C \right)^{-1} . \tag{2.5}$$

Near resonance, the frequency can be represented by a small deviation from ω_0 as

$$\omega = \omega_0 + \Delta\omega, \tag{2.6}$$

where $|\Delta\omega| \ll \omega_0$. Using the Taylor expansion around ω_0, the following expression can be simplified as

$$\begin{aligned} \frac{1}{\omega_0 + \Delta\omega} &= \frac{1}{\omega_0} \cdot \frac{1}{1 + \dfrac{\Delta\omega}{\omega_0}} \\ &= \frac{1}{\omega_0} \left(1 - \frac{\Delta\omega}{\omega_0} \right) . \end{aligned} \tag{2.7}$$

Then by using Equations 2.6 and 2.7 in Equation 2.5, the input impedance can be written as

$$\begin{aligned} Z_{in} &= \left(\frac{1}{R} + \frac{1 - \Delta\omega/\omega_0}{j\omega_0 L} + j\omega_0 C + j\Delta\omega C \right)^{-1} \\ &\simeq \left(\frac{1}{R} + j\frac{\Delta\omega}{\omega_0^2 L} + j\Delta\omega C \right)^{-1} \\ &= \left(\frac{1}{R} + 2j\Delta\omega C \right)^{-1} \\ &= \frac{R}{1 + 2j\Delta\omega RC} \\ &= \frac{R}{1 + 2jQ\dfrac{\Delta\omega}{\omega_0}} , \end{aligned} \tag{2.8}$$

since $\omega_0^2 = \frac{1}{LC}$ and $Q = \omega_0 RC$.

The Q given by Equations 2.3 and 2.4 represents the resonant circuit itself, and is called unloaded quality factor Q_u. Q_u involves the power loss by the resonant circuit only. In practice, a resonant circuit is coupled to external circuitry, which absorbs additional power denoted by P_{ext}. The external Q factor, Q_{ext}, is defined in terms of power dissipated in the external circuit as

$$Q_{ext} = \omega_0 \frac{W_m + W_e}{P_{ext}}. \tag{2.9}$$

Similarly, the Q factor of the loaded resonator, Q_l, associated with the total loss can be expressed as

$$Q_l = \omega_0 \frac{W_m + W_e}{P_l + P_{ext}}. \tag{2.10}$$

In view of Equation 2.10, the effect of the external circuitry always lowers the overall Q factor of a resonator.

The definitions of quality factors in Equations 2.3, 2.9, and 2.10 show the relationship

$$\frac{1}{Q_l} = \frac{1}{Q_u} + \frac{1}{Q_{ext}}. \tag{2.11}$$

The degree of coupling between the external circuit and the resonant circuit is measured by the coupling coefficient k. In general, k can be defined in terms of the Q factor as [5]

$$k = \frac{Q_u}{Q_{ext}} \quad \text{or} \quad k = \frac{Q_u - Q_l}{Q_l}. \tag{2.12}$$

The coupling coefficient k denotes the ratio of the power dissipated in the external circuit to the power loss in the resonant circuit itself. The condition of $k = 1$ is referred to as critical coupling. If k is greater than unity, the resonator is said to be over coupled, while $k < 1$ is called under coupled.

2.2 Cavity Resonator

Cavity resonators are constructed from closed sections of waveguide. A rectangular cavity resonator is usually formed by a waveguide shorted at both ends

by grounded conducting plates. The cavity can be air or dielectric filled volume in three dimensions, which is totally enclosed by metallic walls. The electric and magnetic energy is stored within the volume of the cavity. Power can be dissipated in the metallic walls due to the finite conductivity, as well as in the dielectric filling material. Cavity resonators are attractive at frequencies beyond 3 GHz since they are capable of providing Q values of 5000 or more [25].

2.2.1 Rectangular Waveguide

It is necessary to transfer electromagnetic signal power from one point to another with low propagation loss. A variety of structures can guide the electromagnetic waves to propagate from place to place, such as two-wire lines, coaxial cables, and waveguides.

At higher microwave frequencies, especially at wavelength below 10 cm, waveguides are preferred for applications requiring very low power loss. Waveguides with rectangular or circular cross sections are commonly used geometries. Rectangular waveguide is by far the most widely used type in comparison with circular waveguide.

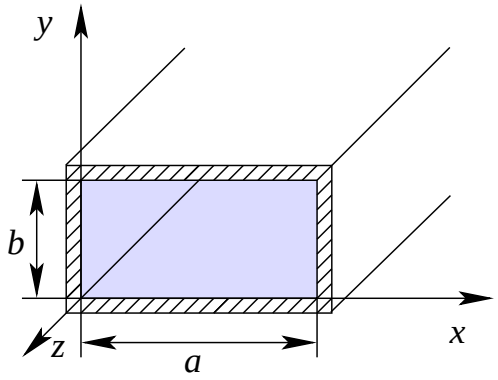

Figure 2.2 Geometry of a rectangular waveguide.

The geometry of a rectangular waveguide is shown in Figure 2.2, with width a and height b. It is assumed that the guide is filled with a material of permittivity ϵ and permeability μ. The rectangular waveguide supports transverse electric (TE) waves and transverse magnetic (TM) waves. In TE waves, the electric field is

entirely transverse, but the magnetic field is not. In TM waves, the magnetic field has no axial component, but the electric field has.

The field components of the TE modes, which are characterized by fields with $E_z = 0$, can be found by solving the wave equations applicable to the longitudinal magnetic field component H_z. The partial differential equation can be solved by the method of separation of variables and applying the boundary conditions that the electric field components tangential to the waveguide walls are zero, and the solution for H_z is found to be [5]

$$H_z(x, y, z) = A_{mn} \cos \frac{m\pi x}{a} \cos \frac{n\pi y}{b} e^{-j\beta z}, \quad (m, n = 0, 1, 2, ..., but not both 0.) \tag{2.13}$$

where A_{mn} is an arbitrary amplitude constant representing the maximum magnitude of the magnetic field intensity, and m and n are arbitrary integers.

Then the transverse field components can be derived as

$$\begin{aligned}
E_x &= \frac{-j\omega\mu}{k_c^2} \frac{\partial H_z}{\partial y} \\
&= \frac{j\omega\mu n\pi}{k_c^2 b} A_{mn} \cos \frac{m\pi x}{a} \sin \frac{n\pi y}{b} e^{-j\beta z}, && \text{(2.14a)} \\
E_y &= \frac{j\omega\mu}{k_c^2} \frac{\partial H_z}{\partial x} \\
&= \frac{-j\omega\mu m\pi}{k_c^2 a} A_{mn} \sin \frac{m\pi x}{a} \cos \frac{n\pi y}{b} e^{-j\beta z}, && \text{(2.14b)} \\
H_x &= \frac{-j\beta}{k_c^2} \frac{\partial H_z}{\partial x} \\
&= \frac{j\beta m\pi}{k_c^2 a} A_{mn} \sin \frac{m\pi x}{a} \cos \frac{n\pi y}{b} e^{-j\beta z}, && \text{(2.14c)} \\
H_y &= \frac{-j\beta}{k_c^2} \frac{\partial H_z}{\partial y} \\
&= \frac{j\beta n\pi}{k_c^2 b} A_{mn} \cos \frac{m\pi x}{a} \sin \frac{n\pi y}{b} e^{-j\beta z}. && \text{(2.14d)}
\end{aligned}$$

The parameters k, k_c, and β in the expression of the the field components can

be calculated by

$$k = \omega\sqrt{\mu\epsilon}\ , \tag{2.15}$$

$$k_c = \sqrt{\left(\frac{m\pi}{a}\right)^2 + \left(\frac{n\pi}{b}\right)^2}\ , \tag{2.16}$$

$$\beta = \sqrt{k^2 - k_c^2}\ . \tag{2.17}$$

The description of the theoretical parameters used in the equations above is summarized in Table 2.1.

Table 2.1 Description of theoretical parameters for TE mode.

Name	**Description**
E_x	x component of electric field
E_y	y component of electric field
H_x	x component of magnetic field
H_y	y component of magnetic field
H_z	z component of magnetic field
a, b	Waveguide width, height
m, n	Eigenvalues, corresponding to propagation modes
ω	Operating frequency in rad/s
k	Free-space wave number
β	Propagation constant
k_c	Cutoff wave number

In view of Equations 2.13 and 2.14a to 2.14d, there are infinite possible solutions for TE waves identified by the two integer subscripts m and n. Correspondingly, infinite propagating modes TE_{mn} defined by the combination of m and n can exist in rectangular waveguide. Each mode has a cutoff frequency $f_{c_{mn}}$, above which the mode can propagate along the waveguide, and below which the mode can not propagate. The mode with the lowest cutoff frequency is called the dominant mode. Cutoff frequency is a geometrical dependent parameter. The cutoff frequency associated with the cross section configuration a and b is where

$k = k_c$, or

$$f_{c_{mn}} = \frac{1}{2\pi\sqrt{\mu\epsilon}}\sqrt{\left(\frac{m\pi}{a}\right)^2 + \left(\frac{n\pi}{b}\right)^2} \ . \tag{2.18}$$

The guide wavelength λ_g, which is defined as the distance between the equal phase planes along the waveguide, is given by

$$\lambda_g = \frac{2\pi}{\beta} = \frac{\lambda_0}{\sqrt{1-(f_c/f)^2}} \ , \tag{2.19}$$

λ_g is bigger than λ_0, which is the wavelength of the plane wave in free-space with frequency f. The guide wavelength is also geometrically dependent, since it is determined by the cutoff frequency in Equation 2.18.

Dominant TE_{10} Mode

Assuming $a > b$, the lowest cutoff frequency occurs for the TE_{10} mode with $m = 1$ and $n = 0$. Thus the TE_{10} mode is the dominant mode of the rectangular waveguide. The cutoff frequency $f_{c_{10}}$ and the guide wavelength λ_g are found, according to Equations 2.18 and 2.19, to be

$$f_{c_{10}} = \frac{1}{2a\sqrt{\mu\epsilon}} \ , \tag{2.20}$$

$$\lambda_g = \frac{\lambda_0}{\sqrt{1-(\lambda_0/2a)^2}} \ . \tag{2.21}$$

The expressions of electric and magnetic field components for TE_{10} mode can be derived by setting $m = 1$ and $n = 0$ in Equations from 2.13 to 2.14d. It is noted that no field components vary in the y direction since n equals zero. Electric and magnetic field patterns are sketched in Figure 2.3. The solid lines represent the electric field, and the dashed lines represent magnetic fields. Field component intensity variation along the x coordinate is shown in Figure 2.4. Component E_y is the only electric field component for the TE_{10} propagation mode. E_y intensity variation follows a half-sine curve, and reaches the maximum at the waveguide center, and is zero at the conducting walls. The magnetic field lines form closed

circles in the horizonal planes of the guide. The transverse magnetic component H_x shares the same intensity variation characteristic as E_y along the x direction, with maximum at the center and zero at the side walls. The longitudinal magnetic component H_z, on the contrary, is a maximum at the side walls and zero at the center. The field pattern repeats itself every half guide wavelength ($\lambda_g/2$) along the propagation direction in rectangular waveguide, but is reversed.

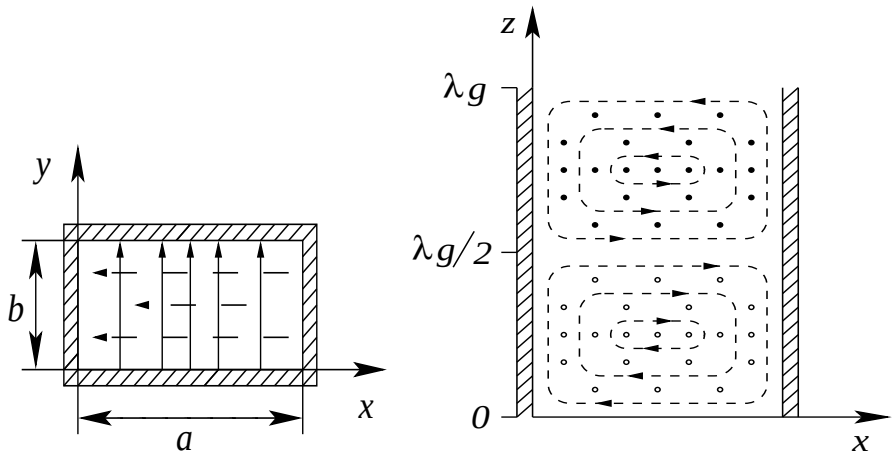

(a) Transverse plane; (b) Top view.

Figure 2.3 Field lines for TE_{10} mode of a rectangular waveguide. Solid lines represent the electric field and dashed, magnetic.

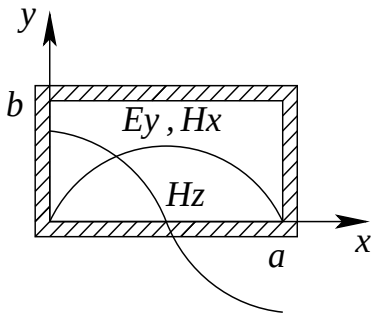

Figure 2.4 Field component intensity along x coordinate for TE_{10} mode in the rectangular waveguide.

2.2.2 Rectangular Resonant Cavity Basics

A resonant structure can be constructed by terminating a section of rectangular waveguide in short circuits at $z = 0$ and $z = d$, as shown in Figure 2.5. The incident and reflected travelling waves superpose on one another to produce standing waves in the rectangular cavity. The length of the cavity is required to be a multiple of a half guide wavelength at the resonant frequency in order to satisfy the boundary conditions of $E_x = E_y = 0$ on the end walls at $z = 0$ and $z = d$.

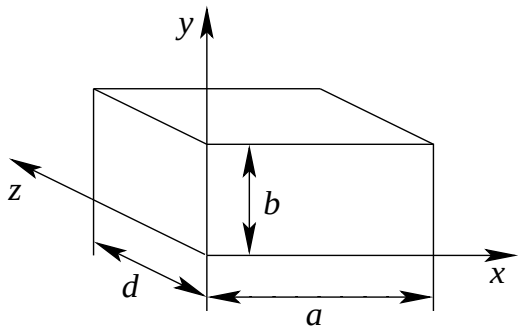

Figure 2.5 A rectangular resonant cavity.

According to Equation 2.13, the general form of longitudinal magnetic field of the TE_{mn} rectangular waveguide mode can be expressed by the superposition of forward and backward travelling waves as

$$H_z(x, y, z) = \cos\frac{m\pi x}{a}\cos\frac{n\pi y}{b}(C^+e^{-j\beta z} + C^-e^{j\beta z}), \tag{2.22}$$

where C^+ and C^- are arbitrary amplitudes of the forward and backward travelling waves. By applying the boundary conditions that $H_z = 0$ at $z = 0$ and $z = d$, the solution of H_z is found to be

$$H_z(x, y, z) = H_0\cos\frac{m\pi x}{a}\cos\frac{n\pi y}{b}\sin\frac{l\pi z}{d}, \tag{2.23}$$

and the resonant frequency of TE_{mnl} mode for the rectangular cavity shown in

Figure 2.5 is given by [5]

$$f_{mnl} = \frac{c}{2\pi\sqrt{\mu_r \epsilon_r}} \sqrt{\left(\frac{m\pi}{a}\right)^2 + \left(\frac{n\pi}{b}\right)^2 + \left(\frac{l\pi}{d}\right)^2} \quad (m, n = 0, 1, 2, \ldots \; ; \; l = 1, 2, 3, \ldots), \tag{2.24}$$

where μ_r and ϵ_r are the relative permeability and permittivity of the material filling in the volume of the cavity; c is the velocity of light in free-space with the value $c = 3 \times 10^8$ m/s. The subscripts m, n, and l represent the number of half-sine periods in the standing wave pattern along x, y and z axes, respectively.

An infinite number of resonant modes can exist in a cavity with fixed shape and size corresponding to the different field distributions determined by the triple combination of m, n, and l. For $b \leq a < d$, the dominant resonant mode with lowest resonant frequency is TE_{101} mode. The total fields for TE_{101} resonant mode are found by substituting Equation 2.23 into Equations 2.14a to 2.14c, and can be written as

$$E_y = \frac{-j\omega\mu a}{\pi} H_0 \sin\frac{\pi x}{a} \sin\frac{\pi z}{d} \; , \tag{2.25a}$$

$$H_x = \frac{-a}{d} H_0 \sin\frac{\pi x}{a} \cos\frac{\pi z}{d} \; , \tag{2.25b}$$

$$H_z = H_0 \cos\frac{\pi x}{a} \sin\frac{\pi z}{d}. \tag{2.25c}$$

The field distribution of TE_{101} resonant mode is similar to those shown in Figure 2.3, if shorting plates are placed at $z = 0$ and $z = \lambda_g/2$, since TE_{101} resonant mode corresponds to TE_{10} waveguide mode in a shorted guide with length of $z = \lambda_g/2$.

In general, the average stored electric and magnetic energies in a volume V are given by [5]

$$W_e = \frac{\epsilon}{4} \int_V \overline{E} \cdot \overline{E}^* dv \; , \tag{2.26a}$$

$$W_m = \frac{\mu}{4} \int_V \overline{H} \cdot \overline{H}^* dv, \tag{2.26b}$$

where W_e is the energy stored in the electric field; W_m is energy stored in the magnetic field.

Using Equations 2.25a to 2.25c in 2.26a and 2.26b, the stored electric and magnetic energy in a rectangular cavity resonant at TE_{101} mode is

$$\begin{aligned} W_e &= \frac{\mu}{4}\int_V E_y E_y^* dv \\ &= \frac{\epsilon abd}{16} E_0^2 \end{aligned} \tag{2.27a}$$

$$\begin{aligned} W_m &= \frac{\mu}{4}\int_V (H_x H_x^* + H_z H_z^*) dv \\ &= \frac{\mu abd}{16} E_0^2 \left(\frac{1}{Z_{TE}^2} + \frac{\pi^2}{k^2\eta^2 a^2}\right), \end{aligned} \tag{2.27b}$$

where E_0 is the maximum magnitude of E_y; $\eta = \sqrt{\mu/\epsilon}$ is the intrinsic impedance; $Z_{TE} = k\eta/\beta$ is the TE wave impedance; and $\beta = \beta_{10}$ is the propagation constant for TE_{10} mode.

The power lost in the conducting walls can be calculated in terms of surface conductivity R_s and the tangential magnetic field H_t at the surface of the walls as [5]

$$P_c = \frac{R_s}{2}\int_{walls} |\overline{H_t}|^2 ds. \tag{2.28}$$

where $R_s = \sqrt{\omega\mu_0/2\sigma}$ is the surface resistivity of the metallic walls; μ_0 is the free-space permeability, which is a constant having the value of $\mu_0 = 4\pi \times 10^{-7}$ H/m; and σ is the metal conductivity.

Using Equations 2.25b and 2.25c in Equation 2.28, the power dissipated in the walls of the cavity operating at TE_{101} mode is derived as

$$\begin{aligned} P_c &= \frac{R_s}{2}\Bigg\{2\int_{y=0}^{b}\int_{x=0}^{a} |H_x(z=0)|^2 dxdy + 2\int_{z=0}^{d}\int_{y=0}^{b} |H_z(x=0)|^2 dydz \\ &\quad +2\int_{z=0}^{d}\int_{x=0}^{a} \left[|H_x(y=0)|^2 + |H_z(y=0)|^2\right] dxdz\Bigg\} \\ &= \frac{R_s E_0^2 \lambda^2}{8\eta^2}\left(\frac{ab}{d^2} + \frac{bd}{a^2} + \frac{a}{2d} + \frac{d}{2a}\right). \end{aligned} \tag{2.29}$$

The unloaded Q factor at resonance is determined by evaluating the average electric energy stored in the cavity and the loss by the finite conductivity of the cavity walls. Using the fact that $W_e = W_m$ at the resonant frequency, unloaded Q factor of the cavity with lossy conducting walls but lossless dielectric for TE_{101} mode is found to be [5]

$$\begin{aligned} Q_{cond} &= \omega_0 \frac{W_m + W_e}{P_c} , \\ &= \frac{2\omega_0 W_e}{P_c} , \\ &= \frac{(kad)^3 b\eta}{2\pi^2 R_s} \frac{1}{(2a^3b + 2bd^3 + a^3d + ad^3)} . \end{aligned} \tag{2.30}$$

For the dielectric-filled cavity, power is dissipated in both the filling material and the conducting walls. A lossy dielectric can be characterized by its complex permittivity, which is defined as

$$\begin{aligned} \epsilon &= \epsilon' - j\epsilon'' \\ &= \epsilon_0\epsilon_r(1 - j\tan\delta). \end{aligned} \tag{2.31}$$

where $\tan\delta$ is the loss tangent of the material.

The imaginary part of ϵ accounts for the loss in the material due to the damping of the vibrating dipole moments. The loss of a dielectric material can be calculated by defining an equivalent conductivity

$$\begin{aligned} \sigma &= \omega\epsilon'' \\ &= \omega\epsilon_0\epsilon_r \tan\delta. \end{aligned} \tag{2.32}$$

Then the power dissipated in the dielectric can be found by [5]

$$\begin{aligned} P_{diel} &= \frac{1}{2}\int_V \overline{J}\cdot\overline{E}^* dV \\ &= \frac{\sigma}{2}\int_V |\overline{E}^2| dV \\ &= \frac{adb\omega\epsilon''|\overline{E_0}^2|}{8}, \end{aligned} \tag{2.33}$$

where $\overline{E}$ is given by Equation 2.25a.

From the definition of Q in Equation 2.3, the Q of the cavity with a lossy dielectric filling but with perfectly conducting walls is given by

$$Q_{diel} = \frac{2\omega_0 W_e}{P_{diel}} = \frac{1}{\tan\delta}\ , \tag{2.34}$$

which applies for any resonant mode of a rectangular cavity.

For the rectangular cavity filled with dielectric material, both metal losses and dielectric losses are present. The total loss $P_l = P_{cond} + P_{diel}$. The total unloaded Q thus can be derived as

$$Q_u = \left(\frac{1}{Q_{cond}} + \frac{1}{Q_{diel}}\right)^{-1}\ . \tag{2.35}$$

For the air-filled cavity, no dielectric loss exits. Therefore, the item Q_{diel} in Equation 2.35 can be ignored, and the total Q factor equals to Q_{cond}.

2.2.3 Coupling to Cavities

The electromagnetic fields discussed in Section 2.2.2 are inside the cavity that is completely shielded from the outside by conducting walls. It is necessary to excite the waves in the cavity by means of some source. The coupling can be via either the electric or magnetic fields of a given mode. General mechanisms used to couple, or excite, the fields by an external circuit include current loop, electrical probe, and aperture coupling.

A small loop can couple electromagnetic energy into or out of the resonator. The resonant mode in the cavity that presents a magnetic field with field lines through the loop can be excited by the loop. Thus, the plane of the loop should be perpendicular to the direction of the magnetic field of the mode desired to be excited. For efficient coupling of the desired mode, the loop should be placed at the location where the magnetic field of the given mode is a maximum. Introduction of a small probe that is parallel to the direction and at the maximum of the electric field can also excite the waves in the cavity. In addition, a small aperture on the cavity may be designed to couple electric and magnetic energy to and from the cavity. For the case of strong coupling, the slot should be in a position and orientation such that the slot intersects the current flow on the surface of the cavity.

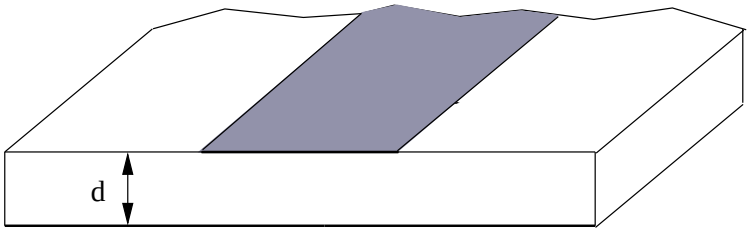

(a) Geometry of a microstrip line.

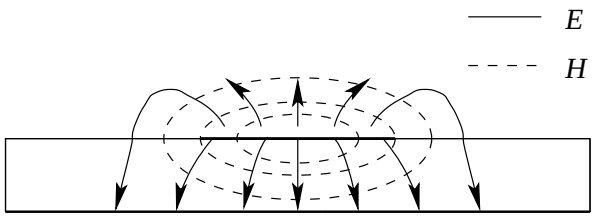

(b) Electric and magnetic field lines of a microstrip line.

Figure 2.6 Microstrip transmission line.

A method of microstrip-slot aperture coupling was first proposed in [26] as a feeding technique for a patch antenna design. The coupling mechanism is sum-

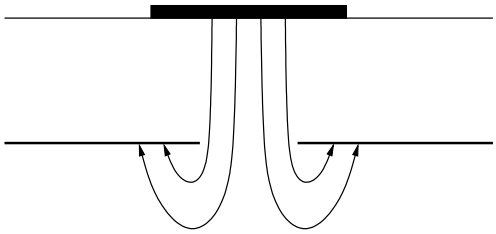

(a) Electric field lines fringing through and around an aperture in the ground plane.

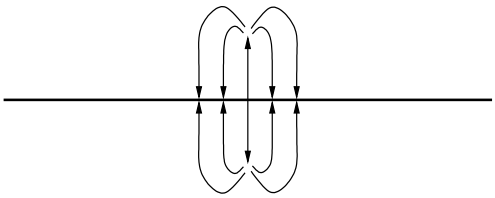

(b) Field lines generated by electric polarization currents normal to a conducting plane.

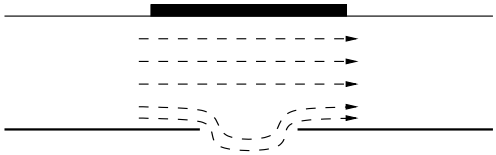

(c) Magnetic field lines fringing through and around an aperture in the ground plane.

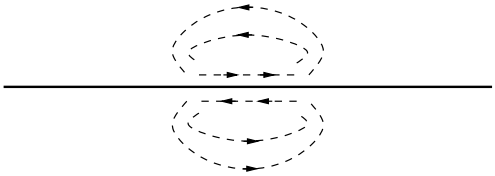

(d) Field lines generated by magnetic polarization currents parallel to a conducting plane.

Figure 2.7 Schematic illustrating of equivalent electric and magnetic polarization currents at an aperture in a conducting ground plane.

marized briefly as follows. The geometry of a microstrip line is shown in Figure 2.6(a), with a piece of conductor printed on a dielectric material, which is grounded by a thin ground plane. The electric and magnetic field lines between the long microstrip line and the ground plane are shown in Figure 2.6(b). If a small aperture is opened in the conducting ground plane, the electric and magnetic field lines will fringe through and around the slot as shown in Figure 2.7(a) and Figure 2.7(c), respectively. Figure 2.7(b) shows the field lines generated by infinitesimal electric polarization currents $\overline{P}_e$, which are both perpendicular to the closed ground plane but with opposite directions. Compared with the field lines of Figures 2.7(a) and 2.7(c), the similarity suggests that the electric field due to the microstrip mode fringing through an aperture in a ground plane can be represented by the electric polarization currents normal to the conducting plane without the presence of the aperture. Similarly, the fringing of the magnetic microstrip mode field can be represented by two infinitesimal magnetic polarization currents $\overline{P}_m$, which are located parallel to the conducting ground with opposite directions as shown in Figure 2.7(d). $\overline{P}_e$ and $\overline{P}_m$ can be related to the electric and magnetic current sources $\overline{J}$ and $\overline{M}$, which are proportional to the normal electric and parallel magnetic field density at the center of the slot, respectively. The fields on both sides of the aperture can be computed using the equivalent currents $\overline{J}$ by assuming that the aperture is closed by a conducting plane. Therefore, the aperture in the ground plane is equivalent to a current source placed below the ground plane that excites the fields in the cavity.

2.3 Summary

In this chapter the basic characteristics of the resonators, such as the definition of Q factor and coupling coefficient, are presented by the lumped RLC resonator models. Then the properties of rectangular waveguide cavities, a form of implementation of resonator circuits at microwave frequencies, are discussed. Also, some typical coupling techniques used to excite the fields inside the cav-

ity are illustrated. The resonator basics presented in this chapter establish the theoretical background for the design procedures in the following chapters.

Chapter 3

EXPERIMENTAL TECHNIQUES

3.1 Simulation Techniques

The resonator model cannot be easily simulated using empirical methods, because of the lack of component models for structures with coupling slots. Numerical techniques, such as the finite element method (FEM), need to be employed to analyze the resonator.

FEM is one of the oldest numerical techniques applied to engineering problems. The term finite element was first discussed by Clough in 1960 [27]. The first textbook on FEM appeared in 1967 [28]. In the late 1960s and early 1970s, FEM was applied by engineers to a wide variety of problems including stress analysis, fluid flow, heat transfer, and other areas. Most of the commercial FEM softwares originated in 1970s and 1980s.

FEM is a method for numerical solution of field problems by solving partial differential equations and also integral equations. The advantage of FEM includes its capacity of handling bodies composed of complex geometries (2-D and 3-D) and materials (homogeneous and nonhomogeneous). The principle process steps involved in FEM are briefly illustrated using Ansoft HFSS [29] as a demonstration tool. More detailed and advanced references on the FEM applied to electromagnetic problems can be found in [30] and [31]. Ansoft HFSS is a software package specialized in solving electromagnetic field solutions using FEM, and is used to model all of the cavity resonator circuits. In FEM, the full complex problem model is divided into simple geometric sub-regions, which are called elements.

The elements in 3D forms could take on different shapes such as bricks, prisms, and tetrahedra. In Ansoft HFSS, the entire structure is divided into a large number of tetrahedra, which are essentially four-sided pyramids shown in Figure 3.1. The process of model dividing is called meshing. Correspondingly, the collections of the tetrahedra are referred to as the finite element mesh.

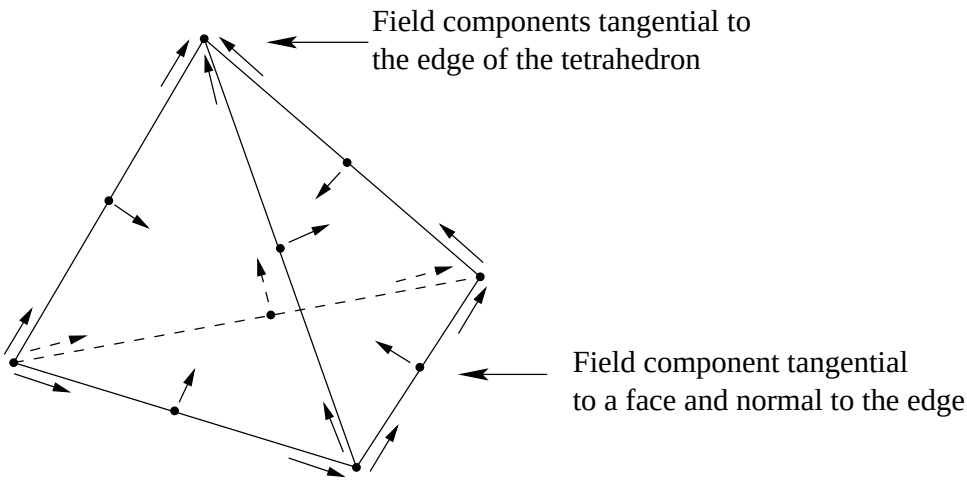

Figure 3.1 Geometry of a tetrahedral element in Ansoft HFSS.

The vector quantities, such as the electric field and magnetic field, are solved at the vertices and nodes that are the midpoints between each pair of vertices. At each vertex, the program stores the field components that are tangential to the edges of the tetrahedron. At each node, fields solutions that are tangential to a face and normal to the edge are stored as well. The field solutions inside the tetrahedron are interpolated from these stored field components. Thus, the solutions of Maxwell's Equations derived by numerical method are stored as matrices.

The accuracy of the solutions depends on how dense the model is meshed. To generate accurate field quantities, the volume of each tetrahedron must be small enough so that fields can successfully interpolated from the values at vertices and nodes. Generally, solutions obtained by finely meshed models containing thousands of elements (tetrahedra) are more precise than those based on coarse meshes using relatively small number of elements. But for meshes with a large

number of elements, a significant number of matrices are generated to store the field quantities, which will considerably affect the required computer memory and simulation time. Therefore, a compromise must be made between the size of the mesh and the level of accuracy.

To produce the optimal mesh, Ansoft HFSS first generates a solution based on a coarse initial mesh. Then the mesh is automatically refined in a way that the refinement is focused on the areas of high error density, which saves the computer resource and simulation time. The simulation stops if the new solutions generated from the refined mesh meet the criteria of convergence governed by selected parameters. Otherwise, the model will be meshed further until convergence to a solution is obtained.

3.2 Q Factor Measurement

3.2.1 Impedance Measurement

As described in Section 2.1, the fundamental characteristics that define a resonator include resonant frequency f_0, coupling coefficient k, and unloaded Q factor.

The Q value of a resonant cavity can be determined in many ways. Among them, impedance measurement is based on the observation of the input impedance of the resonator varying with frequency, and thus is suitable for the measurement of a one-port resonator configuration. This method was first proposed by Gintzon in [32], and is described briefly as follows.

Consider a coupling network that contains a cavity, a coupling system, and a piece of transmission line connecting to a power source, as shown in Figure 3.2 [32]. The cavity resonance in a particular mode is represented by the parameters L, C and R_s. The coupling mechanism is represented by its self-inductance L_1 and mutual inductance M between it and the cavity inductance L, while the resistive losses in the coupling network are neglected. The circuit can be simplified by transforming the effect of the coupling network into a coupled impedance in series

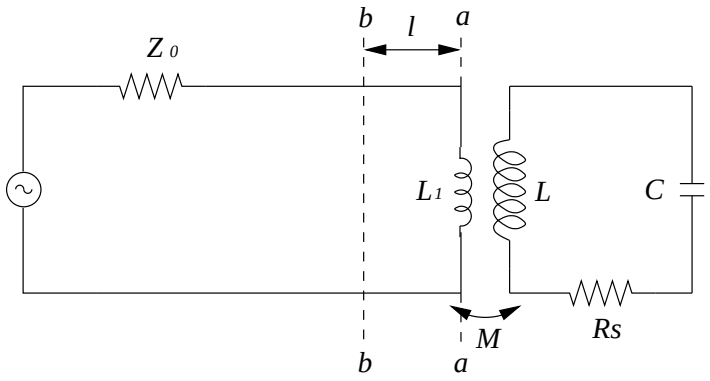

Figure 3.2 Equivalent circuit of a cavity coupled to a signal source.

with the cavity parameters, as shown in Figure 3.3. The coupled impedance is given by

$$\begin{aligned} Z &= \frac{(\omega M)^2}{Z_0 + j\omega L_1} \\ &= \frac{(\omega M)^2}{Z_0\left[1+\left(\frac{\omega L_1}{Z_0}\right)^2\right]}\left(1 - j\frac{\omega L_1}{Z_0}\right). \end{aligned} \tag{3.1}$$

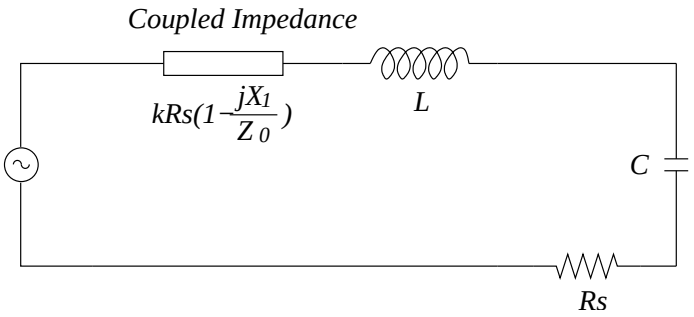

Figure 3.3 Equivalent circuit with the coupling network transformed into a coupled impedance.

To simplify the expression, a parameter k is defined as

$$\begin{aligned} k &= \frac{(\omega M)^2}{Z_0 R_s} \frac{1}{1+\left(\frac{X_1}{Z_0}\right)^2} \\ &= \frac{k_1}{1+\left(\frac{X_1}{Z_0}\right)^2} , \end{aligned} \tag{3.2}$$

where

$$k_1 = \frac{(\omega M)^2}{Z_0 R_s}. \tag{3.3}$$

Using Equation 3.2 and $X_1 = \omega L_1$, Equation 3.1 becomes

$$Z = kR_s \left(1 - \frac{jX_1}{Z_0}\right) . \tag{3.4}$$

The loaded Q factor for a coupled series resonant circuit is defined by the ratio of total reactance to the total series loss. For the circuit shown in Figure 3.3, the loaded Q is

$$\begin{aligned} Q_l &= \frac{\omega L - kR_s \frac{X_1}{Z_0}}{R_s(1+k)} \\ &= \frac{\omega L}{R_s} \frac{\left(1 - \frac{kR_s}{Z_0}\frac{X_1}{\omega L}\right)}{1+k} . \end{aligned} \tag{3.5}$$

Neglecting the second term in the numerator of Equation 3.5, representing the ratio of coupled reactance to the cavity reactance which is usually small compared to unity, Equation 3.5 becomes

$$Q_l = \frac{Q_u}{1+k}, \tag{3.6}$$

where

$$Q_u = \frac{\omega L}{R_s} , \tag{3.7}$$

is the Q factor of the unloaded cavity circuit. Equation 3.6 is also the same

relationship for coupling coefficient k defined in Equation 2.12.

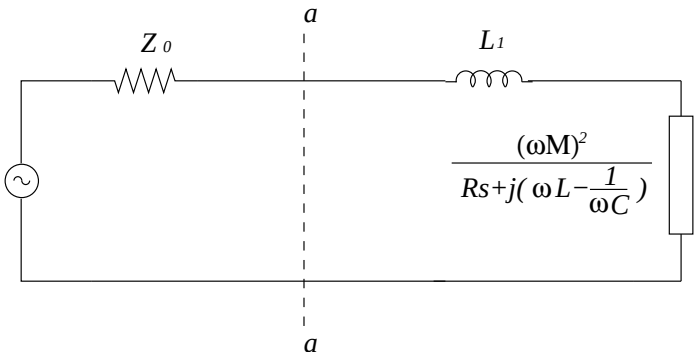

Figure 3.4 Equivalent circuit with the cavity transformed into a coupled impedance.

Figure 3.2 can be simplified further by transforming the cavity into a coupled impedance in series with the inductance L_1, as shown in Figure 3.4. The total input impedance at the terminal of the coupling system, which is located at a position $a - a$ near the cavity in Figure 3.4, can be written as

$$Z_{aa} = jX_1 + \frac{(\omega M)^2}{R_s + j(\omega L - \frac{1}{\omega C})} \ . \tag{3.8}$$

With the similar approach used to derive Equation 2.8, the normalized input impedance at reference plane $a - a$ can be approximated as

$$\frac{Z_{aa}}{Z_0} = j\frac{X_1}{Z_0} + \frac{k_1}{1 + 2jQ_u\delta} \ , \tag{3.9}$$

where

$$\delta = \frac{\omega - \omega_0}{\omega_0} = \frac{\Delta\omega}{\omega_0}, \tag{3.10}$$

and is the frequency-tuning parameter; k_1 is the ratio of the coupled resistance to the cavity resistance R_s; Z_0 is the characteristic impedance of the transmission line, as well as the internal impedance of the signal source.

The second term of Equation 3.9 presents the impedance of an unloaded parallel resonant circuit, which was described in Equation 2.8, with impedance $k_1 Z_0$ at

resonant frequency of ω_0, and describes a circle with diameter k_1 on the normalized complex impedance plane. The first term in the equation, which is introduced by the self-reactance of the coupling system, causes the circle to displace along the imaginary axis, as shown in Figure 3.5.

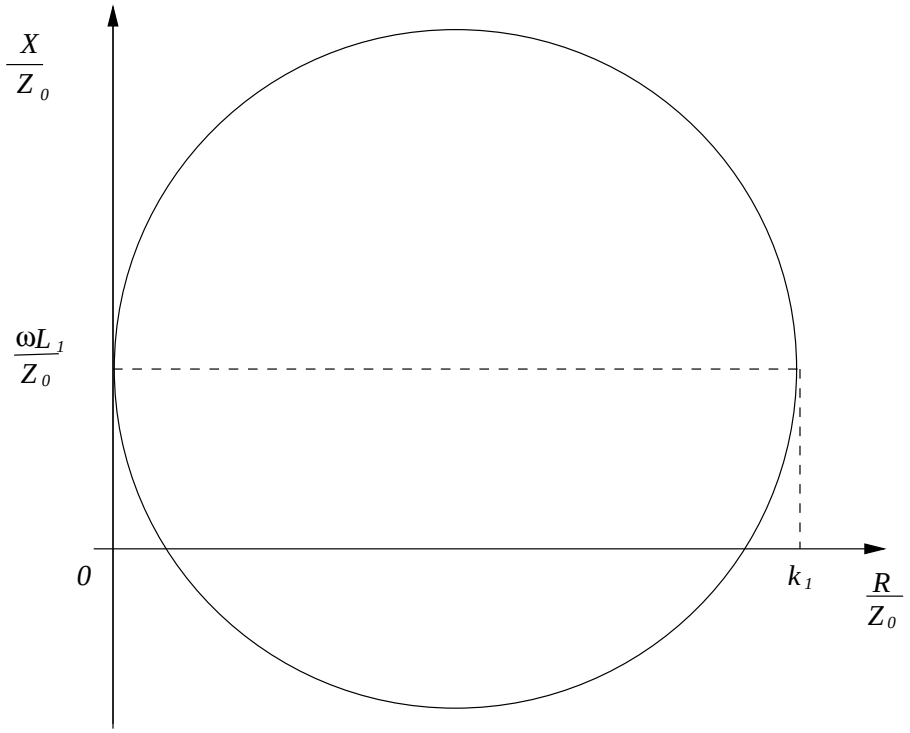

Figure 3.5 Normalized input impedance of the resonant cavity referred to an arbitrary position.

The effect of self-reactance of the coupling system can be removed by finding special reference planes along the transmission line, which are called detuned-short or detuned-open positions. At the detuned-short position, the impedance looking into the cavity represents a simple parallel circuit. Similarly, at the detuned-open position, which is $\lambda/4$ away from the detuned-short position, the impedance appears as a series resonant circuit.

The detuned-short position can be found by tuning the frequency far off resonance. At this frequency, the second term in Equation 3.9 disappears, and the impedance becomes the self-reactance of the coupling system. At the reference

plane $b-b$, which is away from the plane $a-a$ by a distance l, the impedance looking into the cavity is

$$\frac{Z_{bb}}{Z_0} = \frac{Z_{aa} + jZ_0 tan\beta l}{Z_0 + jZ_{aa} tan\beta l}. \tag{3.11}$$

The length l of the transmission line can be chosen so that the first term in the Equation 3.9 disappears. When the cavity is detuned, making $Z_{bb} = 0$ yields

$$\beta l = -\tan^{-1}\left(\frac{X_1}{Z_0}\right). \tag{3.12}$$

Substituting Equations 3.9 and 3.12 into Equation 3.11, the impedance at the detuned short position is derived as

$$\frac{Z_{bb}}{Z_0} = \frac{k}{1 + j2Q_u(\delta - \delta_0)}\ , \tag{3.13}$$

where

$$\delta_0 = \frac{k}{2Q_u}\left(\frac{X_1}{Z_0}\right), \tag{3.14}$$

and k is expressed in Equation 3.2.

Similar to the second term in Equation 3.9, Equation 3.13 represents a parallel resonant circuit with an impedance kZ_0 at resonance, and also corresponds to a circle on the impedance plane, as shown in Figure 3.6. Compared to the impedance circle described by Equation 3.9, the diameter of the transformed circle corresponding to the impedance at plane $b-b$ given by Equation 3.13 is different. Also, the resonant frequency of the circuit described by Equation 3.13 is altered from the resonant frequency ω_0 of the cavity by the amount given by Equation 3.14.

The resonator characteristics then can be determined based on the observation of the variation of the input impedance of the resonator with frequency. With the detuned short position as the reference plane, the measured impedance locus

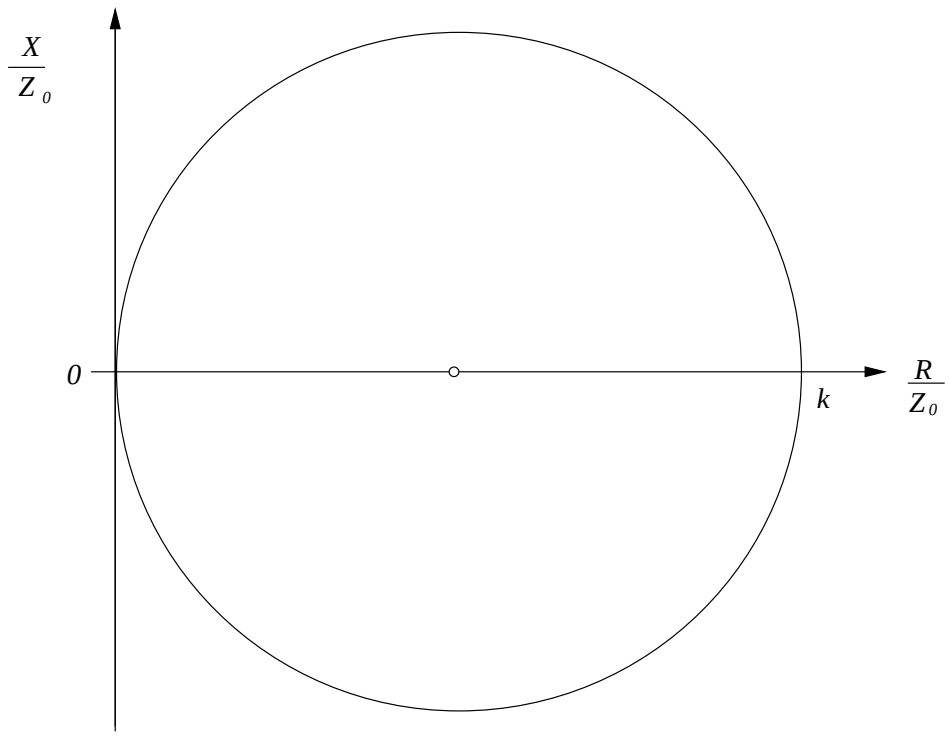

Figure 3.6 Normalized input impedance of the resonant cavity referred to an arbitrary the detuned short position.

as a function of frequency describes a circle. The values of Q_u, Q_l and Q_{ext} can be obtained by interpreting the impedance data. Theoretically, the resonator characteristics can be determined by measuring impedance at only three frequency points, since a circle can be completely defined by three points. In order to improve the accuracy, additional data can be taken to account for the random, systematic, or accidental errors.

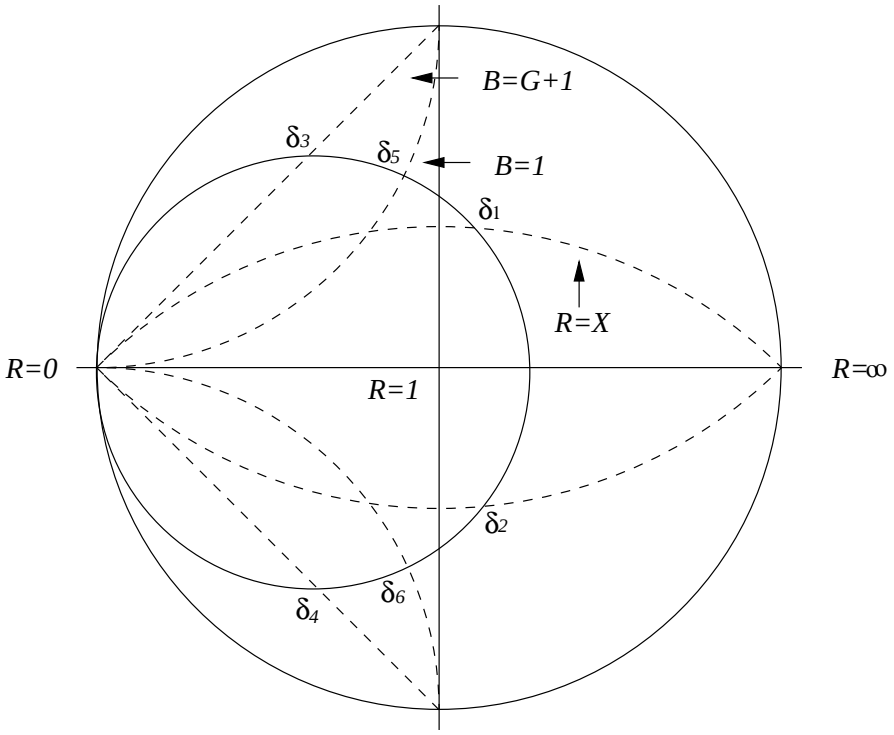

Figure 3.7 Identification of the points from the Smith chart.

According to Equation 3.13, at certain frequencies the imaginary part of the denominator equals ± 1, and the input impedance becomes

$$\frac{Z_{bb}}{Z_0} = \frac{k}{1 \pm j} \ , \tag{3.15}$$

which has equal resistive and reactive parts ($R = X$). The locus of these points regardless of k is a circle on the Smith chart as shown in Figure 3.7, with center at the $\pm 90^o$ point, and passing through 0 and 180^o on the unit circle. The frequency

points satisfying Equation 3.15 locate at the intersection of this circle with the impedance circle. And the corresponding δ, called δ_1 and δ_2, satisfies

$$2Q_u(\delta_1 - \delta_0) = 1, \tag{3.16a}$$

$$2Q_u(\delta_2 - \delta_0) = -1. \tag{3.16b}$$

Hence, by rearranging Equations 3.16a and 3.16b Q_u is found in terms of frequency as as

$$\begin{aligned} Q_u &= \frac{1}{\delta_1 - \delta_2} \\ &= \frac{f_0}{f_1 - f_2}. \end{aligned} \tag{3.17}$$

Thus, Q_u can be graphically determined by finding the two frequencies on the Smith chart, at which the impedance locus passes through the point $R = X$, as indicated in Figure 3.7.

The loaded and external Q values can be determined in a similar way. Substituting Q_u by Q_l as in Equation 3.5, Equation 3.13 becomes

$$\frac{Z_{bb}}{Z_0} = \frac{k}{1 + j2Q_l(1+k)(\delta - \delta_0)} \ . \tag{3.18}$$

Similarly, Equation 3.13 can be expressed in terms of Q_{ext} as

$$\frac{Z_{bb}}{Z_0} = \frac{k}{1 + j2Q_{ext}k(\delta - \delta_0)} \ . \tag{3.19}$$

Frequency tuning parameters δ_3 and δ_4, which satisfy

$$2Q_l(\delta - \delta_0) = \pm 1 \ , \tag{3.20}$$

can be defined. At these frequency points, the impedance becomes

$$\frac{Z_{bb}}{Z_0} = \frac{k}{1 \pm j(1+k)}. \ , \tag{3.21}$$

Similarly, δ_5 and δ_6 are defined, which satisfy

$$2Q_{ext}(\delta - \delta_0) = \pm 1. \tag{3.22}$$

At these frequency points, the impedance becomes

$$\frac{Z_{bb}}{Z_0} = \frac{k}{1 \pm jk} \ . \tag{3.23}$$

Then Q_l and Q_{ext} can be derived in terms of specific frequency points as

$$Q_l = \frac{1}{\delta_3 - \delta_4} \ , \tag{3.24}$$

$$Q_{ext} = \frac{1}{\delta_5 - \delta_6} \ , \tag{3.25}$$

where δ_3 and δ_4 can be found by the intersection of the $B = G + 1$ circle and the impedance circle; δ_5 and δ_6 are located on the intersection of the $B = 1$ circle and the impedance circle, as shown in Figure 3.7. Therefore, by locating these frequency points as summarized in Figure 3.7, Q_u, Q_l, and Q_{ext} can be derived according to Equations 3.17, 3.24, and 3.25, respectively.

3.2.2 Reflection Type Measurement

As described above, the method developed in [32] requires the definition of special reference planes such as detuned open and detuned short positions. The impedance data are interpreted with respect to one of these two reference points, which implies the effect of the reactance of the external circuits must be neglected. This measurement is complicated by the requirement to rearrange the measured data relative to the reference point. Besides, this measurement method relies

solely on the discrete data, and thus tends to give poor results when the practical effects introduced by a real measurement system, such as noise, are presented.

Based on the procedure documented in [32], a reflection type measurement, which is considered one of the most accurate and practical Q-factor measurement [33], [34], is described in [35] with a few modifications. The reference plane is assumed to be the end of a section of transmission line leading to the resonator, so that the data measured from a network analyzer can be used directly. The coupling mechanism is taken into account in the method described in [35]. The measurement involves fitting the complex reflection coefficient data into the impedance circle on the Smith chart. The data are processed using the linear fractional curve-fitting algorithm, instead of the graphic procedure described by Ginzton. Furthermore, this data-fitting procedure allows the calculation of the random errors caused by imperfect data away from ideal circle, and thus makes the measurement performed in a more systematic way. A program called $QZERO$ [36] was developed to assist determining the Q factor of a resonator using the reflection type measurement described above. The method is described briefly in the following sections. Details about the principle of the reflection type of measurement and the program $QZERO$ can be found in [35], [37], [38], and [36].

Lossless Coupling

The equivalent circuit for the input impedance Z_i of a reactance-coupled (either inductance or capacitance) cavity resonator is represented by Figure 3.8. In practice, an infinite number of resonant modes (resonant frequencies) exist in the cavity. In the narrow range of frequencies around a certain resonant frequency ω_0, the term (R_e+jX_e) in Figure 3.8 can represent the equivalent external impedance, including the effect of the coupling structures and off-resonance modes. The transmission line with the characteristic impedance R_c represents the cable connecting the resonator to the measurement equipment. When the measurement is performed in the narrow range of frequencies around the unloaded resonant

frequency ω_0, the mathematical expression for the input impedance measured by the network analyzer is (R_e is ignored for the sake of simplicity)

$$Z_i = jX_e + \frac{R_0}{1 + 2jQ_0\frac{\Delta\omega}{\omega_0}} \ , \tag{3.26}$$

where Q_0 is the unloaded Q factor of the resonator.

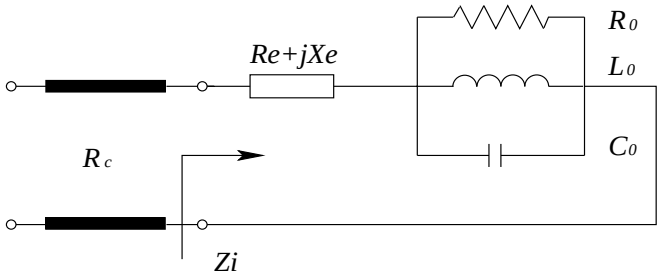

Figure 3.8 Equivalent circuit for a reactive-coupled cavity in the vicinity of resonant frequency ω_0.

The second term on the right hand side corresponds to an exact circle on the complex rectangular impedance plane. The frequency dependence of reactance X_e distorts the circular shape of the Q circle so that a "balloon" shape loop is formed. However, for high Q factor systems, the bandwidth of measurement is very small, and the reactance can be assumed to be constant in the narrow range of frequencies around the resonance without any loss of measurement accuracy. The reflection type of Q measurement is based on the observation of the circle created by the reflection coefficient plotted on the Smith chart as a function of the frequency.

Assuming that the loss introduced by the coupling mechanism can be neglected, the analysis can be simplified by setting R_e equal to zero in the equivalent circuit for the coupled cavity shown in Figure 3.8.

The loaded resonant cavity can be represented by attaching an external resistance R_c to port one, as shown in Figure 3.9. R_c is chosen to be equal to the characteristic impedance of the transmission line leading to the cavity. Observing

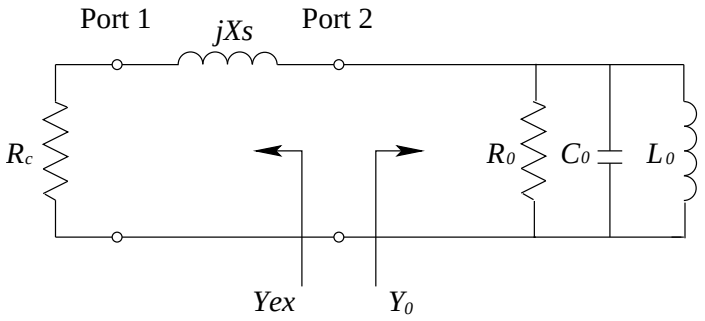

Figure 3.9 Equivalent circuit for loaded resonant cavity.

at port 2, the external admittance Y_{ex} and unloaded admittance Y_0 can be written as

$$Y_{ex} = G_{ex} + jB_{ex} = \frac{1}{R_c + jX_s} \ , \tag{3.27}$$

$$Y_0 = G_0 \left(1 + jQ_0 2\frac{\omega - \omega_0}{\omega_0}\right), \tag{3.28}$$

where the conductance G_{ex} and susceptance B_{ex} of the external circuit is

$$G_{ex} = \frac{R_c}{R_c^2 + X_s^2} \ , \tag{3.29}$$

$$B_{ex} = -\frac{X_s}{R_c^2 + X_s^2} \ . \tag{3.30}$$

Since X_s is assumed to be constant within the narrow range of frequencies, G_{ex} and B_{ex} also can also be treated as constant.

The observation at port 2, which is hidden inside the cavity, shows the effect of the external circuit on the cavity. The existence of the external circuit, including the coupling mechanism and a resistive loading, changes the resonant frequency and lowers the Q value compared with the unloaded cavity.

From Figure 3.9, the total admittance of the loaded cavity is

$$\begin{aligned} Y_L &= Y_0 + Y_{ex} \\ &= G_{ex} + G_0 + j\left(G_0 Q_0 2\frac{\omega - \omega_0}{\omega_0} + B_{ex}\right) \ , \end{aligned} \tag{3.31}$$

where $G_0 = 1/R_0$. Hence the loaded resonant frequency is found, when the imaginary part of the above equation equals zero, as

$$\omega_L = \omega_0 \left(1 - \frac{B_{ex}}{2Q_0 G_0}\right) \ . \tag{3.32}$$

Substituting B_{ex} in Equation 3.31, the loaded admittance can be expressed alternatively as

$$Y_L = (G_{ex} + G_0)\left(1 + jQ_L 2\frac{\omega - \omega_0}{\omega_0}\right) \ , \tag{3.33}$$

where Q_L is the loaded Q factor, and is defined as

$$Q_L = Q_0 \frac{G_0}{G_0 + G_{ex}} \ . \tag{3.34}$$

The coupling coefficient, which is defined as the ratio of the power dissipated in the external circuit to the power dissipated in the unloaded resonator, is then expressed as

$$k = \frac{G_{ex}}{G_0} \ , \tag{3.35}$$

and Equation 3.34 becomes

$$Q_L = \frac{Q_0}{1 + k} \ , \tag{3.36}$$

which is in agreement with the relationship between k and Q defined previously in Equation 2.12.

By replacing G_{ex} with Equation 3.29, k can be expressed in terms of the elements in Figure 3.9 as

$$k = \frac{\frac{R_0}{R_c}}{1 + \left(\frac{X_s}{R_c}\right)^2} \ . \tag{3.37}$$

Substituting Equations 3.37 and 3.30 into 3.32, an alternative expression for ω_L is obtained as

$$\omega_L = \omega_0 \left(1 + \frac{kX_s}{2Q_0 R_c}\right) \ . \tag{3.38}$$

Using this expression, ω_0 can be calculated from the measured ω_L. For a high value of Q_0 in the thousands, the difference between ω_0 and ω_L can be very little.

When plotted on the Smith chart, the measured impedances are transformed into complex reflection coefficients, which fall into the unit circle. The expression for the input reflection coefficient can be obtained from the equivalent circuit as

$$\begin{aligned} \Gamma_i &= \frac{Z_i - R_c}{Z_i + R_c} , \\ &= \frac{jX_s + \frac{1}{Y_0} - R_c}{jX_s + \frac{1}{Y_0} + R_c} , \end{aligned} \tag{3.39}$$

where Z_i is the input impedance observed at port 1 in Figure 3.9.

If the coupling coefficient k diminishes to zero, Y_0 tends toward infinity. This point is situated on the border of the Smith chart, and is referred to as detuned reflection coefficient, which is expressed as

$$\begin{aligned} \Gamma_d &= \frac{jX_s - R_c}{jX_s + R_c} , \\ &= -\frac{Y_{ex}}{Y_{ex}^*} . \end{aligned} \tag{3.40}$$

Then Γ_i can be expressed in term of Γ_d as

$$\Gamma_i = \Gamma_d + \left(\frac{Y_{ex}}{Y_{ex}^*}\right) \frac{2G_{ex}}{Y_0 + Y_{ex}} . \tag{3.41}$$

From Equations 3.31 and 3.35, Γ_i becomes

$$\Gamma_i = \Gamma_d \left(1 - \frac{2k}{1+k} \cdot \frac{1}{1 + jQ_L 2\frac{\omega - \omega_L}{\omega_0}} \right) . \tag{3.42}$$

At a frequency far from the resonance, the second term of the Equation 3.42 in the parenthesis is close to zero, so that the input reflection coefficient is approximately the detuned reflection coefficient ($\Gamma_i \simeq \Gamma_d$), which resides on the border

of the Smith chart as shown in the input impedance circle (Q circle) plotted in Figure 3.10. In the vicinity of the loaded resonant frequency ω_L, the second term of the Equation 3.42 in the parenthesis describes a circle, with the diameter of

$$d = \frac{2k}{1+k} \ , \tag{3.43}$$

which is within the limit of $0 < d < 2$. The stronger the coupling, the bigger is the diameter of the Q circle. At $\omega = \omega_L$, the amplitude of the reflection coefficient is minimum, with the value

$$|\Gamma_i|_{min} = |\Gamma_L| = |1 - d|, \tag{3.44}$$

as shown in Figure 3.10.

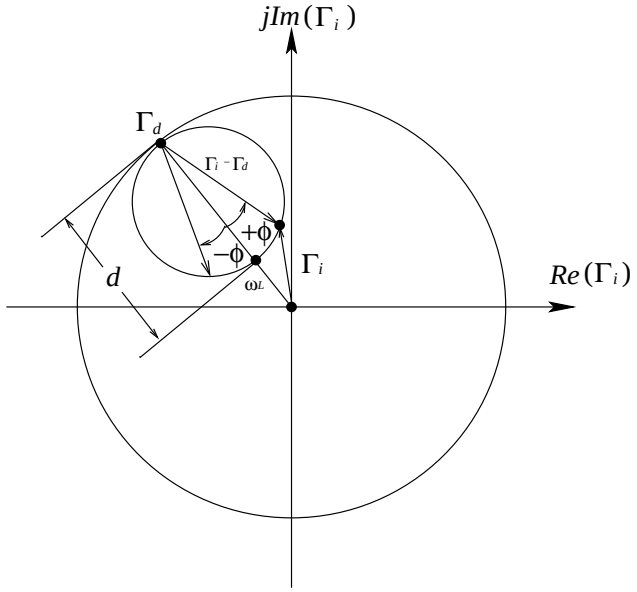

Figure 3.10 Ideal Q circle of a microwave resonator.

For critical coupling ($k = 1$), the diameter of the Q circle is unity, and Γ_i is located on the center of the Smith chart. When the resonator is undercoupled, the diameter d is less than unity; when the resonator is overcoupled, the diameter d is greater than unity.

The vector of $\Gamma_i - \Gamma_d$ is rotated with respect to $-\Gamma_d$, and the relative angle is specified by Equation 3.42 as

$$\phi = -\tan^{-1}\left(Q_L 2\frac{\omega - \omega_L}{\omega_0}\right), \tag{3.45}$$

As frequency changes, the vector $\Gamma_i - \Gamma_d$ moves on the Q circle, and its phase with respect to $-\Gamma_d$ is shown in Figure 3.10. At $\omega = \omega_L$, Γ_i reaches its minimum, no matter if the resonator is overcoupled or undercoupled.

At the specific frequency of f_1, which is below the resonant frequency f_L, the corresponding angle of the vector $\Gamma_i - \Gamma_d$ with respect to $-\Gamma_d$ is

$$\tan(\phi_1) = -Q_L 2\frac{f_1 - f_L}{f_0}, \tag{3.46}$$

where $\tan(\phi_1)$ is positive.

Similarly, at frequency of f_2, which is above the resonance, the corresponding angle is

$$\tan(\phi_2) = -Q_L 2\frac{f_2 - f_L}{f_0}, \tag{3.47}$$

where $\tan(\phi_2)$ is negative.

The loaded Q can be obtained by subtracting Equation 3.47 from 3.46 as

$$Q_L = \frac{1}{2}\frac{f_L}{f_2 - f_1}(\tan\phi_1 - \tan\phi_2). \tag{3.48}$$

For the case that $\phi_1 = 45^o$ and $\phi_2 = -45^o$, Equation 3.48 is reduced to the simple form

$$Q_L = \frac{f_L}{f_2 - f_1}. \tag{3.49}$$

Therefore, by observing the behavior of the Q circle, which is formed by the input reflection coefficient as a function of frequency, the parameters of a resonator can be determined graphically. The coupling coefficient can be found by the diameter of the Q circle using Equation 3.43; quality factors Q_L and Q_0 can be

determined from Equation 3.48 and 3.36, respectively.

In order to perform accurate measurements using the multiple S-parameter data points generated from a vector network analyzer, a convenient numerical method to replace the traditional graphical data fitting procedure is required. A numerical method of data fitting for a linear fractional transformation on the complex plane is employed by the reflection type measurement to recover the Q factors and coupling coefficient. The procedure is briefly described below. Details can be found in [37] and [36].

For the lossless case, the magnitude of the detuned reflection coefficient $|\Gamma_d| = 1$, so that $|\Gamma_d|$ can be represented by its phase angle only as

$$\Gamma_d = e^{-j2\delta}. \tag{3.50}$$

Substituting the coupling coefficient k by the diameter of the Q circle as expressed in Equation 3.43, Equation 3.42 can be rewritten as

$$\Gamma_i = \frac{jQ_L\Gamma_d 2\dfrac{\omega-\omega_L}{\omega_0} + \Gamma_d + de^{-j2\delta}}{jQ_L 2\dfrac{\omega-\omega_L}{\omega_0} + 1}\ . \tag{3.51}$$

This expression can be recognized as a linear fractional transformation

$$\Gamma_i = \frac{a_1 t + a_2}{a_3 t + 1}, \tag{3.52}$$

where t is a normalized frequency variable, and is defined as

$$t = 2\frac{\omega-\omega_L}{\omega_0} = 2\frac{f-f_L}{f_0}. \tag{3.53}$$

When normalized in such a manner, the fractional linear transformation is defined in terms of the three complex coefficients a_1 to a_3, which are the transfor-

mation constants written as

$$a_1 = jQ_L\Gamma_d, \tag{3.54a}$$

$$a_2 = \Gamma_d + de^{-j2\delta}, \tag{3.54b}$$

$$a_3 = jQ_L. \tag{3.54c}$$

The loaded Q factor and the diameter of the Q circle can be solved from the three transformation coefficients by

$$Q_L = \mathrm{Im}(a_3), \tag{3.55}$$

$$d = \left| a_2 - \frac{a_1}{a_3} \right|. \tag{3.56}$$

The coupling coefficient and unloaded Q can be found from these two parameters by using Equations 3.43 and 3.36, respectively.

Three points of the reflection coefficient measured at different frequencies are enough to solve for the unknown coefficients. In the case that the data points chosen could be unreliable due to the effect of noise, it is safe to perform more than three measurements and obtain an overdetermined system of equations.

In order to find the transformation coefficients, N measured points Γ_i are applied to Equation 3.52 at N frequency points, which forms an overdetermined system of N equations with three unknown variables. The system is solved by the least-square method for the three unknowns. Details of the curve fitting procedure is described in [38]. The procedure of finding the transformation coefficients consists of writing the Equation 3.52 as linear combination of a_1, a_2, and a_3 as

$$a_1 t_n + a_2 - a_3 t_n \Gamma_{i,n} = \Gamma_{i,n} \quad n = 1, 2, 3, ..., N. \tag{3.57}$$

The least-square result of the system provides the solutions for a_1, a_2, a_3, and their variances as well. In this procedure, the individual measurements are

weighted in a way that the weights are inversely proportional to the variances of individual measurements, which prevents less reliable data from have too much undesired influence on the results, and improves the stability of solutions. The circuit elements Q_L, Q_0, and k can be specified by the three complex transformation coefficients a_1, a_2, and a_3. The uncertainty (=standard deviation=square root of variance) of the measured quantities can be determined from the variances of the transformation coefficients.

The curve fitting procedure is performed iteratively. In the first iteration, neither the resonant frequencies, f_0 and f_L, nor the variances of the three transformation coefficients are precisely known. Therefore, unloaded and loaded resonant frequencies f_0 and f_L in Equation 3.53 are estimated as the frequency of the measured point closest to the origin of the Smith Chart, and the weights are estimated by assuming that all three variances to be equal to each other. In the later iteration steps, the resonant frequencies and weights are improved and determined more accurately. When the iteration is finished, the three unknown coefficients as well as their variances are obtained. In this measurement, the only source of error is the random variations of data, the system errors of the equipment that generates the data are not considered. For random errors, the standard uncertainty means a 63% probability that the complex number will be situated within the specified error circle.

Correction for Coupling Losses

For a coupling system with appreciable losses, the equivalent circuit can be modified by adding a resistance R_s series with reactance X_s, as shown in Figure 3.11. A section of transmission line with characteristic impedance R_c is also included in the equivalent circuit. The lossy coupling system is represented by the circuit between ports $1'$ and 2. The unloaded resonant cavity is modeled by a parallel RLC lumped circuit.

When observed at port 2, the entire equivalent circuit in Figure 3.11 can be

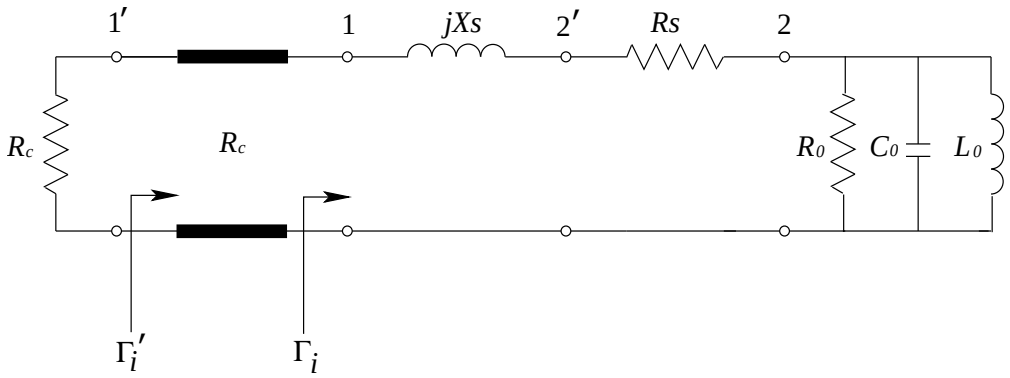

Figure 3.11 Complete equivalent circuit including the effect of coupling losses for a reactive-coupled cavity in the vicinity of resonant frequency.

simplified to the one as shown in Figure 3.12. The external admittance added to the unloaded cavity can be written as

$$Y_{ex} = G_{ex} + jB_{ex} = \frac{1}{R_c + R_s + jX_s} \ , \tag{3.58}$$

where G_{ex} is the sum of two parts

$$G_{ex} = G_{e1} + G_{e2}. \tag{3.59}$$

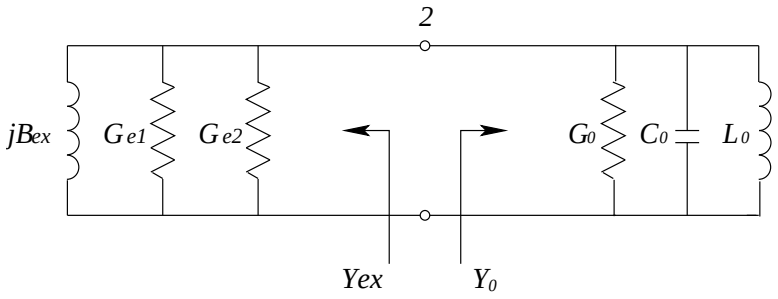

Figure 3.12 Equivalent circuit at port 2.

G_{e1} corresponds to the effect of the characteristic impedance R_c, and G_{e2}

exhibits the effect of coupling loss R_s as

$$G_{e1} = \frac{R_c}{(R_c + Rs)^2 + X_s^2} \ , \tag{3.60a}$$

$$G_{e2} = \frac{R_s}{(R_c + Rs)^2 + X_s^2} \ . \tag{3.60b}$$

The susceptance observed to the left of port 2 is

$$B_{ex} = -\frac{X_s}{(R_c + Rs)^2 + X_s^2} \ . \tag{3.61}$$

Using a similar procedure as described in Section 3.2.2, the admittance of the loaded resonator is found to be

$$\begin{aligned} Y_L &= Y_0 + Y_{ex} \\ &= (G_{ex} + G_0)\left(1 + jQ_L 2\frac{\omega - \omega_0}{\omega_0}\right) \ . \end{aligned} \tag{3.62}$$

The overall coupling coefficient is defined as

$$\begin{aligned} k &= \frac{G_{ex}}{G_0} = \frac{G_{e1} + G_{e2}}{G_0} \\ &= k_1 + k_2, \end{aligned} \tag{3.63}$$

where k_2 represents the ratio of the power dissipation in the coupling circuit to that in the unloaded resonator.

The input reflection coefficient observed at port 1 is given by

$$\Gamma_i = \frac{R_s + jX_s + \frac{1}{Y_0} - R_c}{R_s + jX_s + \frac{1}{Y_0} + R_c} \ . \tag{3.64}$$

Equation 3.64 can be rearranged to a simpler form by multiplying the numer-

ator and denominator by Y_{ex} and Y_0

$$\Gamma_i = \frac{Y_{ex}[Y_0(R_s + jX_s - R_c) + 1]}{Y_0 + Y_{ex}} \ . \tag{3.65}$$

By setting Y_0 to zero, the detuned reflection coefficient can be obtained as

$$\Gamma_d = \frac{R_s jX_s - R_c}{R_s jX_s + R_c} \ . \tag{3.66}$$

It is noted that the magnitude $|\Gamma_d|$ is less than unity due to the introduction of coupling resistance R_s.

Then Γ_i can be expressed in terms of Γ_d as

$$\Gamma_i = \Gamma_d + \frac{Y_{ex}(1 - \Gamma_d)}{Y_L} \ . \tag{3.67}$$

Using Equation 3.62, Γ_i as a function of frequency is obtained as

$$\Gamma_i = \Gamma_d + \frac{de^{j\gamma}}{1 + jQ_L 2\dfrac{\omega - \omega_L}{\omega_0}} \tag{3.68}$$

where d is the diameter of the Q circle, which is

$$d = \frac{k_1}{1 + k_1 + k_2} \ , \tag{3.69}$$

and γ is the rotation angle, which is

$$\gamma = -2\tan^{-1}\left(\frac{X_s}{R_c + R_s}\right) \ . \tag{3.70}$$

Compared with the Q circle for the lossless case described by Equation 3.42, the presence of k_2 leads to the reduction of the circle diameter. Since in general the magnitude of k_2 is small, which is on the order of 0.01, the diameter is reduced by only about several percent. A graphical interpretation of this fact is that the

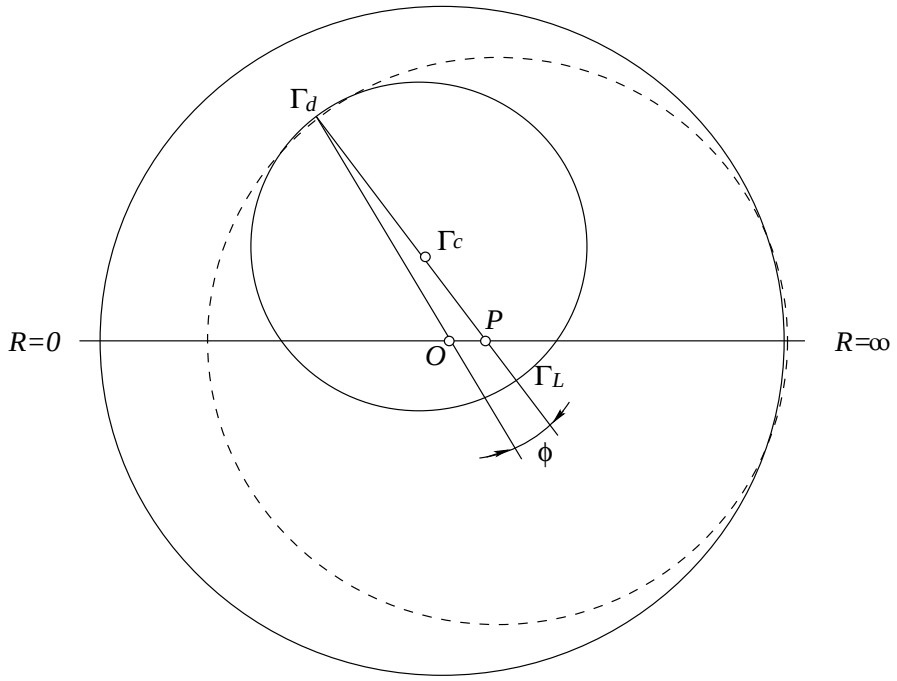

Figure 3.13 Input reflection coefficient as a function of frequency for lossy coupling.

Q circle (solid line circle) never touches the circumference of the Smith chart, as shown in Figure 3.13. The dashed line circle is defined as the coupling loss circuit, which is tangential to both the Q circle and the border of the Smith chart. Point P, as marked in Figure 3.13, is the center of the coupling loss circle. Point O is the center of the Smith chart. The diameter of the coupling loss circle is denoted d_2, which can be computed from the magnitude of the detuned reflection coefficient $|\Gamma_d|$ and the angle ϕ as

$$d_2 = \frac{1 - |\Gamma_d|^2}{1 - |\Gamma_d| \cos \phi} \ . \tag{3.71}$$

The normalized impedance at point C on the constant resistance circle is R_s/R_c. From the Smith chart basics [5], the diameter of the coupled loss circle can be written as

$$d_2 = \frac{2}{1 + \dfrac{R_s}{R_c}}. \tag{3.72}$$

Using Equations 3.60a, 3.60b, and 3.63, d_2 then becomes

$$d_2 = \frac{2}{1 + \frac{k_2}{k_1}}. \tag{3.73}$$

Solving the combination of Equations 3.71 and 3.73, k_1 and k_2 are obtained in terms of d and d_2 as

$$k_1 = \frac{1}{2\left(\frac{1}{d} - \frac{1}{d_2}\right)}\ , \tag{3.74a}$$

$$k_2 = \frac{\frac{2}{d_2} - 1}{2\left(\frac{1}{d} - \frac{1}{d_2}\right)}\ . \tag{3.74b}$$

According to Equation 3.63, the total coupling coefficient can be evaluated in terms of d and d_2 as

$$k = \frac{1}{\frac{d_2}{d} - 1}\ . \tag{3.75}$$

Using the normalized variable from Equation 3.53, the input reflection coefficient in Equation 3.68 can be written in a form ready for the curve fitting

$$\Gamma_i = \frac{jQ_L\Gamma_d 2\frac{\omega - \omega_L}{\omega_0} + \Gamma_d + de^{j\gamma}}{jQ_L 2\frac{\omega - \omega_L}{\omega_0} + 1} = \frac{a_1 t + a_2}{a_3 t + 1}\ . \tag{3.76}$$

Q_L is solved as

$$Q_L = \mathrm{Im}(a_3), \tag{3.77}$$

the detuned reflection coefficient is

$$Q_L = \frac{a_1}{a_3}, \tag{3.78}$$

and the reflection coefficient at ω_L is

$$\Gamma_L = a_2. \tag{3.79}$$

The center of the Q circle can be computed by

$$\begin{aligned} \Gamma_c &= \frac{\Gamma_d + \Gamma_L}{2} \\ &= \frac{a_3^* a_2 - a_1}{a_3^* - a_3} \ . \end{aligned} \tag{3.80}$$

The diameter of the Q circle is then obtained by

$$\begin{aligned} d &= 2|\Gamma_c - \Gamma_L| \\ &= 2\frac{|a_2 a_3 - a_1|}{|a_3^* - a_3|} \ . \end{aligned} \tag{3.81}$$

The diameter d of the coupling circle can be computed from Equation 3.71. The angle ϕ in this equation is computed as

$$\phi = \phi_1 - \phi_2, \tag{3.82}$$

where

$$\phi_1 = \tan^{-1}\left[\frac{\mathrm{Im}\Gamma_d}{\mathrm{Re}\Gamma_d}\right] \ , \tag{3.83a}$$

$$\phi_2 = \tan^{-1}\left[\frac{\mathrm{Im}(\Gamma_c - \Gamma_d)}{\mathrm{Re}(\Gamma_c - \Gamma_d)}\right] \ . \tag{3.83b}$$

With d and d_2 already known, the total k can be evaluated by Equation 3.75. Then Q_0 is computed by Equation 3.36.

3.3 Effect of Surface Roughness

The loss of the resonant cavity is caused by the flow of the induced currents in the metal walls. The general formulas for the loss are derived with the assump-

tion that the metal surfaces of the structure are perfectly smooth, and thus the conductivity is independent of frequency and is equal to that of the bulk metal. In reality, the presence of surface roughness introduces more power losses from the conductor walls. The magnitude of the loss depends on the relationship between surface roughness dimensions and the skin depth of the field penetration into the metal surface, which decreases as the frequency increases. As the operating frequency of the circuit pushes higher, the effect of the surface roughness on conductor loss becomes more important. At low frequencies, the roughness dimensions are small compared to the skin depth, and only a small fraction of the total current is affected by the roughness, resulting in small additional power loss compared to the ideal smooth conductor. However as the frequency increases, the skin depth decreases and approaches the roughness dimensions. In this case, the current and fields are concentrated near the surface of the conductor, and a larger fraction of the total current is forced to follow the roughness profile, resulting in more power loss.

A theoretical investigation of surface roughness on the current losses was made in [39] at microwave frequencies. The approach in [39] is applicable to the case where the roughness dimensions are small comparable to the free space wavelength and all other physical dimensions of the structure.

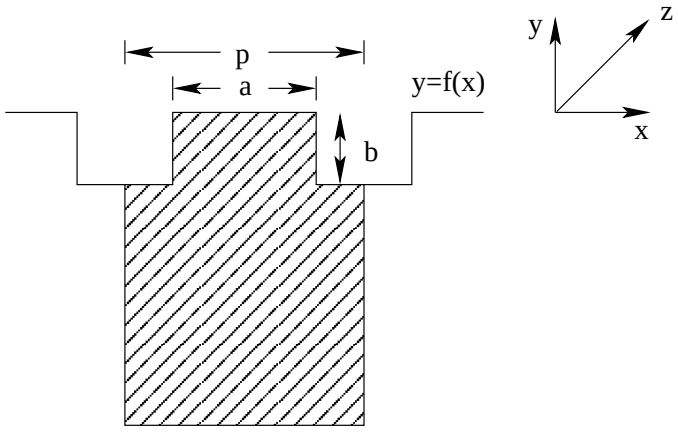

Figure 3.14 Cross section of semi-infinite conductors with rectangular surface grooves.

A part of the surface of a cavity resonator is modeled by a piece of semi-infinite conducting metal in the z direction, as shown in Figure 3.14 [39], with thickness extending from $y = f(x)$ to $y = -\infty$. The surface profile cross-section in the x-y plane is represented by function $f(x)$, which is typically irregular but could be simplified as a periodic function, for instance as shown in Figure 3.14 with groove period p. Assume that an alternating magnetic field $\mathbf{H} = \hat{z}H_z e^{j\omega t}$ is impressed in the z direction at the surface of the periodic roughness profile, so that the currents are induced parallel to the xy plane. With the assumption that the groove is much smaller compared to the free space wavelength and the other physical dimensions of the structure, the variation of H_z with z could be neglected. For roughness features that are very small in height compared to the dimensions of the apparatus, the impressed field variation along the roughness surface profile could be neglected. Therefore, H_z can be treated as a constant H_0 following the surface of the conductor.

The magnetic field in a source free region satisfies the differential equation

$$\nabla^2 \mathbf{H} = -\mu\epsilon\omega^2 \mathbf{H}. \tag{3.84}$$

For a metal with finite conductivity σ, the effective dielectric constant is written as

$$\epsilon = \epsilon' - j\frac{\sigma}{\omega}. \tag{3.85}$$

Applying the effect that the conduction current is much greater than the displacement current in a good conductor, which means $\sigma \gg \omega\epsilon'$, Equation 3.84 can be written as

$$\nabla^2 \mathbf{H} = j\omega\mu\sigma \mathbf{H}. \tag{3.86}$$

Most metals can be categorized as good conductors, including gold and copper, where the approximation is valid.

Since **H** is independent of z and has only a z-component, Equation 3.86 become

$$\frac{\partial^2 H_z}{\partial x^2} + \frac{\partial^2 H_z}{\partial y^2} = \frac{2j}{\delta^2} H_z, \tag{3.87}$$

where δ is the skin depth of the conductor, and is defined as

$$\delta = \sqrt{\frac{2}{\mu\omega\sigma}} \ . \tag{3.88}$$

The numerical solution for H_z is derived using the relaxation method, which is described briefly in the Appendix A with the boundary conditions $H_z = H_0$ at the surface $y = f(x)$ of the metal, and $H_z \to 0$ as $y \to -\infty$.

In the special case of the conductor with plane surface, where $f(x) = 0$, H_z is independent of x, so that Equation 3.87 can be simplified as

$$\frac{\partial^2 H_z}{\partial y^2} = \frac{2j}{\delta^2} H_z. \tag{3.89}$$

Solving this equation, H_z is given simply as

$$H_z = H_0 e^{(-\frac{1+j}{\delta}|y|)} \ , \tag{3.90}$$

which decays exponentially with the depth of penetration beneath the conductor surface.

After Equation 3.87 is solved, the power dissipated in a given volume V of the conducting metal can be calculated by

$$\begin{aligned} P &= \frac{\sigma}{2}\int_V |\mathbf{E}|^2 dv \\ &= \frac{1}{2\sigma}\int_V \mathbf{J}\cdot\mathbf{J}^* dv \\ &= \frac{1}{2\sigma}\int_V (\nabla\times\mathbf{H})(\nabla\times\mathbf{H}^*) dv \ , \end{aligned} \tag{3.91}$$

where **J** represents the conduction current density, which is related to the electric

field density as $\mathbf{J} = \sigma\mathbf{E}$.

The integral on the right side of Equation 3.91 can be transformed into a format more suitable for power loss calculation using the procedure proposed in [39]. The transformation is performed on a cell with unit length in the z direction, with d equal to the groove period in the x direction, and infinite depth in the y direction. The transformed expression for power dissipation becomes

$$P = -\frac{1}{\sigma\delta^2}\mathrm{Im}\left[H_0^* \int_0^p \int_{-\infty}^{f(x)} H_z dx dy\right] , \tag{3.92}$$

where the integration is performed over the shaded region of Figure 3.14.

For a conductor with a plane surface, the power dissipated in the same volume cell can be derived by inserting Equation 3.90 into Equation 3.92, which gives the solution

$$\begin{aligned} P_0 &= -\frac{|H_0|^2}{\sigma\delta^2}\mathrm{Im}\left[\int_{-\infty}^{f(x)} \int_0^p e^{(\frac{1+j}{\delta}y)} dy dx\right] \\ &= \frac{|H_0|^2 p}{2\sigma\delta} . \end{aligned} \tag{3.93}$$

Based on Equation 3.92 and Equation 3.93, the ratio of power dissipated in the conductor with the grooved surface to that in the same conductor with plane surface is obtained as

$$\frac{P}{P_0} = -\frac{2}{|H_0|^2 p\delta}\mathrm{Im}\left[H_0^* \int_0^p \int_{-\infty}^{f(x)} H_z dy dx\right] . \tag{3.94}$$

Once H_z is derived using the relaxation method, the integral on the right side of Equation 3.94 is carried out by first assigning an arbitrary value to H_0, which would be cancelled out in Equation 3.94 for the power ratio.

The relative power dissipation on two-dimensional (2-D) periodic triangular and rectangular surface profiles is calculated in [39] from the H_z derived using the relaxation method. Rigorous numerical mathematical treatments of specific

profiles suggest that if roughness dimensions are comparable and not dramatically larger than the skin depth, then reasonable approximations can be made using root-mean-square (r.m.s) roughness deviation measurements from the mean surface. The exact shape of the surface roughness is also not critical, as long as the deviations are of approximately equal width and depth. The ratio of power losses in rough surface with equilateral triangular grooves to that dissipated into a smooth interface can be approximated by [6]

$$\frac{P}{P_0} = 1 + \frac{2}{\pi} tan^{-1}\{1.4(\frac{\triangle}{\delta})^2\}. \tag{3.95}$$

where $\triangle$ is the r.m.s surface roughness; δ is the skin depth. Equation 3.95 is derived by fitting the data obtained in [39] into a curve. The relative power dissipation as a function of the ratio Δ/δ of r.m.s roughness to skin depth is represented graphically in Figure 3.15. According to this calculation, comparable to the plane surface, the losses on the grooved surface are increased by about 60 percent when the r.m.s surface roughness is equal to one skin depth. At the frequency of 24 GHz, the skin depth in gold is only 0.5 μm. Thus, the power loss would be increased by 60 percent if the r.m.s roughness of the metal surface is approximately 0.5 μm.

Recently, the effect of surface roughness on the power loss in a conductor [40] was analyzed by applying a generalized impedance boundary condition for 2D conducting rough interfaces [41] [42]. The equivalent boundary condition is derived by applying the method of homogenization, which separates the microscopic (fine) and macroscopic (global) features of the problem. In this way, the field is represented by the combination of two functions, one carrying the information of fine structure, and the other carrying that of global behavior. Due to the geometry of the rough surface, the field exhibits variations with respect to the periodicity of the roughness. The total field is a function of two spacial length scales, which correspond to the incident wave and the microstructure of the roughness, respectively.

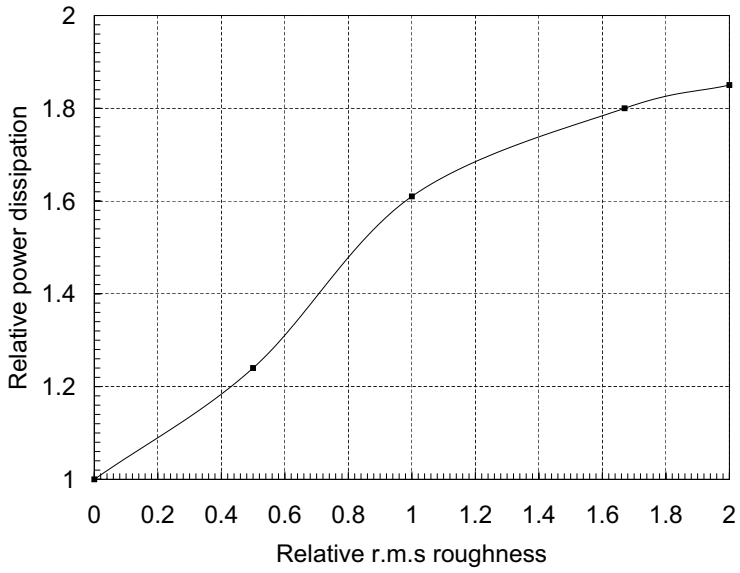

Figure 3.15 Relative power dissipation vs. rms roughness for triangular grooves transverse to the current flow.

Close to the rough surface, the total field is composed of both a boundary-layer field and an effective field. The boundary-layer field, or the localized field, is close to the surface, which is function of both small distances comparable to roughness periods and a large distance comparable to the wavelength. The effective field is a few periods away from the conductor surface, and changes significantly only over distances of the order of a wavelength. By applying the technique of homogenization to separate the boundary-layer field from the effective field, an equivalent boundary condition is derived for the effective field. Hence, the actual periodic rough surface can be replaced by an effective smooth surface applied with this equivalent boundary condition, which incorporates all the effects of the roughness profile. Then the impedance boundary condition is used to calculate the power loss associated with conducting rough interfaces. The results implemented with FEM are found to be in fair agreement with that analyzed in the classic paper [39].

3.4 Summary

This chapter introduces the software and techniques used to design, model, and evaluated the resonator and filter structures presented in this thesis work. Two available simulation tools are employed to analyze the performance of the resonator: Ansoft HFSS and QZERO. HFSS is a commercial FEM based simulator used to extract the S-parameter of the resonator in simulation. The program QZERO implements the methods discussed in this section to assist in the analysis of the microwave resonator. It determines important parameters such as quality factor and coupling coefficient by processing the data using a reflection type measurement. The additional power dissipation in the conductor due to the surface roughness is approximated in simulation by Equation 3.95, assuming equilateral triangular surface grooves, which is used to analyze the surface roughness effect on the performance of the circuit models presented in the later designs.

Chapter 4

RESONATOR DESIGN AND SIMULATION

4.1 Air-filled Resonant Cavity

The dimensions of the air-filled rectangular cavities operating at the dominant TE_{101} mode can be calculated according to the theory described in Chapter 2.

The increase of the metal conductivity on the interior of the cavity walls reduces the conductor loss, and hence directly increases the quality factor. Therefore, metals with high conductivity, such as copper and gold (assumed in this case) with typical conductivity values of 5.7×10^7 and 4.1×10^7S/m respectively, are preferred.

Q factor is optimized when the cavity is implemented with a square base. The relationship between the unloaded Q factor and the cavity dimensions for the air-filled resonant cavities operating at 18 GHz, 24 GHz, and 37 GHz are first investigated based on the theoretical calculations, assuming gold with finite conductivity but no roughness. Figure 4.1 shows the Q factor variation with the size of the cavity base, while the cavity height is constant (2 mm). For all three resonant cavities, the maximum Q is reached when the length and width of the cavity are equal (square base), which is denoted by the markers on the plot.

The resonant frequency variation with increasing cavity width/length for a 2-mm-deep square-based cavity is illustrated graphically in Figure 4.2. As the cavity dimension increases, the resonant frequency decreases. Q factor increases with increasing resonant frequency (decreasing of cavity base dimension) at the cavity height of 2 mm.

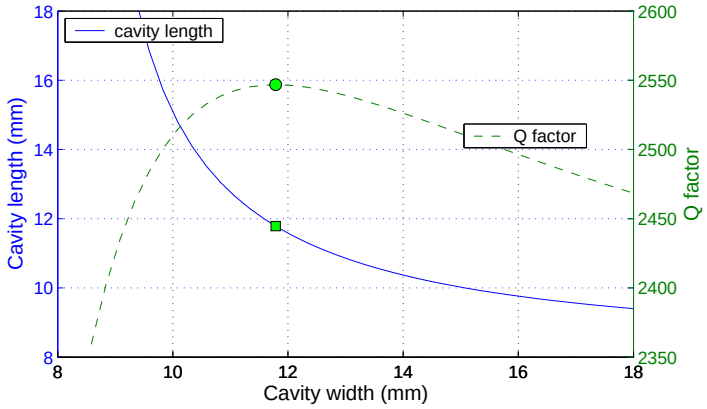

(a) 18 GHz resonant cavity.

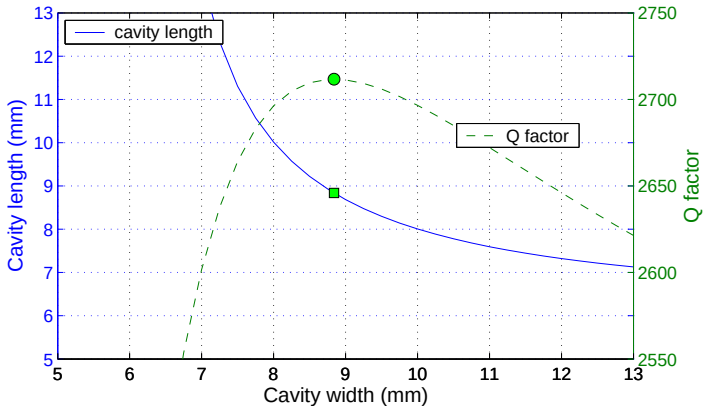

(b) 24 GHz resonant cavity.

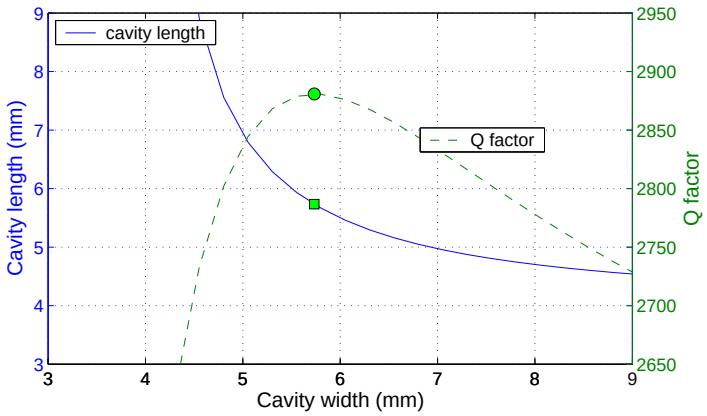

(c) 37 GHz resonant cavity.

Figure 4.1 Q variation with the size of the cavity base (2 mm deep cavity).

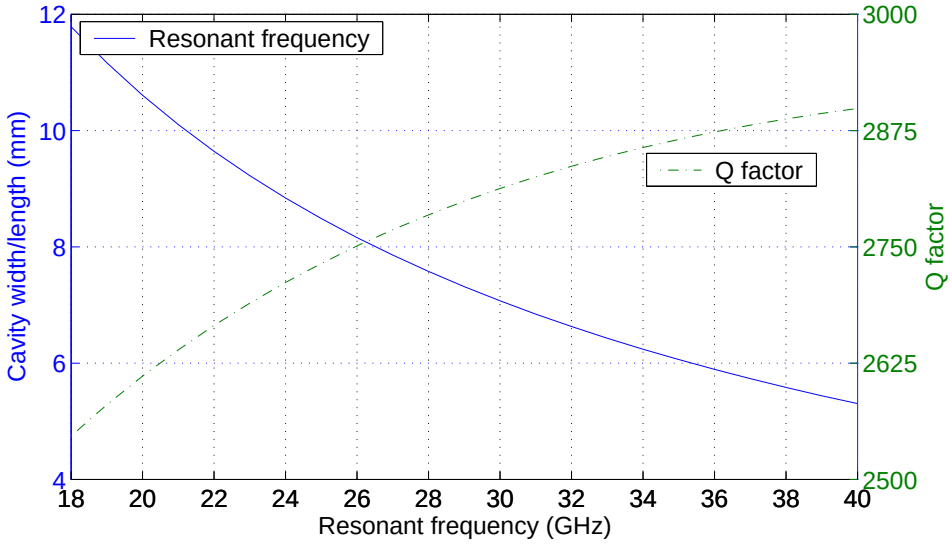

Figure 4.2 Q and resonant frequency versus cavity width/length for a 2-mm-deep square-based cavity.

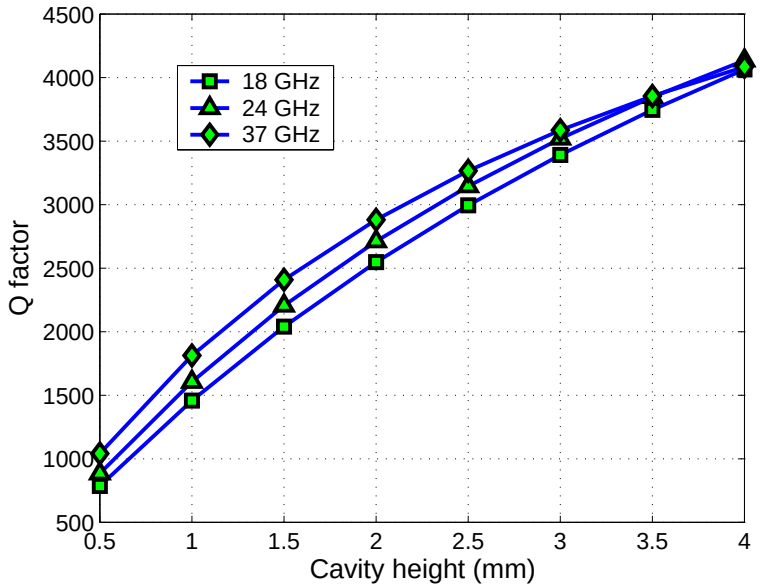

Figure 4.3 Q versus cavity height for square base cavity.

Increasing the height of the air-filled cavity can also contribute to improvement of the Q factor. The Q factor versus cavity height for square-based cavities resonant at 18 GHz, 24 GHz, and 37 GHz is examined (Figure 4.3), and Q factor is shown to increase dramatically with increasing cavity height. The base dimensions and the corresponding Q values for the 2 mm-deep cavities are summarized in Table 4.1.

Table 4.1 Base dimensions and the corresponding Q values for air-filled 2 mm-deep cavities resonant at 18 GHz, 24 GHz, and 37 GHz.

Resonant frequency	**Cavity width/length**	Q **factor**
18 GHz	11.785 mm	2546.8
24 GHz	8.839 mm	2711.7
37 GHz	5.733 mm	2880.8

4.2 Dielectric-filled Resonant Cavity

A miniaturized cavity resonator with size reduction in the lateral dimensions can be achieved by filling the cavity with a dielectric material.

The effects of dielectric filling on the resonant frequency and quality factor are shown in Figures 4.4 and 4.5, respectively. The results are obtained based on 2-mm-deep square-based cavities with base dimensions of 5.733×5.733 mm^2, 8.839×8.839 mm^2, and 11.785×11.785 mm^2, which correspond to the resonant frequencies of 18 GHz, 24 GHz, and 37 GHz, respectively, when the cavities are filled with air. According to Figure 4.4, the resonant frequency decreases as the dielectric constant of the filling material increases, which exhibits the effect of miniaturization by filling the cavity with high dielectric constant materials. For cavities with constant sizes, the quality factor decreases with increasing dielectric permittivity, as can be seen in Figure 4.5, where the Q data are obtained assuming that the dielectric material is lossless, and only the conductor loss contributes to

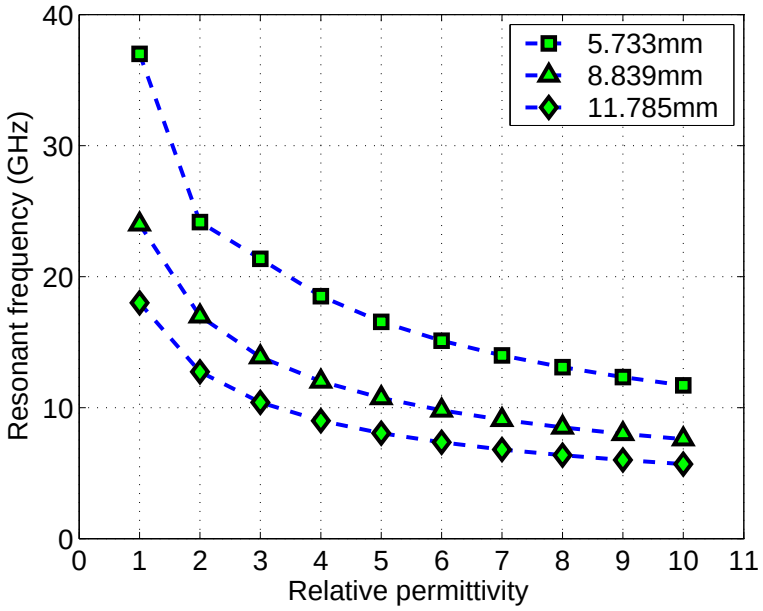

Figure 4.4 Resonant frequency versus relative permittivity for 2-mm-deep square-based cavity.

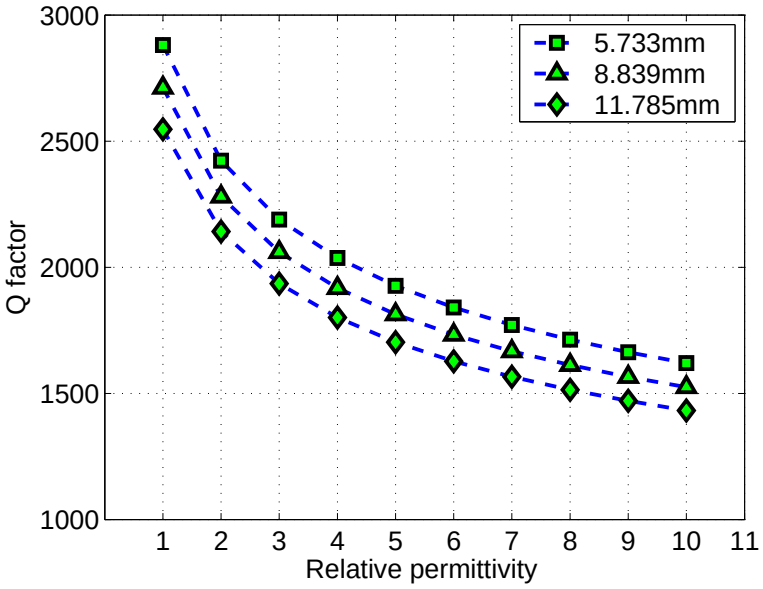

Figure 4.5 Quality factor versus relative permittivity for 2-mm-deep square-based cavity.

the Q factor.

One dielectric material that is interesting to consider is PMMA, since it is already present in the cavity during processing. A typical relative permittivity for PMMA is $\epsilon_r = 2.57$ [43]. According to Figure 4.4, the PMMA filler results in frequency shifting from 18 GHz, 24 GHz, and 37 GHz down to 11.2 GHz, 15.0 GHz, and 23.1 GHz respectively, as listed in Table 4.2. The quality factor (Q_{cond}) due to only the conductor loss is also summarized in Table 4.2. PMMA material has a relatively high loss factor of $\tan \delta = 0.0032$ [43]. When including the effect of material loss, the total Q drops substantially (see Table 4.2), indicating that the Q obtainable from PMMA-filled cavities is mainly limited by the high loss tangent of the PMMA material. However, this may still be attractive to consider in some situations since processing would be simplified considerably if the PMMA was not removed. In addition, the PMMA could provide support for structures with fine internal structure.

Table 4.2 Resonant frequency and Q values for PMMA-filled 2 mm-deep cavities.

Cavity width/length	**Resonant frequency**	Q_{cond}	**Total** Q
11.785 mm	11.2 GHz	2011.4	270.5
8.839 mm	15.0 GHz	2141.7	272.7
5.733 mm	23.1 GHz	2275.3	274.8

4.3 One-port Cavity Resonator

Based on the theoretical dimensions presented in Section 4.1, a complete cavity resonator with the external coupling circuit is designed. The proposed resonator has only one port, which is determined by its potential application as a frequency stabilizing component in an oscillator. Figure 4.6 shows the top view and the cross section view of the one-port cavity resonator. The cavity is constructed of a five-sided metal box at the bottom of the structure. A hollow cavity is chosen

for this design in order to get optimal Q as any dielectric filling materials would introduce extra loss (see Section 4.2). The top plane of the cavity is formed by a separate metallized substrate positioned on top of the box, which is patterned with the coupling circuit. The cavity is coupled to the outer circuit by a small rectangular slot on the ground plane of the substrate. A 50 Ω microstrip feed line connects to the source, and excites the desired TE_{101} mode in the cavity through the slot.

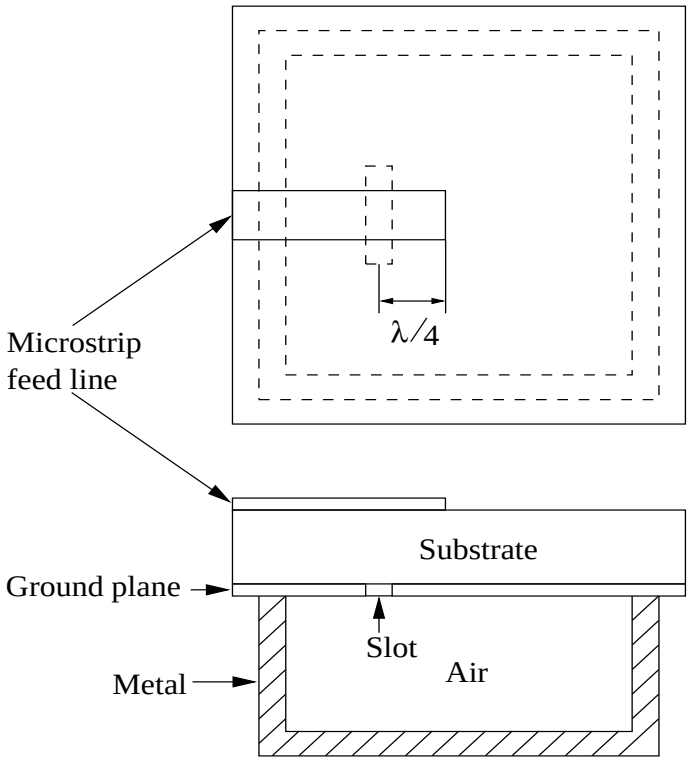

Figure 4.6 Structure of the proposed rectangular cavity resonator.

Substrates are the dielectric material upon which the conductors and the hybrid elements are built to produce the required circuit. General characteristics such as relative permittivity, loss factor, substrate surface roughness, thermal conductivity, and cost are important considerations in choosing substrates. Two basic types of substrate are used for hybrid MICs - “hard” substrates and “soft” substrates.

In the hard substrates category, aluminum-oxide ceramic (Al_2O_3), which is also called "alumina", is common in microwave technology. It is a moderately expensive substrate but still the least expensive of the hard substrates. Alumina has a high relative permittivity, usually 9 to 10, which results in a smaller circuit size and higher levels of circuit integration. Alumina also has low loss factor, which decreases the dielectric losses of the MICs. The surface roughness of a finely polished alumina substrate is on the order of 40 nm, which results in low conductor losses due to the current flow on the metal surface, and makes it an excellent candidate for constructing the sixth side of the cavity resonator. The thermal conductivity of alumina is relatively high, which allows larger heat dissipation from components (e.g., power transistors). The disadvantage of using alumina is the high cost of circuit fabrication. The conductors on the substrate are produced using expensive thin-film technology. This technology requires significant investment in production equipment. Alumina is also very hard and brittle, and is difficult to machine. Cuts can be made with a diamond saw or a laser; holes can be drilled with a laser or a carbide tool.

Soft substrates are available in a wide range of relative permittivities depending on material. The substrate materials can be pure plastics or plastics loaded with glass fibers or ceramic powder. Soft substrates usually use copper for their conductors. The laminates are copper-coated on both sides. The copper layer is usually fabricated either by rolling or electro-chemical deposition, which results in relatively high surface roughness with typical values on the order of several hundred nanometres. Soft substrates provide the simplest method of producing MICs. All that is required is a high resolution photoetching system to permit structure fabrication on the copper-clad laminates. Soft substrates are also easy to machine. Except for relative permittivity, which can be made as high as that of alumina, other characteristics such as loss factor, the substrate surface roughness and thermal conductivity are worse than those of alumina, but still acceptable for many applications. The advantage of using soft substrates is that the cost for

MIC fabrication is very low, because the circuits can be made in the laboratory without the need for complex processing equipment.

The electromagnetic fields propagating in microstrip lines should be Quasi-TEM mode, for which the longitudinal field components are required to be small compared with the transverse (to the direction of propagation) field components. Thinner substrate has to be used for this design to guarantee the Quasi-TEM mode transmission. Therefore, it is necessary to ensure that the cutoff frequency of the non TEM mode is much higher than the operating frequency of the circuit [6]. The cutoff frequency of the first hybrid mode can be roughly calculated by [6]

$$f_g = 0.4 Z_L / h; \tag{4.1}$$

where Z_L is the characteristic impedance of the microstrip line in Ω; h is the substrate height in mm; f_g is in GHz.

Above the cutoff frequency, hybrid modes, which have longitudinal components of the same order as the transverse components for either electric or magnetic fields, exist in the substrate. The field distribution driven by a microstrip line higher mode is similar to the rectangular waveguide mode. Microstrip hybrid higher modes have hardly any technical uses. The useful frequency range of microstrip lines is the region where only the quasi-TEM mode propagates.

The properties of the one-port resonator are analyzed using a 24 GHz resonator model as a demonstration tool. An HFSS model as shown in Figure 4.6 is constructed and simulated. It is assumed that the sixth side of the cavity is formed by a 0.4 mm-thick alumina substrate with $\epsilon_r = 9.8$ and $\tan \delta = 0.0004$, on which the coupling mechanism is patterned. The coupling slot is placed at 1/4 of the cavity length. The length of the open-ended microstrip feed line is $\lambda/4$ measured from the center of the slot. The detailed dimensions of the 24 GHz resonator are shown in Figure 4.7. In order to compensate for the frequency shifting caused by the effect of the external loading circuit, the base size of the cavity is 8.829

mm × 8.829 mm, which is slightly reduced compared with the dimension from the theoretical calculation shown in Table 4.1. The conductor in the resonator, including the interior walls of the cavity, the microstrip line and the ground plane of the alumina substrate, are assumed to be gold, with conductivity of 4.1 $\times 10^7$ S/m. The criteria of convergence of the HFSS simulation is specified by Maximum Delta S. It is the change in the magnitude of the S-parameters between two consecutive passes. If the magnitude and phase of all S-parameters change by an amount less than the Maximum Delta S per pass value from one iteration to the next, the adaptive analysis stops. Otherwise, it continues until the requested number of passes is completed. The Maximum Delta S for the resonator model shown in Figure 4.7 is specified as 0.005. The number of tetrahedra for such a structure is typically on the order of 21000.

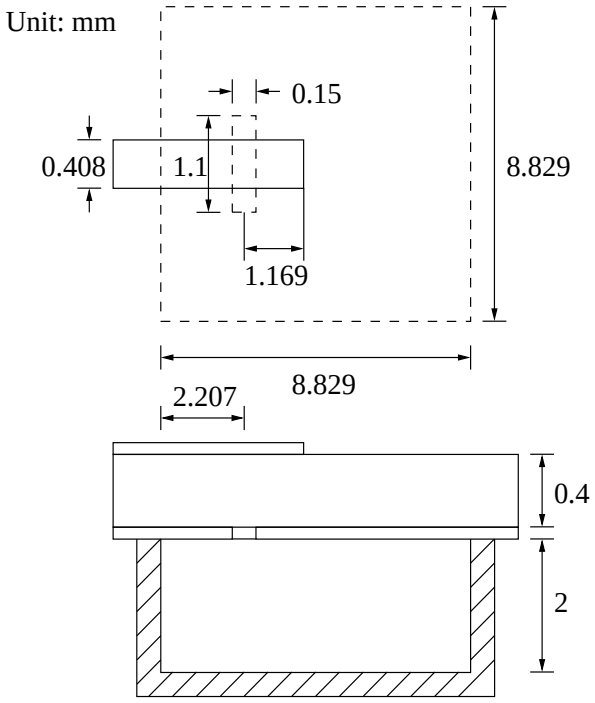

Figure 4.7 Schematic of the 24 GHz cavity resonator.

The input S-parameter versus frequency is plotted on the cartesian plane and the Smith Chart in Figures 4.8(a) and 4.8(b), respectively. As indicated in the

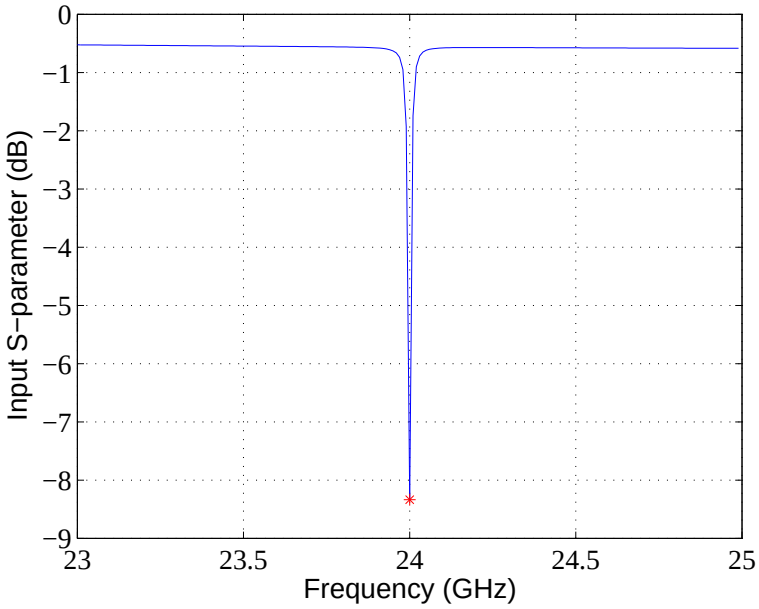

(a) Simulated S_{11} magnitude response of the 24 GHz cavity resonator;

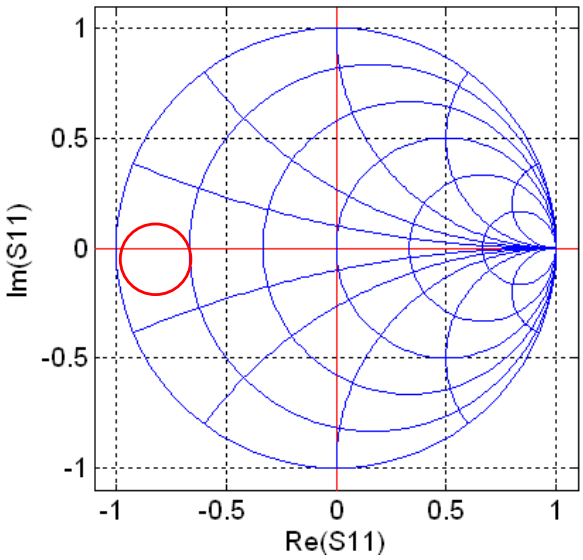

(b) Simulated S_{11} response of the 24 GHz cavity resonator on the Smith chart.

Figure 4.8 Simulated S-parameter for 24 GHz cavity resonator.

previous chapter, the simulated input reflection coefficient, S_{11}, describes an exact circle when plotted on the Smith Chart as a function of frequency within the vicinity of resonance (see Figure 4.8(b)). The resonance occurs where S_{11} reaches its lowest value, which is 23.999 GHz in Figure 4.8(a). Using the measurement method described in Section 3.2, the loaded Q of the resonator is found to be $Q_l = 2416 \pm 26$, and the unloaded Q, Q_u, is equal to 2819 ± 39. The slightly higher Q_u, compared with the value of 2711.7 as theoretically calculated in Table 4.1 for a cavity height of 2 mm, is reasonable since the lateral dimensions of the cavity are slightly smaller than that used to derive the calculated Q_u.

Figure 4.9 shows the electric field plot in horizontal and vertical planes for the dominant resonance mode (24 GHz). The field pattern also matches quite well with that of the TE_{101} resonant mode of an ideal square cavity with a similar size described in Section 2.2.2.

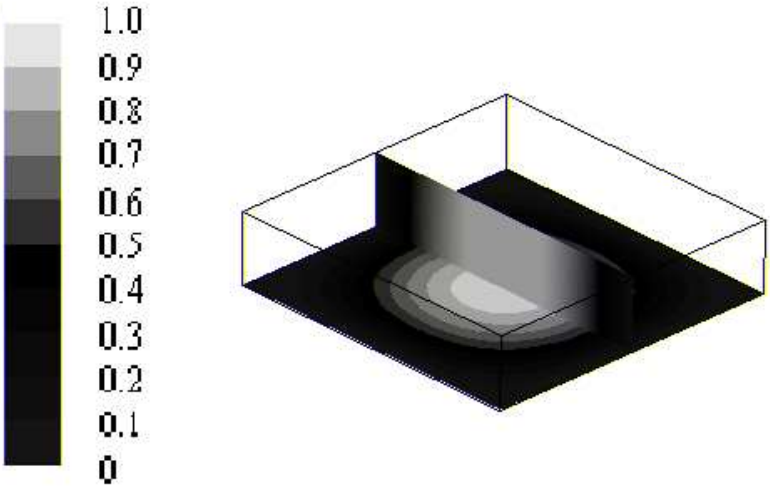

Figure 4.9 Simulated electric field density for the dominant resonance mode (24 GHz).

The depth of the cavity is an important parameter of the cavity resonator, which strongly affects the quality factor: the deeper the cavity, the greater the quality factor. The resonator model is built and simulated using HFSS, and the unloaded Q is extracted using the reflection type measurement described in Chapter 3. The loaded and unloaded Q dependency on the cavity depth is plotted

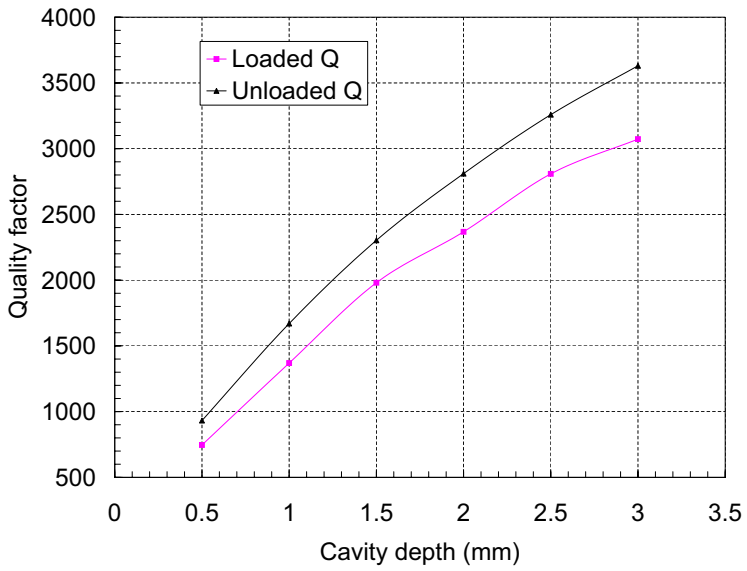

Figure 4.10 Simulated Q factor as a function of cavity depth for 24 GHz resonator.

in Figure 4.10. Although the resonator model is simulated only up to 3 mm cavity depth, which is an obtainable value for LIGA fabrication, the Q factor is expected to increase until the cavity height reaches the value of its width/length. The simulated unloaded Q matches well with the prediction of the theoretical calculation shown in Figure 4.3, which verifies the validation of the Q factor measurement method described in Section 3.2.

The degree of coupling of the electromagnetic energy between the external and resonant circuit is controlled by the slot size on the ground plane. The simulation is run for a slot with constant width of 0.15 mm, and varying the slot length. The coupling coefficient k is plotted versus slot length in Figure 4.11. Second order polynomial interpolation is used to fit the HFSS data to a curve. The coupling coefficient k increases with increasing slot length. According to Equation 2.12, the loaded Q factor, Q_l, decreases with k increasing. This relationship between the coupling coefficient and loaded Q is confirmed by the simulation shown in Figure 4.12. In addition, variation of the slot size results in changing the impedance representing the coupling mechanism, and therefore affects the resonant frequency

of the loaded resonator. The resonant frequency corresponding to slot length variation is given in Table 4.3. Comparing the results in Figure 4.11, Figure 4.12 and Table 4.3, it can be concluded that the slot size has a stronger effect on the loaded quality factor and coupling coefficient than on the resonant frequency of the resonator.

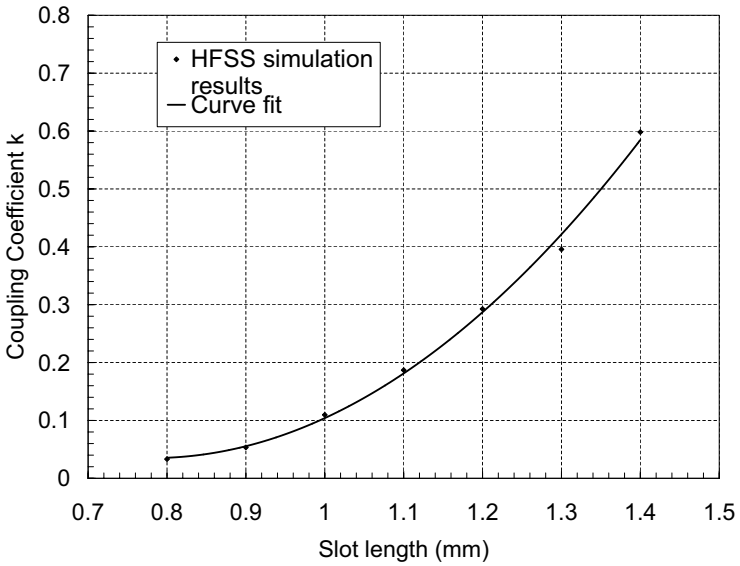

Figure 4.11 Coupling coefficient k as a function of slot length for 24 GHz resonator, curve fit to HFSS simulation result.

Table 4.3 Resonant frequency corresponding to slot length variation for 24 GHz resonator.

Slot length (mm)	f_{res} (GHz)
0.8	24.0024
0.9	24.0023
1.0	24.0010
1.1	23.9994
1.2	23.9982
1.3	23.9969

The amount of coupling between the air cavity and the microstrip feed line is also controlled by the position of the slot. The variation of the coupling coefficient

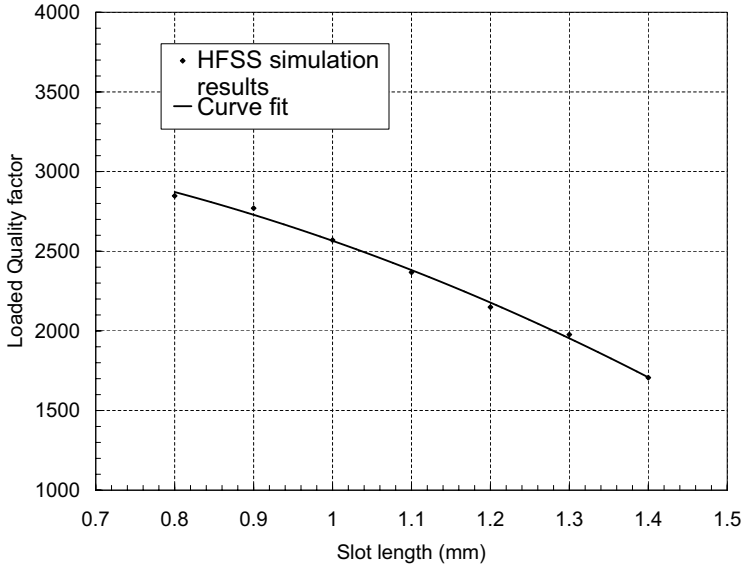

Figure 4.12 Loaded Q as a function of slot length for 24 GHz resonator, curve fit to HFSS simulation result.

k with the position of the slot is shown in Figure 4.13. Zero on the x coordinate corresponds to the position where the center of the slot is located at 1/4 of the length of the cavity, which is also the spot where the slot is $\lambda/4$ relative to the end of the microstrip feed line. Negative numbers indicate that the slot is moving towards the input port, and positive numbers mean that the slot is moving away from the input port. The coupling coefficient k increases until it reaches the maximum at the location where the microstrip feed line is short circuited and maximum current is provided. k then decreases when the slot is out of position of the point, since the coupling of the electromagnetic field is decreased as the slot position moves out of the $\lambda/4$ location relative to the end of the microstrip feed line.

4.4 Silicon-based Cavity Models

The simulation results presented in Section 4.3 are derived on the assumption that the metal surfaces are perfectly smooth, and bulk metal conductivity is used in the HFSS models. In reality, surface roughness is a dominant factor and de-

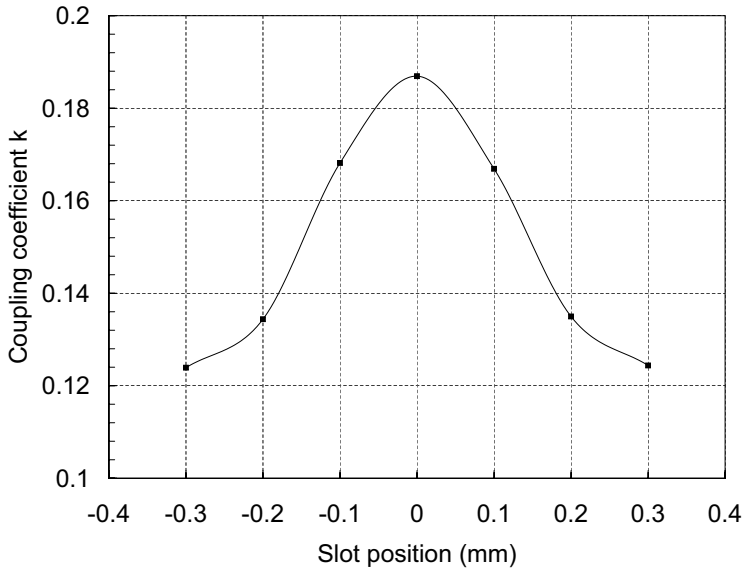

Figure 4.13 Coupling coefficient k as a function of slot position for 24 GHz resonator.

pends on fabrication technology. In this section, cavity models incorporating the effect of metal surface roughness are built and simulated.

To explore the effect of sidewall roughness on Q_u with increasing frequency, 2 mm-deep gold resonant cavity models operating at 18 GHz, 24 GHz, and 37 GHz without external coupling circuits are simulated. The effect of surface roughness is considered in the models by a corresponding reduction in the metal conductivity calculated using Equation 3.95. Triangular grooved surface profiles were assumed on the sidewalls, and 40 nm surface roughness, which is a typical value for polished Al_2O_3 substrates that would form the sixth side of the cavity, was assumed on the top and bottom of the cavity. The simulated Q_u versus r.m.s sidewall roughness for cavity models resonant at the three frequencies is shown in Figure 4.14. For all three frequencies, Q_u decreases slightly when the r.m.s roughness is within 40 nm, and then decreases rapidly with increasing surface roughness. Also Q_u decreases much more rapidly at the higher frequency of 37 GHz due to decreased skin depth effects, suggesting that surface roughness is even more critical at higher microwave and millimetre-wave frequencies.

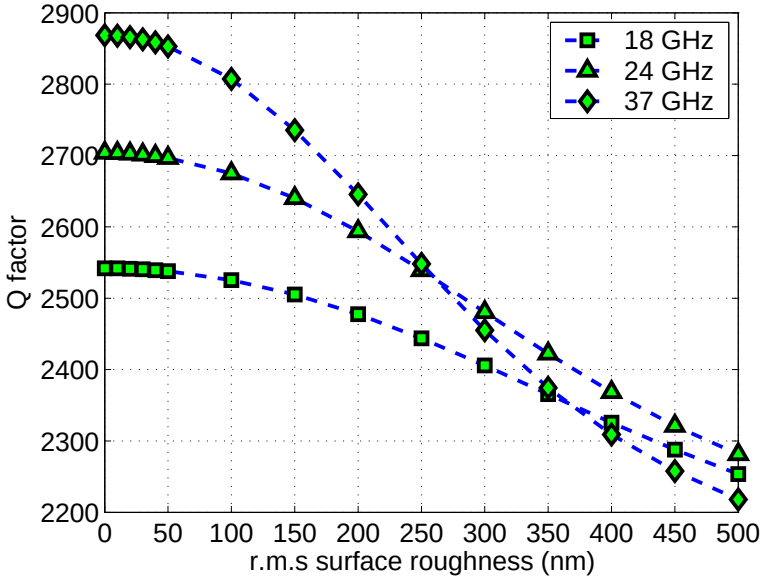

Figure 4.14 Q_u versus r.m.s sidewall roughness for the resonant cavity model with vertical sidewalls.

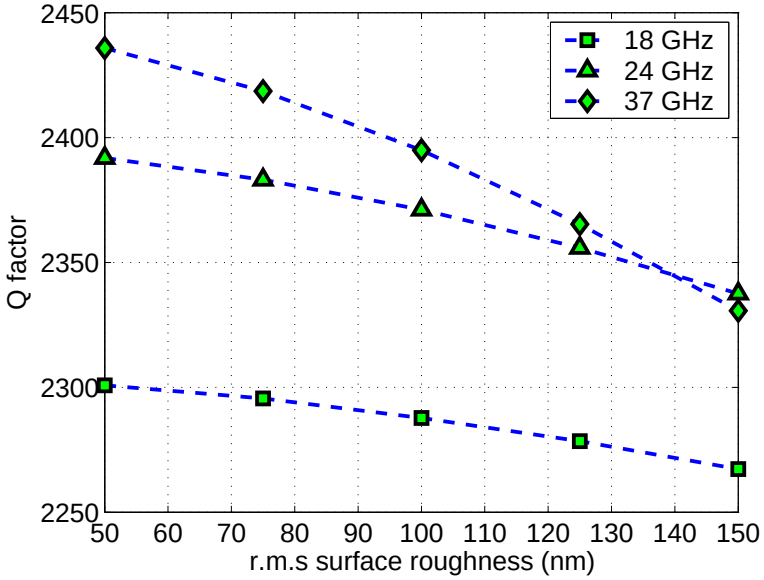

Figure 4.15 Q_u versus r.m.s sidewall roughness for anisotropic wet etching model (2 mm depth).

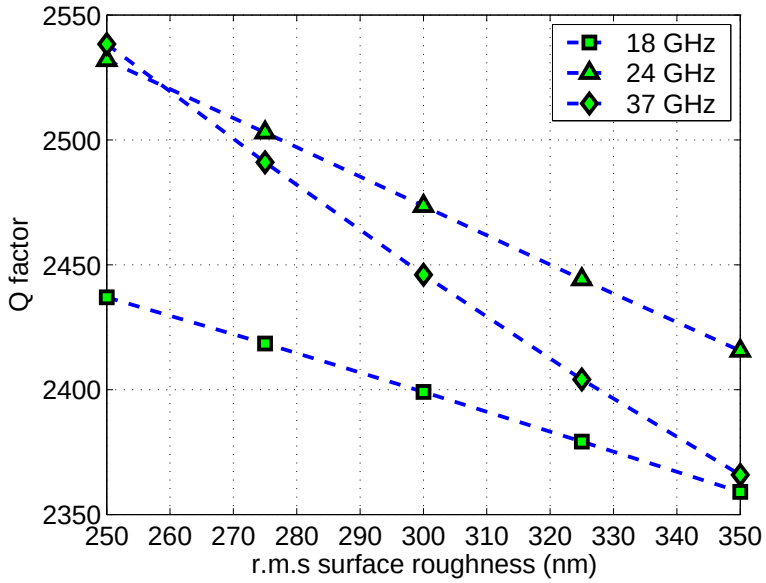

Figure 4.16 Q_u versus r.m.s sidewall roughness for deep RIE model (2 mm depth).

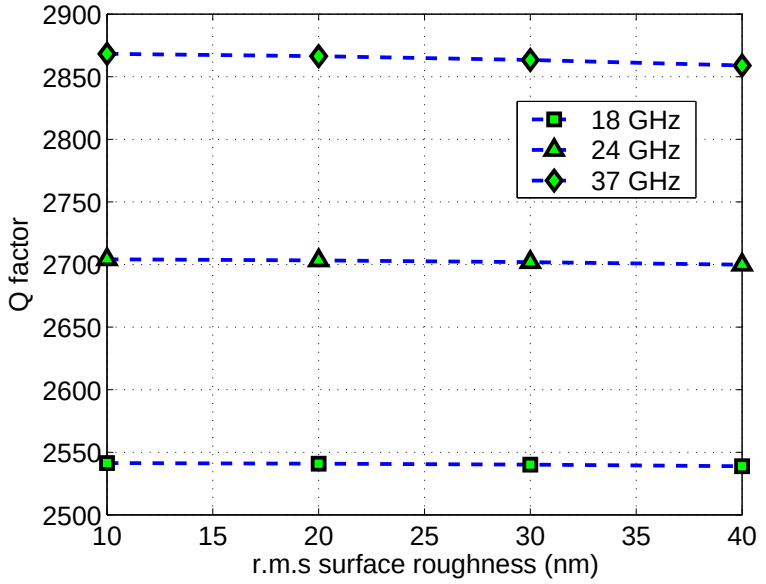

Figure 4.17 Q_u versus r.m.s sidewall roughness for LIGA model (2 mm depth).

In order to investigate the relative Q_u that could be obtained using different fabrication processes, several resonant cavity models representing different fabrication techniques were studied. The r.m.s surface roughness resulting from silicon etching varies with processing conditions. Typically, the r.m.s roughness after anisotropic wet etched (111) silicon ranges from several tens of nanometres to more than 100 nm [44]. The average sidewall roughness after deep RIE etching for an etch depth of 500 μm is typically a few hundred nanometres [45]. The models assume the underlying surface structure (silicon or PMMA) governs the roughness of deposited surface metal and no additional roughness from the deposition process is considered. The resulting Q_u versus r.m.s roughness for the anisotropic wet etching model, deep RIE model, and LIGA model resonant at three frequencies is plotted over typical roughness ranges expected from these processes in Figure 4.15, Figure 4.16, and Figure 4.17, respectively. Both the silicon wet etching model and the deep RIE model were assumed to be constructed by four 500-μm-thick silicon wafers stacked together to provide a comparable cavity depth to the LIGA model. The sidewall profiles for the cavity models representing different fabrication processes are sketched in Figure 4.18. The 54.7^o sidewall slope of each wafer and "sawtooth" cross section of the cavity were considered in the anisotropic wet etching model. A sidewall undercut of 18.5 μm at 500 μm depth [14], which results in a sidewall slope of 87.88^o, was incorporated in the deep RIE model. The profile of side walls for the LIGA model is slightly "well" shaped, with larger dimensions at the bottom than at the top. The slope of sidewalls is typically 89.925^o for a 2-mm-tall structure [46]. The base dimensions of all these models were adjusted to make the cavities resonant at 18, 24, and 37 GHz, respectively. Compared with the result shown in Figure 4.14 from the cavity models with perfectly vertical sidewalls, the Q drops by about 300 for the silicon anisotropic wet etching model due to the effect of sloped sidewalls. For the deep RIE model, the advantage of the relatively vertical sidewalls over anisotropic wet etching model is diminished by the relatively high surface roughness, especially

at 37 GHz, at which Q_u becomes comparable while the skin depth effects begin to dominate. The result from the LIGA model in Figure 4.17 shows considerably better performance in Q_u than the other models, due to the near vertical sidewalls and low surface roughness.

(a) Anisotropic wet etch profile.

(b) Deep RIE etch profile.

(c) LIGA profile.

Figure 4.18 Sketch of sidewall profiles for the cavity models representing different fabrication processes.

As shown in Section 4.1, Q improves with increasing cavity height. To compare the quality factor that could be obtained by the silicon etching and LIGA fabrication methods, simulations are performed to explore the relationship between Q factor and cavity height based on different cavity models.

The simulation results for the silicon wet etching model, deep RIE model, and LIGA model at 37 GHz are plotted in Figures 4.19, 4.20, and 4.21, respectively. In order to make it easy and convenient to compare, the results are also tabulated in Table 4.4. For cavities made by silicon micromachining processes, the sloped sidewalls from the wet etching process, and the relatively high sidewall roughness from the deep RIE process result in almost the same degree of Q degradation, which can be concluded from the close Q values at different cavity heights. Also, the advantage of LIGA fabrication over silicon micromachining is not dramatic at low cavity heights, such as below 1 mm. As the cavity height increases, the

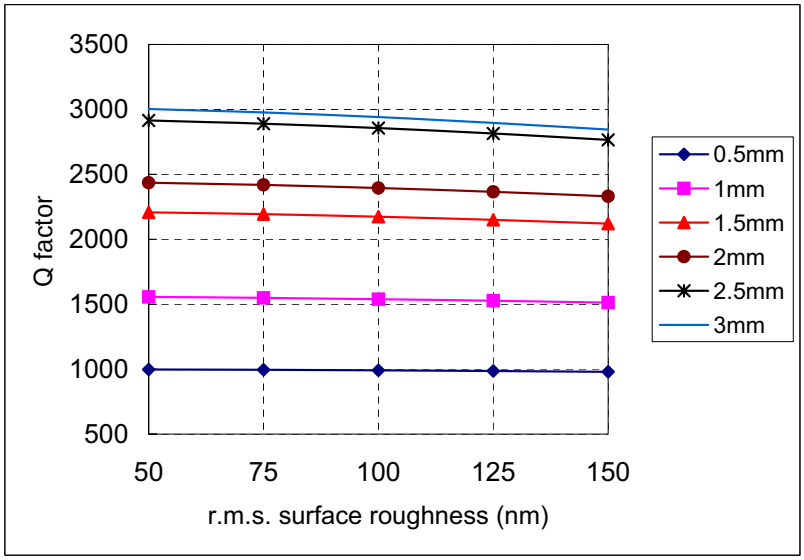

Figure 4.19 Q versus r.m.s. roughness for various cavity heights for anisotropic wet etching model at 37 GHz.

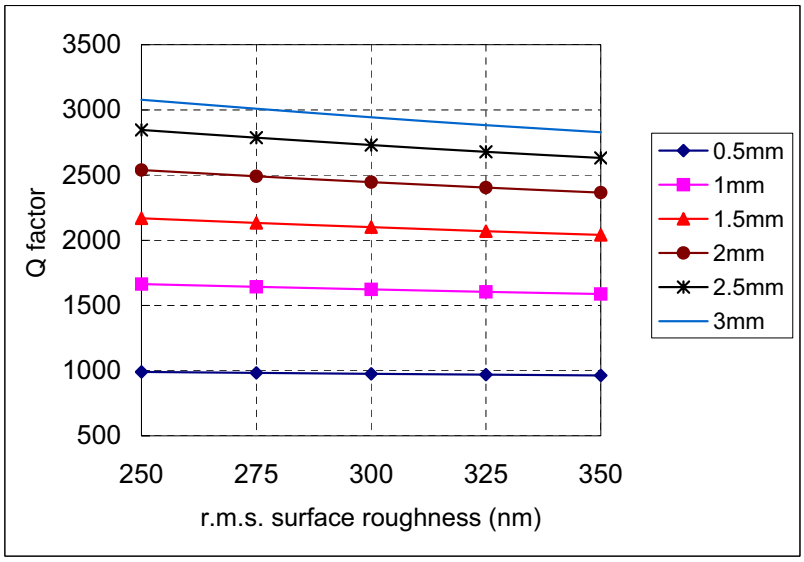

Figure 4.20 Q versus r.m.s. roughness for various cavity heights for deep RIE model at 37 GHz.

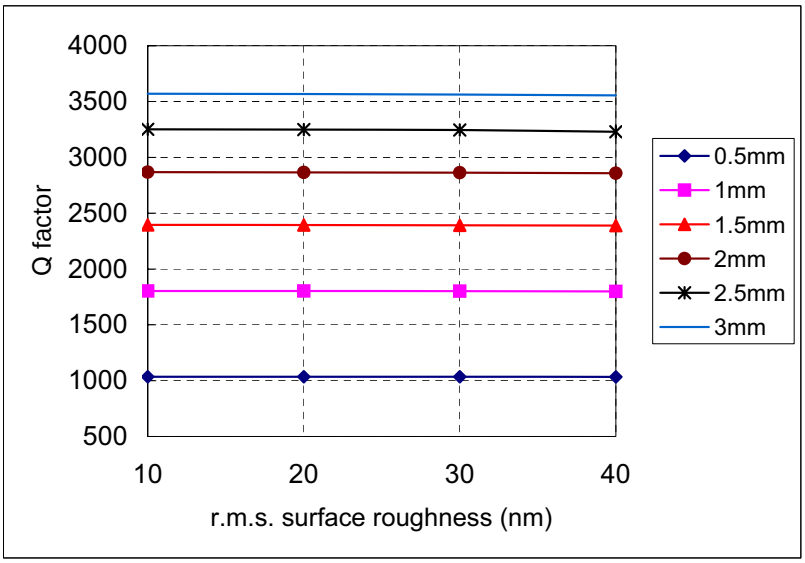

Figure 4.21 Q versus r.m.s. roughness for various cavity heights for LIGA model at 37 GHz.

effect of sidewall profile and roughness dominates, and the improvement in Q by adopting the LIGA technique becomes more significant.

Table 4.4 Q versus cavity height for different cavity models at 37 GHz.

Height	Wet etching model	Deep RIE model	LIGA model
0.5 mm	980-998	963-990	1034-1035
1 mm	1512-1556	1587-1663	1780-1803
1.5 mm	2121-2207	2041-2186	2389-2396
2 mm	2331-2436	2366-2538	2858-2868
2.5 mm	2765-2915	2631-2846	3230-3252
3 mm	2844-3003	2828-3078	3556-3570

As observed from a fabricated LIGA cavity test structure, the top dimensions of the PMMA structure after X-ray lithography shrink slightly, on the order of 12 μm in the x direction 16 μm in the y direction measured at the top of a 2-mm-thick PMMA cavity structure. Also, the shrinkage is found to be somewhat independent of the cavity size in the lateral dimensions. These shrinkage effects on resonant frequency and Q_u are examined using a 2-mm deep cavity resonant at 24 GHz as

an example. Figure 4.22(a) shows the relationship for a square top cavity, with equal cavity width and length variation. In other words, the cavity shrinks but the top remains square. Figure 4.22(b) shows the relationship by keeping the cavity width nominal while changing the cavity length. In this case, the bottom of the cavity is assumed to be square, but the top after shrinkage becomes rectangular. In both figures, the x-axis represents the percentage of shrinkage in the lateral dimensions relative to nominal values. The resonant frequency in both cases increases as expected with the dimension shrinkage due to a decrease in cavity volume. At 0.2% shrinkage, which is comparable to that of the LIGA fabricated PMMA cavity structure, the resonant frequency increases by about 0.086% for even shrinkage case, and 0.042% for uneven shrinkage case. The shrinkage effect on Q_u is more complicated. The frequency increasing with cavity shrinkage results in conductivity reduction, which tends to increase the power loss per unit area. However, the total area of the cavity walls varies with the volume shrinkage. The surface area of the sidewalls, assumed to have 30 nm roughness, gets slightly bigger, while the top dimension, assumed to have 40 nm roughness, gets slightly smaller, which leads to Q variation in opposite directions. The irregular shape of the cavity other than the rectangular may also affect the electric and magnetic field distribution inside the cavity, and thus the amount of total stored energy. As the result of all the aspects mentioned above, Q presents very slight fluctuations with the dimension shrinkage.

Three cavity resonator models incorporating the effect of surface roughness and size shrinkage are simulated using HFSS. Q_u is extracted from the loaded circuit using a reflection type measurement based on the simulated S_{11}. The resulting resonant frequency and Q_u are summarized in Table 4.5. The size shrinkage on the top of the cavities, ranging from 0.1% to 0.3% relative to the nominal base dimensions of the three models, results in a slight shift of resonant frequencies towards higher values, and is also consistent with the unloaded simulations shown in Figure 4.22(a) and 4.22(b). The simulated Q_u extracted from the loaded circuit

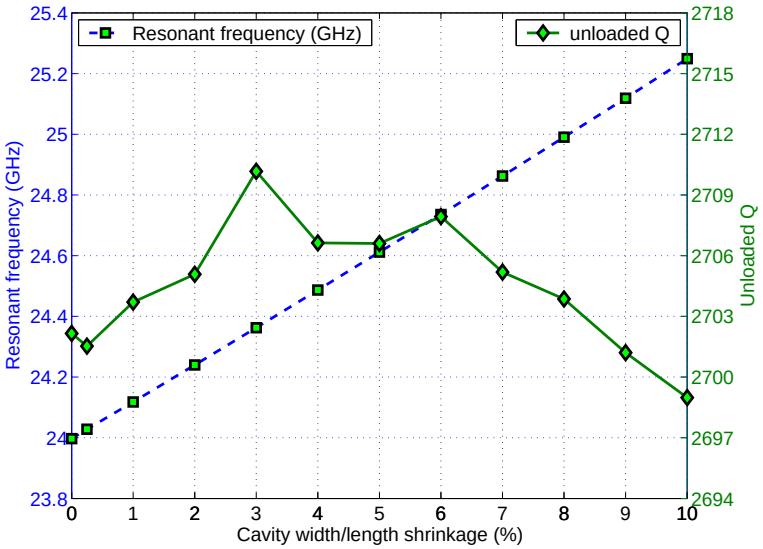

(a) Even shrinkage.

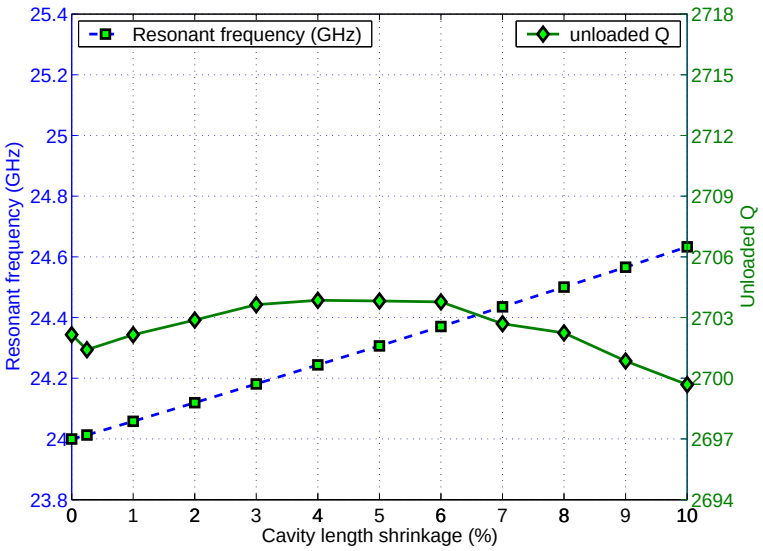

(b) Uneven shrinkage.

Figure 4.22 Q_u and resonant frequency variation with the top size of the cavity at 24 GHz (2-mm depth).

are also close to those derived from theoretical calculation based on resonant cavities with plain gold surfaces as plotted in Figure 4.3, which demonstrates the potential of realizing high Q cavity resonators using the LIGA technique.

Table 4.5 Simulated LIGA cavity resonator parameters.

Shrinkage		Resonant frequency (GHz)	Q_u
x direction	y direction		
0.102%	0.136%	18.0012	2536.3 ± 12.5
0.136%	0.181%	24.0026	2684.2 ± 7.2
0.210%	0.279%	37.0013	2783.4 ± 9.3

4.5 LTCC Cavity Models

During the last few years, many studies have proven that an electromagnetic band-gap (EBG) structure can be employed to replace a fully conducting side-wall structure to realize a cavity resonator [47] [48] [49] [50]. The periodic arrangements of metallic-posts form a structure that stops the propagation of electromagnetic waves for certain frequency regions, and thus can replace the solid metallic side-walls.

LTCC is a technique to implement a low-cost EBG cavity resonator. Rows of vias can be easily punched, and the metallized via posts construct the sidewalls of the cavity. This structure introduces extra leakage loss, which is the energy that escapes through the EBG lattice. The total unloaded Q, Q_t, of an EBG resonator is composed of three factors: conductor loss, dielectric loss, and leakage loss, and can be determined by

$$Q_t = \left(\frac{1}{Q_{cond}} + \frac{1}{Q_{diel}} + \frac{1}{Q_{rad}} \right)^{-1} , \tag{4.2}$$

where Q_{cond} is the Q factor due solely to the current loss in the metal cavity walls; Q_{diel} is associated with the power dissipation in the dielectric filling; and Q_{rad} is the effect of energy radiation through the EBG posts.

An EBG resonant cavity model, as shown in Figure 4.23 is simulated using

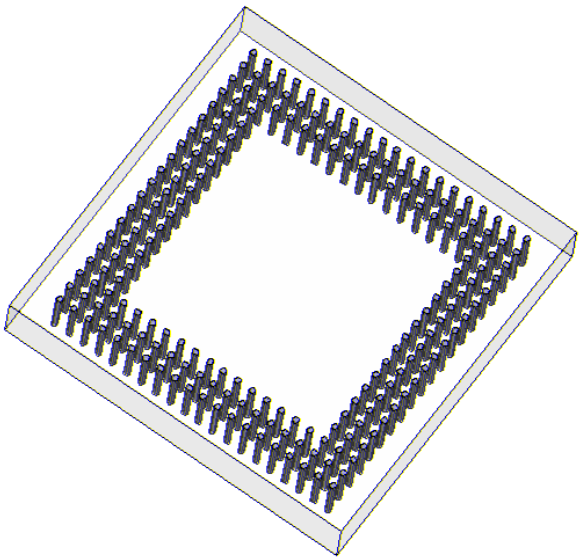

Figure 4.23 EBG resonant cavity model.

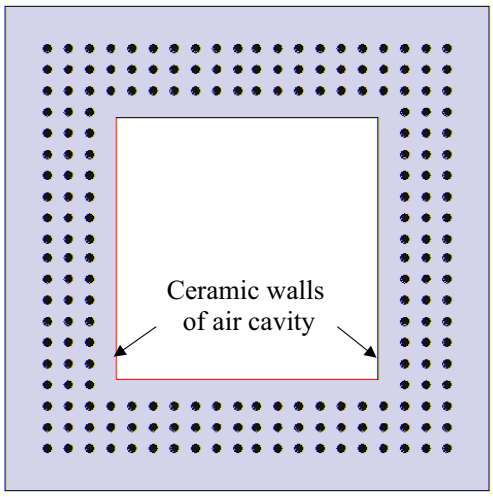

Figure 4.24 LTCC resonant cavity model.

HFSS to determine the effect of radiation loss on resonator Q. No dielectric material is filled in the cavity, although it is not realistic for practical cavity implementation. Therefore, only the conductor and radiation loss contributes to the total Q factor. In order to minimize the leakage loss, three rows of vias are used as sidewalls. For the same reason, minimum size of via posts (via diameter = 130 μm) and spacing (via pitch = 390 μm) [16] allowed by LTCC design rules are used. The dimension of the cavity is adjusted to resonate at 37 GHz. The simulated Q at different cavity heights is given in Figure 4.25. A practical cavity model that could be realized using LTCC technique is also simulated, as shown in Figure 4.24. For LTCC resonator, the overall Q factor is mainly limited by the loss in the ceramic material. In order to investigate the highest possible Q that could be obtained by LTCC resonator, an air cavity is put inside the LTCC resonator [15] (see Figure 4.24), which will reduce the dielectric loss dramatically. The Ferro A6-S LTCC material, with $\epsilon_r = 6.2$ and $\tan\delta = 0.0013$, which is one of the lowest loss LTCC materials, is assumed in the model. The simulated results are also presented in Figure 4.25. To compare with the traditional metallic wall cavity, an HFSS cavity model constructed of fully conducting metals is simulated, and the Q obtained corresponding to the cavity is plotted in Figure 4.25. The metal (gold in this case) surface of all the three cavity models is assumed to be perfectly smooth, with conductivity of 4.1×10^7 S/m.

Comparing the Q values resulting from different cavity models in Figure 4.25, Q_u of the EBG cavity is lower than that of the solid metallic wall cavity at all cavity heights, due to the existence of the radiation loss through the via posts. Also, the radiation loss becomes more important as the cavity height increases. For example, the Q decreases by only 14 (or 3%) at cavity height of 0.2 mm; however, when the cavity height increases to 2 mm, the Q drops by 485 (or 17%) compared with that of the solid wall cavity. For the practical LTCC cavity model with air cavity inside, extra loss dissipated in the LTCC material is introduced. Although the majority of the cavity volume is still filled with air, the effect of

the dielectric loss is significant, which is proved by the rapid decrease of Q as the depth of the cavity becomes higher. Due to the limitation of the computational resource, the LTCC cavity model (see Figure 4.24) is simulated only up to 1.4 mm cavity height.

Also the Q values from the LIGA model considering surface roughness and solid metallic wall cavity at 37 GHz are found to be very close, by comparing Figure 4.21 and Figure 4.25. For example, at a cavity height of 2 mm, the unloaded Q of the solid metallic wall cavity is 2883, while unloaded Q of LIGA cavity is 2858-2868 (see Table 4.4), which is only 0.9% lower than that of solid metallic wall cavity.

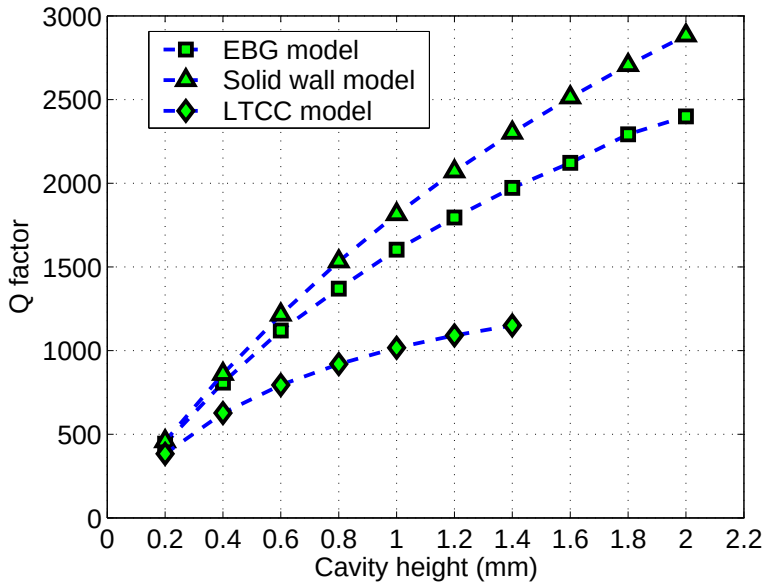

Figure 4.25 Comparison of Q_u derived from 37 GHz cavity models with sidewalls constructed by solid metal and via holes at different cavity height.

4.6 Summary

The properties of the rectangular resonant cavity, including both hollow cavity and dielectric filled cavity, is investigated in this Chapter. Based on these results, a completed one-port resonator suitable for LIGA fabrication is proposed and simulated using HFSS.

To explore the advantages of the LIGA resonator, cavity models representing available fabrication techniques, such as silicon machining and LTCC technologies, are simulated. In comparison to the silicon-based technique, the LIGA process allows the fabrication of very deep cavities with highly vertical sidewalls having optical quality roughness, suggesting that Q performance approaching the perfect smooth cavity is potentially feasible. Also, the simulated LIGA Q_u is found quite promising compared to the simulated silicon structures assuming wafer-stacking techniques. The potential advantages of smooth LIGA resonators are more dramatic at higher frequencies with reduced skin depth. LTCC resonators are realized by replacing solid metal sidewalls with rows of via holes, which results in extra radiation loss through the posts. In order to constrain the fields with the resonator and produce a negligible leakage loss, multiple rows of vias are usually needed. Therefore, the overall structure of the LTCC resonator is larger than an equivalent metallic cavity with solid walls. Although simulation results show that the radiation loss of the LTCC resonator could be minimized by employing multiple layers of vias, the dielectric loss is the major limitation in Q possibly obtained by this technology, even for the extreme case that an air cavity is put inside the LTCC resonator. Simulations also show that the potential advantages of smooth LIGA resonators over silicon and LTCC structures are more dramatic with increasing cavity height.

Chapter 5

RESONATOR FABRICATION AND MEASUREMENT

5.1 Cavity Fabrication

The five-sided cavity structures are fabricated using the LIGA process at the Institute for Microstructure Technology (IMT), Forschungszentrum Karlsruhe in Germany. The first step in the fabrication procedure is to create a layout for the X-ray mask, which contains the information to be transferred into a resist. A picture of the overall mask layout for this application is shown in Figure 5.1. The dimension of the mask are 20 mm $\times$ 60 mm, which is the size of the standard masks used at IMT, and is indicated by the outer rectangular shown in Figure 5.1. The resonant cavities accounts for approximately 60 % of the total mask area. The rest of the mask region is assigned to another user.

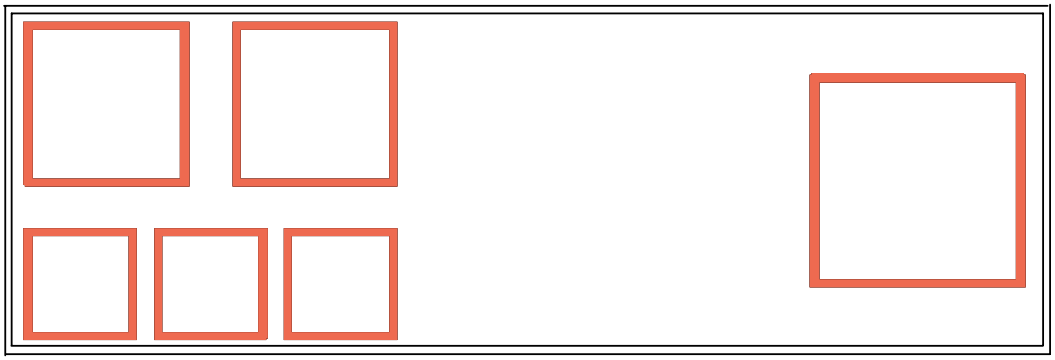

Figure 5.1 Layout for the X-ray mask.

Within the confine of the allocated mask area, six resonant cavities with three

different geometries are included in the layout. The cavities are designed to resonate at frequencies of 18, 24, and 37 GHz. The layout for the 18 GHz design (biggest cavity) is on the right half of the mask. The 24 GHz designs (two identical middle sized cavities) are on the upper left of the mask. The 37 GHz designs (three identical small sized cavities) reside on the bottom left of the mask.

The X-ray mask consists of a thin layer of membrane and an absorber pattered onto the membrane. The membrane is made of low atomic number (Z) materials with a low X-ray absorption coefficient, whose thickness must be carefully chosen in order to be at least 80% transparent to hard X-rays with short wavelength between 0.2 nm and 0.6 nm. Titanium (Ti) and beryllium (Be) are the most commonly used membrane materials for LIGA application because of their radiation transparency [51]. For titanium, the membrane thickness is limited to several micrometres in order to get adequate transparency to X-ray exposure. Whereas, with beryllium, a thicker film of several hundred micrometres can achieve the same results, which makes processing and handing much easier. In addition, the distortions of a beryllium membrane due to the absorber stress is much smaller. The absorber must be made up of a material with high Z, which absorbs X-rays and constitutes the opaque regions of the mask. Gold is the most commonly used material for the absorber, but other metals, such as tungsten and tantalum, are also used. As opposed to the thin membrane, the gold absorber must be at least 10 μm thick to achieve appropriate absorption of X-ray radiation and good contrast.

In order to avoid cracking at the corners of the PMMA structures during the X-ray exposure, the sharp inner edges of the cavities in the layout are rounded by 5 μm. The X-ray mask is fabricated at IMT with a 2.7-μm-thick titanium membrane and a 20-μm-thick gold absorber.

The cavity fabrication steps are described in Figure 5.2. For simplicity, only cavities on the left portion of the layout (see Figure 5.1) are demonstrated. With the X-ray mask fabricated, the LIGA process starts with gluing a resist (PMMA)

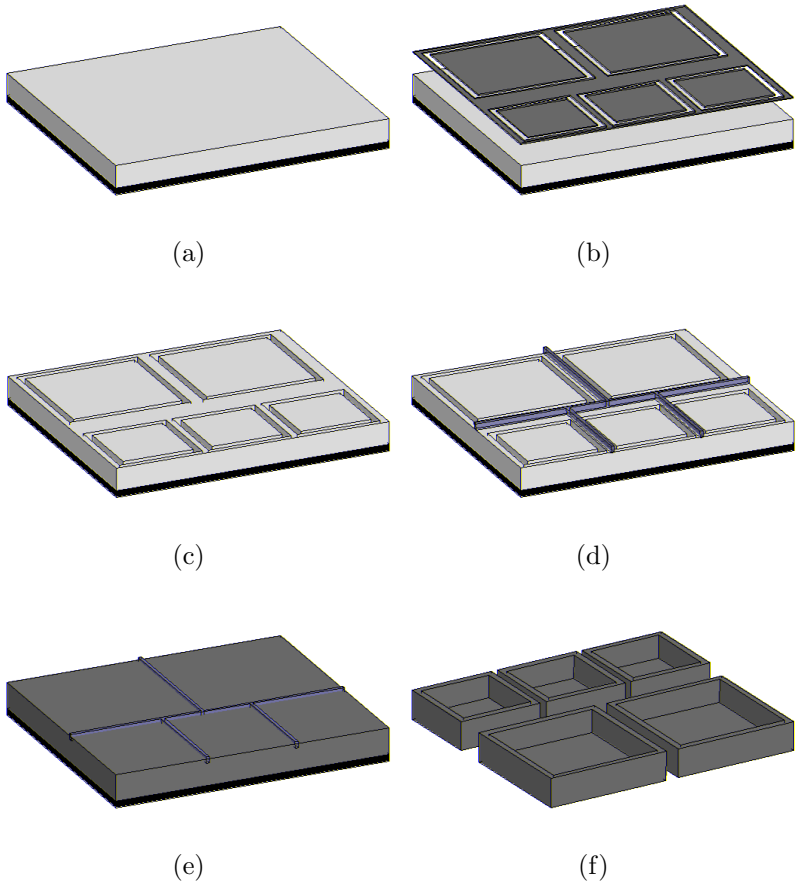

Figure 5.2 LIGA fabrication steps for the resonant cavities.

sheet onto the substrate, as shown in Figure 5.2(a). A variety of materials, such as silicon, alumina, and quartz, can be used as substrate in the LIGA process. Generally, prior to applying the resist, a thin film of conductor is required to be coated on the insulating substrate as a plating base for further electroplating. But this step is not a necessary in this cavity fabrication process. It is replaced by another method, which will be explained later. For this application, a standard 525-μm-thick silicon wafer is used as a sacrificial substrate, and an 1800-μm-thick PMMA sheet is glued on the substrate using a liquid PMMA-based glue.

The next step is to expose the thick PMMA resist to hard X-ray radiation through the mask, as shown in Figure 5.2(b). After this step, the patterns on the X-ray mask are exactly transferred to the PMMA resist. PMMA is a positive resist. X-ray exposure breaks the molecule chains of the resist in the exposed region, which can be easily dissolved using a suitable developer, as shown in 5.2(c). The high accuracy, vertical and smooth sidewalls are the result of the short wavelength of the X-ray radiation, as well as no back scattering and forward scattering effects. In this case, 1.8-mm-thick PMMA on a silicon substrate was exposed to hard X-ray radiation at storage ring ANKA (Litho 3) operated at 2.5-GeV synchrotron energy. The power of the white beam was reduced by carbon (652μm) and aluminum (282 μm) preabsorbers to diminish the thermal distortions of the 2.7-μm-thick titanium mask membrane. 500-μm-thick intermediate absorbers (polyimide) were applied between the mask and resist to reduce the attack of the resist surface by fluorescence radiation generated in the titanium mask membrane.

The irradiated sample was dip-developed in GG developers at room temperature. The PMMA regions exposed to the X-ray radiation are dissolved, and PMMA cavity structures are formed as shown in Figure 5.2(c). At least four layers of green tape are glued on top of the PMMA, as shown in Figure 5.2(d), to assist in later separation of the cavity devices after metallization.

A scanning electron microscope (SEM) image of the 1800 μm tall PMMA

structure after X-ray exposure and immersion development is shown in Figure 5.3. Excellent sidewall verticality is obtained with the PMMA structure, with only slight shrinkage at the top surface of 8.5 ± 2.5 μm in either lateral dimensions. This corresponds to sidewalls with verticality between 89.82^0 and 89.9^0. Figure 5.4 demonstrates the sidewall surface quality of the PMMA structure, measured to be on the order of 26 ± 12 nm for structures of similar height using the deep XRL process at IMT [46].

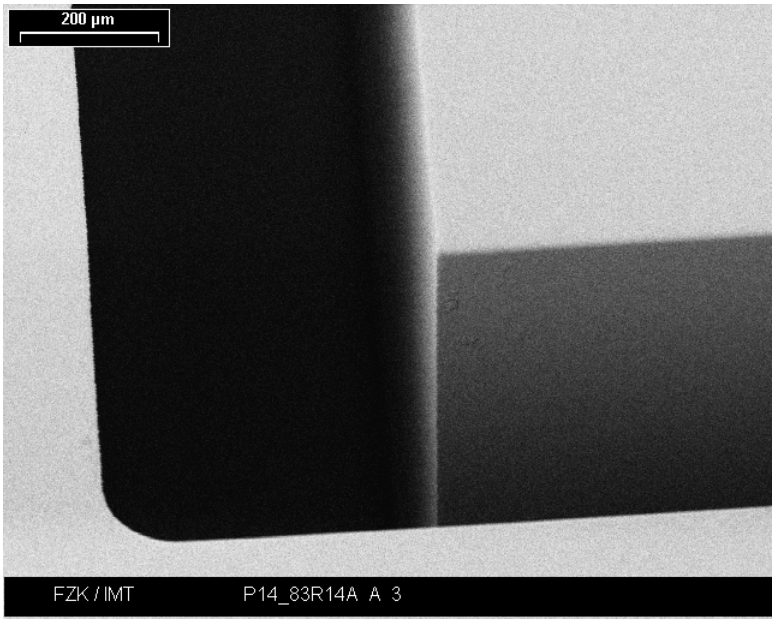

Figure 5.3 SEM micrograph of the PMMA cavity structure made with XRL.

The developed PMMA structure is then used as a template for metal electroforming, and to define the metallic cavity inside wall structure. Gold is chosen as the metal to be deposited in contact with the PMMA resist and form the internal walls of the cavities due to its high conductivity. A thin film of gold (approximately 900 nm) was first sputtered on the PMMA surface as a plating base, and then was thickened to in excess of several skin depths (in this case, approximately 5 μm thick) by gold electroplating, ensuring that the electrical loss characteristics of the cavity sidewall were governed by the gold layer, and not the subsequent

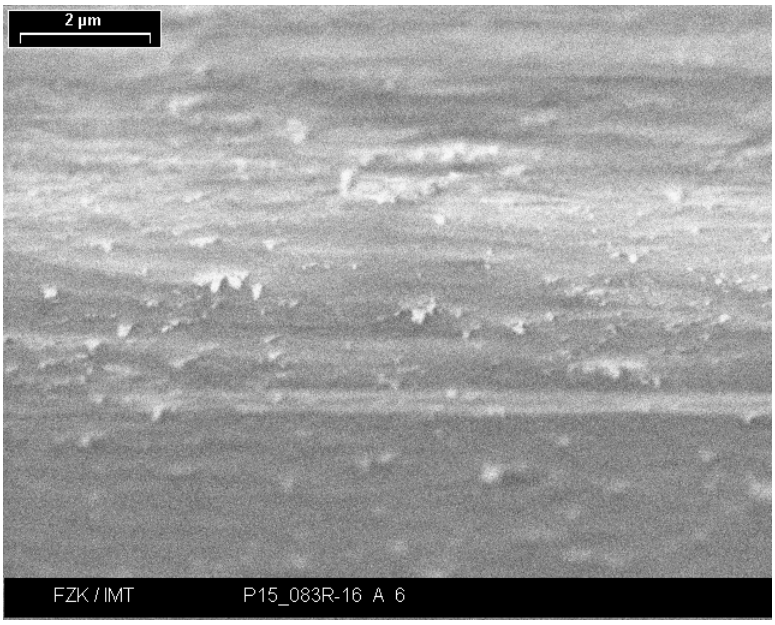

Figure 5.4 SEM micrograph of the side surface of PMMA cavity structure made with XRL.

nickel structural layer. Since almost all the electromagnetic fields are confined within the 3-4 skin depth of the inside cavity walls, the 5 μm gold layer is thick enough to provide good electrical performance. Then nickel (approximately 500 μm), the most widely used metal in electroplating LIGA due to its low internal stress in the tall metal structures, is electroplated on top of the gold until the gaps are fully filled to provide mechanical strength for the final metal cavities. As seen in Figure 5.2(e), after the electroplating process, part of the green tape is buried in the metal.

Then the silicon substrate is etched off in potassium hydroxide (KOH) solvent. Finally, the remaining resist is removed by flood exposure and development. The sequence of flood exposure and development is done three times, in order keep the additional stress as low as possible. The metal cavity structures are separated after the stripping, as shown in 5.2(f), in which the structure is flipped over to obtain a better view. With this process, the cavity sidewall surface quality is governed by the roughness of the sidewalls of the PMMA template.

A SEM picture of the inside corner of the final metallized cavity structure is shown in Figure 5.5. A SEM picture of the bottom surface of the metal cavity is shown in Figure 5.6. Excellent surface quality is evident from Figure 5.5 and Figure 5.6, which suggests the potential of the LIGA process for fabricating cavities with high Q and low loss. The few slight scratches on the bottom surface (Figure 5.6, corresponding to the top PMMA surface) are not a result of X-ray exposure, but due to roughness of the PMMA sheet. This could possibly be improved with better surface polishing of the PMMA sheet.

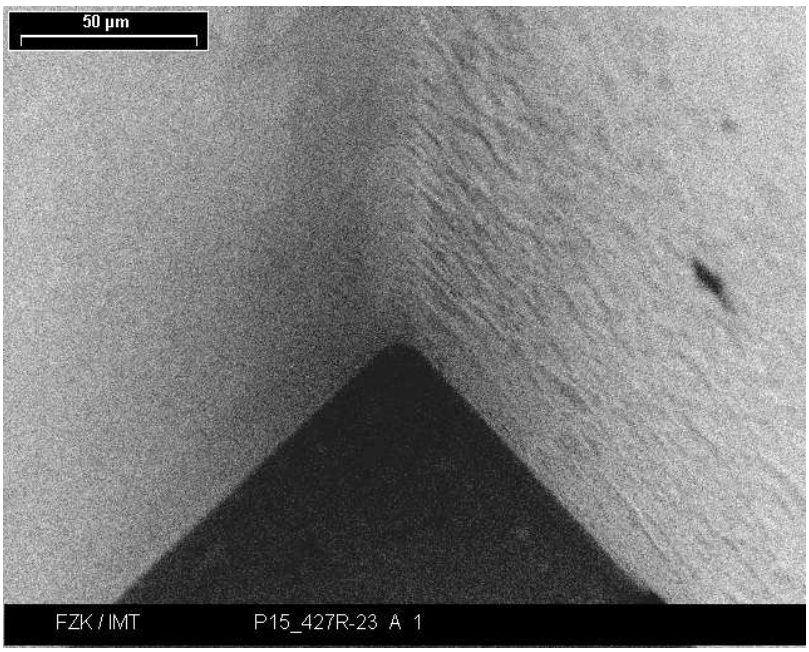

Figure 5.5 SEM micrograph of the inside corner of the gold and nickel metallized cavity made using deep XRL PMMA template.

5.2 Measurement Results and Discussion

5.2.1 24 GHz Resonator

To facilitate the testing of the 24 GHz five-sided metallic cavity, an available RT/Duriod^{TM} 6010 soft substrate was used to fabricate an open circuit microstrip feed line and ground plane coupling slot, and forms the sixth side of the resonator. The thickness of the substrate is 0.635 mm, which results in a cutoff frequency

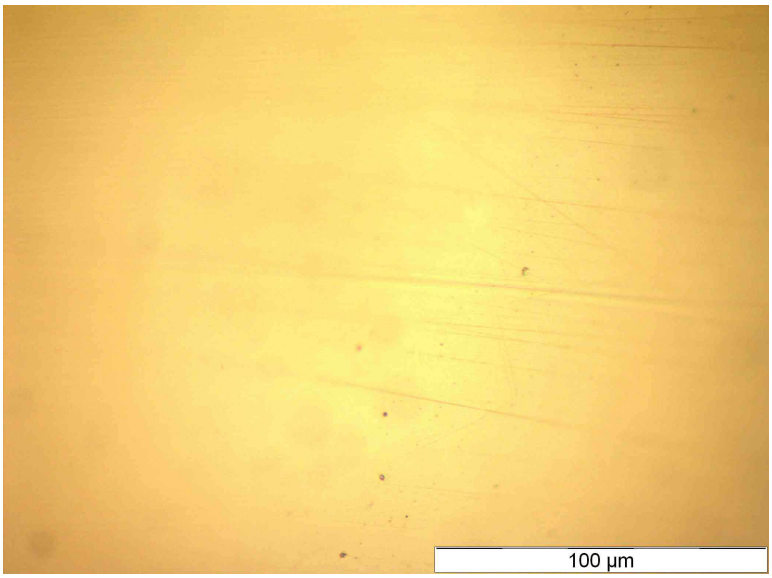

Figure 5.6 SEM micrograph of gold and nickel metallized cavity made using deep XRL PMMA template.

of approximately 31.5 GHz for a 50 Ω microstrip line. The dielectric loss of the substrate is relatively high, with loss tangent of 0.0023 at 10 GHz. The substrate is cladded with 1/2 oz. (17 μm) rolled copper, which has approximate 300 nm surface roughness. The rectangular coupling slot of 1.3 mm in length and 0.5 mm in width is milled into the copper ground plane.

The top wafer and the cavity were connected together through clamping, and the performance of the resonator was measured using an Agilent 8722ES vector network analyzer (VNA) and a test jig with a coaxial APC 3.5 connector, constructed to hold the assembly. A full SOL (short/open/load) 1-port calibration using a coaxial calibrated short, open, load, and sliding load was performed around 24 GHz. The connector and microstrip feed line loss are not accounted for in the calibration.

The nominal position between the cavity and the top substrate is found by moving the cavity around slightly until a strong resonance occurs at around 24 GHz. The measured S_{11} response of the resonator around 24 GHz is plotted on the Cartesian plane and also the Smith chart in Figures 5.7 and 5.8, respectively. Fig-

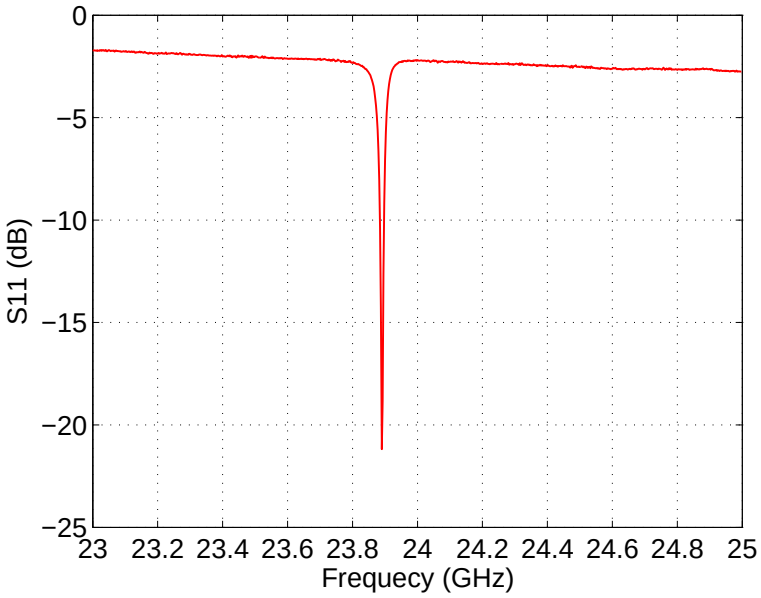

Figure 5.7 S_{11} magnitude response of the 24 GHz LIGA cavity resonator showing the resonant peak at 23.89 GHz.

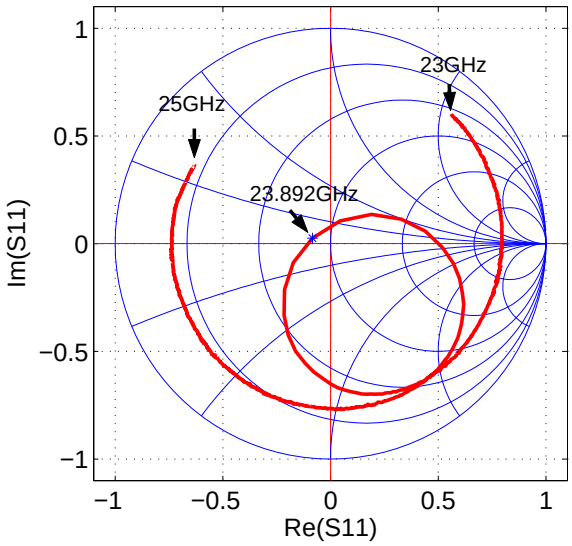

Figure 5.8 S_{11} response of the 24 GHz LIGA cavity resonator on the Smith chart used to calculated Q_u.

ure 5.7 shows a very strong resonance at 23.892 GHz. Unloaded Q was extracted from the loaded circuit using a reflection type measurement as in Section 3.2, based on the measured value of S_{11} shown in Figure 5.8. As described in Section 3.2, the input reflection coefficient in the vicinity of the resonant frequency forms a circle on the Smith chart. At the frequencies far off the resonance, the impedance representing the resonant cavity itself disappears, and the reflection coefficient becomes that of the coupling system, which is the top substrate patterned with the microstrip line and the slot on the ground plane. On the Smith chart, the variation of the impedance of the top substrate with the frequency is demonstrated by the curve outside the Q circle. A summary of modelled and measured data is given in Table 5.1.

Table 5.1 Summary of modelled and measured results for the 24 GHz LIGA cavity resonator

Resonator	f_{res} (GHz)	Q_u	Q_l
HFSS	23.980	2274.3±53.4	1015.8±15.3
Measured	23.892	1742.3±56.4	908.0±23.4

The APC 3.5 connector inserted between the feed line of the resonator and the test jig is not included in the HFSS model, which also leads to the difference in the resonant frequency and Q factor between simulated and measured results. The connector loss is measured separately, and found to be 1.0 dB around 24 GHz. When the 1.0 dB of the uncalibrated loss in S_{11} is included in the calculation, the Q_u increases to a value of 1868.4 ± 66.7. The combined loss of connector and microstrip feed line is measured to be 2.0 dB. Subtracting this from the measured S_{11} gives a Q_u of 2122.2 ± 85.0.

The differences between the simulated and measured results could also be explained by the inaccurate hand alignment between the substrate and the five-sided cavity. The sensitivity of the resonator parameters to the alignment is simulated using HFSS. The position of the cavity is varied from its nominal position, where

the center of the coupling slot is located at 1/4 of the length of the cavity as shown in Figure 4.6. The HFSS model is simulated with cavity position deviation in both the x direction (direction along slot length) and the z direction (direction along the slot width). The simulated results for cavity position deviation in the x direction are plotted in Figure 5.9, in which zero in the x axis indicates the nominal position of the cavity, positive and negative numbers indicate that the cavity is moving along the length of the slot, but towards the opposite directions. In Figure 5.9, the simulated data points are curve fitted to a second order polynomial. As seen from Figure 5.9(a), the cavity position deviation in the x direction has little effect on the resonant frequency of the resonator. The unloaded Q tends to increase slightly with increasing the cavity position deviation, and is symmetric about the nominal cavity position (See Figure 5.9(b)). The coupling coefficient k decreases slightly with increasing the cavity position deviation, and is also symmetric about the nominal cavity position (See Figure 5.9(c)).

The simulated results for cavity position deviation in the z direction are plotted in Figure 5.10, in which the negative numbers indicate the cavity is moving along the width of the slot towards the port, and the positive numbers mean that the cavity is moving away from the input port. The resonant frequency variation with the cavity position deviation is demonstrated in Figure 5.10(a), where the frequency increases when the cavity moves away from the input port. The unloaded Q increases (see Figure 5.10(b)), while the coupling coefficient k decreases (see Figure 5.10(c)) when the coupling slot is closer to the center of the cavity (the cavity moves towards the port).

Comparing Figure 5.9 and Figure 5.10, the cavity position deviation in the z direction has more effect on the resonant frequency, unloaded Q, and coupling coefficient k than the cavity position deviation in the x direction, especially for the coupling coefficient k, which varies from +25% to -29%. However, it can be seen from Figure 5.9 and Figure 5.10, the cavity alignment has limited effect on Q_u. Compared with the results obtained at nominal cavity position, maximum

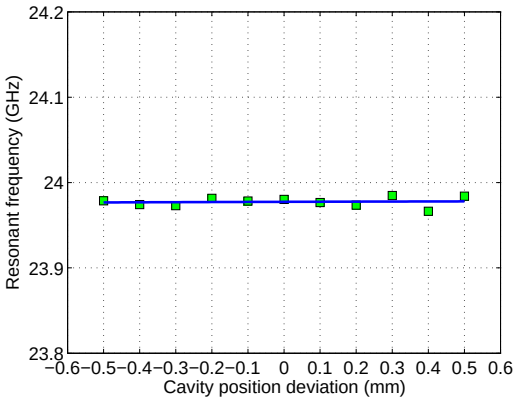

(a) Resonant frequency versus cavity position deviation.

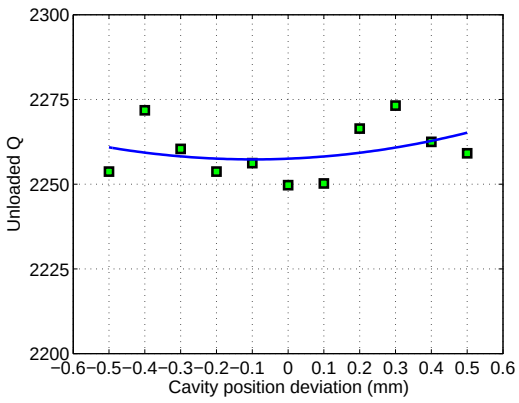

(b) Unloaded Q versus cavity position deviation.

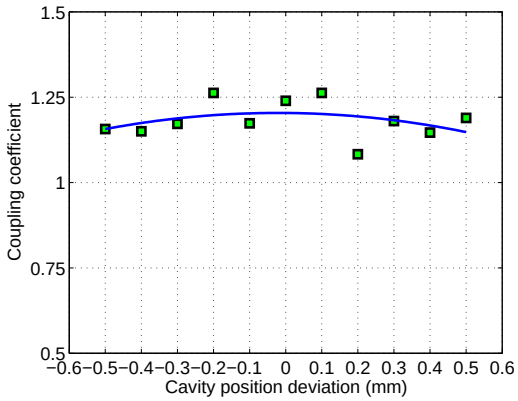

(c) Coupling coefficient versus cavity position deviation.

Figure 5.9 Sensitivity of 24 GHz resonator parameters to the cavity position deviation in the x direction.

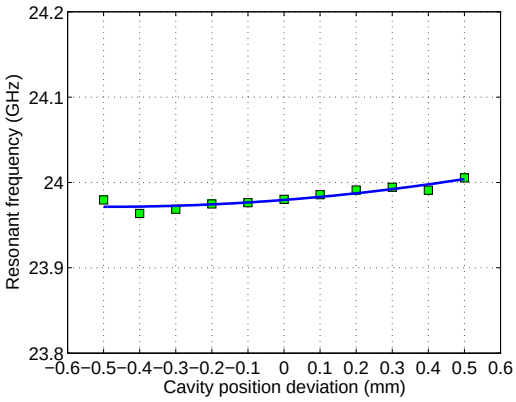

(a) Resonant frequency versus cavity position deviation.

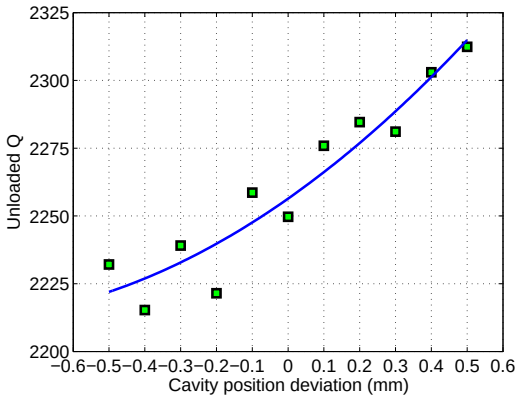

(b) Unloaded Q versus cavity position deviation.

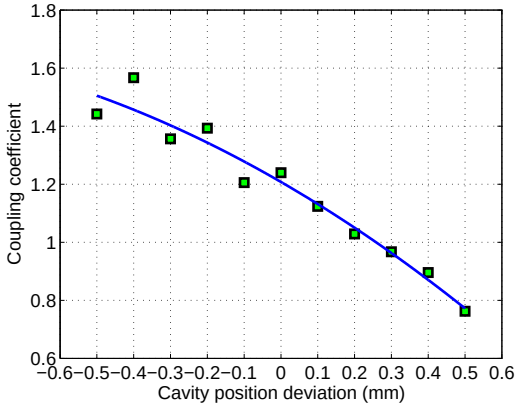

(c) Coupling coefficient versus cavity position deviation.

Figure 5.10 Sensitivity of 24 GHz resonator parameters to the cavity position deviation in the z direction.

Q_u degradation is about 30 or 1.33%.

As described before, the degree of field coupled into the cavity is controlled by the slot position. When the cavity moves, the relative position between the coupling slot and the cavity varies accordingly, which changes the coupling coefficient of the resonator, as shown in Figures 5.9(c)and 5.10(c). The magnitude of electric and magnetic field intensity at the center of the slot as a function of the cavity position deviation in the x direction and the z direction is plotted in Figure 5.11 and Figure 5.12, respectively. The amplitude of the field intensity is normalized to the field intensity where the cavity is at its nominal position. When the cavity position moves along the slot length, the electric and magnetic field intensity (see Figure 5.11(a) and Figure 5.11(b)) at the center of the slot tends to vary in the same direction. When the cavity position moves along the slot width, the electric field intensity (see Figure 5.12(a)) increases with the cavity position deviation, while the magnetic field intensity (see Figure 5.12(b)) decreases with the cavity position deviation. The electric and magnetic field intensity at the center of the slot tends to vary in the opposite direction. However, in both cases, the changing of the coupling coefficient (see Figure 5.9(c) and Figure 5.10(c)) always coincides with the variation of the magnetic field intensity, which denotes that magnetic coupling is stronger than electric coupling and thus is the dominant coupling mechanism.

The simulated Q_u given in Table 5.1 is obtained based on 1.8 mm cavity height. Although the height of the PMMA sheet is expected to be uniform, an accurate measurement shows that the thickness of the PMMA sheet ranges from 1.765 mm to 1.800 mm, measured at nine different locations of PMMA. Unfortunately, it is difficult to determine the exact original positions of the cavities on the wafer, after the metal cavities were separated during the last fabrication step. Simulations are run for HFSS models with reduced cavity height. The results are shown in Table 5.2. For the lowest possible cavity height measured to be 1.765 mm, the resonant frequency decreases by 4 MHz, and the unloaded Q drops by 2.63%,

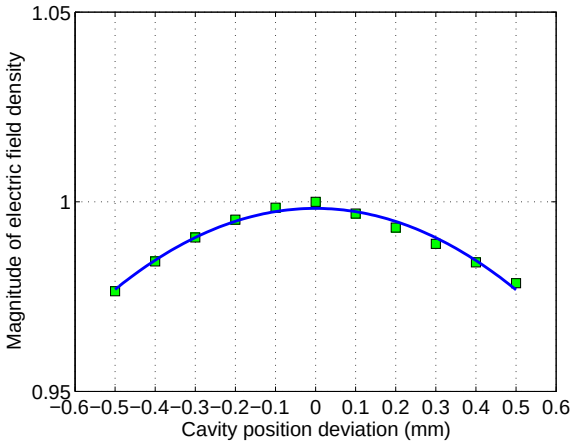

(a) Magnitude of electric field intensity versus cavity position deviation.

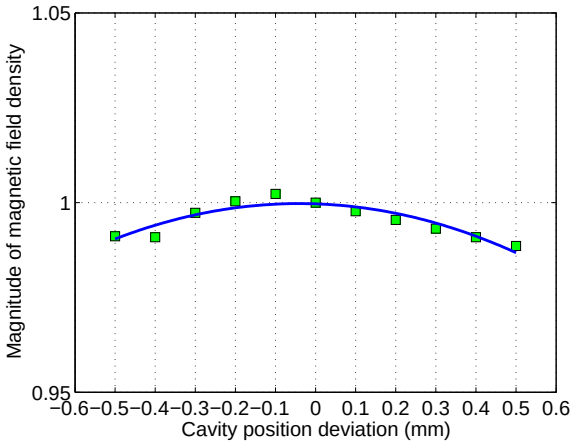

(b) Magnitude of magnetic field intensity versus cavity position deviation.

Figure 5.11 Magnitude of electric and magnetic field intensity at the center of the slot as a function of the cavity position deviation in the x direction for a 24 GHz resonant cavity.

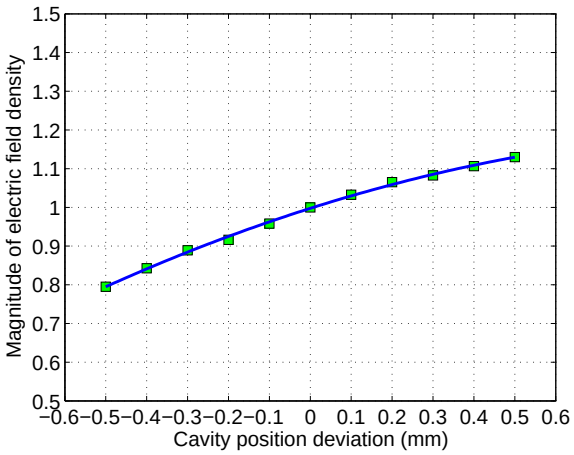

(a) Magnitude of electric field intensity versus cavity position deviation.

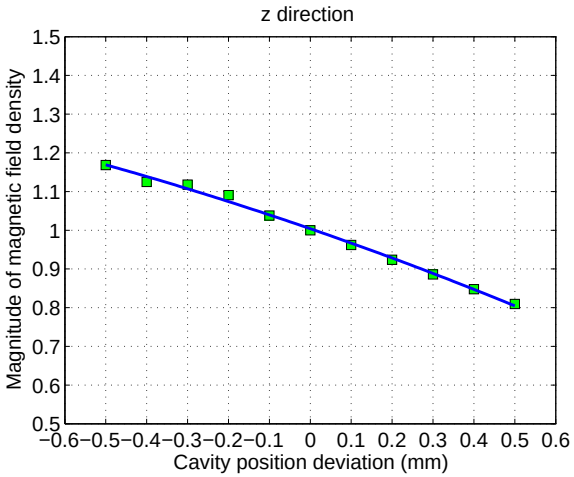

(b) Magnitude of magnetic field intensity versus cavity position deviation.

Figure 5.12 Magnitude of electric and magnetic field intensity at the center of the slot as a function of the cavity position deviation in the z direction for a 24 GHz resonant cavity.

compared with the HFSS simulation result based on the 1.8-mm cavity shown in Table 5.1. By accounting for the effect of cavity height reduction, the tested resonator results in Table 5.1 are in closer agreement with the simulation results.

Table 5.2 Simulation results for the 24 GHz LIGA cavity resonator with reduced cavity height

Cavity height	f_{res} (GHz)	Q_u
1.765 mm	23.976	2223.3 ±46.7
1.800 mm	23.980	2274.3 ±53.4

Another possible reason for the discrepancies between measured and simulated results is that the top substrate and the cavity is connected through clamping, which could possibly leave air gaps between the interface and result in Q_u decreasing. Although no such experiment has been done, it is reported that Q_u could increase by at least one hundred after the substrate and the cavity are completely bonded through soldering [13], and also the resonant frequency could shift down by about 50 MHz.

5.2.2 37 GHz Resonator

As evaluated using Equation 4.1, the cutoff frequency for a 50 Ω microstrip line on a RT/Duroid^{TM} 6010 soft substrate is 31.5 GHz. Although for 37 GHz applications, which is above the cutoff frequency, the Quasi-TEM mode transmission is not maintained, and the longitudinal field components could be comparable with the transverse field components, simulation results show that the fields in the feed microstrip line are likely big enough to excite the 37 GHz metallic cavity.

The simulated S_{11} response of the 37 GHz resonator is plotted on the Cartesian plane and also the Smith chart in Figure 5.13 and Figure 5.14, respectively. Similar to the HFSS model for the 24 GHz resonator, the surface roughness (30 nm on the interior walls of the five sided cavity and 300 nm on the ground plane of the soft substrate) is accounted for by corresponding reduction in the metal conductivity. Also, the cavity top shrinkage of 10 μm in lateral dimensions are incorporated in

the model, as measured from the PMMA cavity structure after X-ray exposure and development. The coupling slot opened in the ground plane of the soft substrate has the dimension of 1.1 mm $\times$ 0.5 mm to give a result shown in Figures 5.13 and 5.14. The HFSS model resonates at 36.955 GHz, as indicated in Figure 5.13. The unloaded Q is extracted to be 2124.8 $\pm$ 65 based on the simulated S_{11} in Figure 5.14.

The same test procedure as described in Section 5.2.1 is applied to the 37 GHz resonator. The measured S_{11} response is plotted in Figures 5.15 and 5.16, respectively. According to Figure 5.15, the resonant frequency is found to be 36.960 GHz, which is very close to the simulated results of 36.955 GHz. However, the unloaded Q, which is extracted to be 308.7 $\pm$ 19.6, is much lower than the simulated value of 2124.8 $\pm$ 65. In addition to the reasons discussed in Section 5.2.1, which cause the performance degradation of the 24 GHz resonator, there is another possible explanation for the 37 GHz resonator case. According to Equation 4.1, a 50 Ω microstrip line on the RT/Duriod^{TM} 6010 substrate (with thickness of 0.635 mm) results in a cutoff frequency of 31.5 GHz. Therefore, at the frequency around 37 GHz, the fields in the substrate cannot be treated as a Quasi-TEM mode. As a result, the microstrip-slot aperture coupling analysis described in Section 2.2.3 may not apply to the 37 GHz resonator case. This could be the primary reason that the measured Q is significantly lower than expected. Another possible explanation might be attributed to possible fabrication irregularities, for instance, the gold layer at the internal cavity walls is not as thick as expected (several skin depths), and is deposited unevenly on top of the nickel structure during the electroplating process. Unfortunately, the thickness of the gold layer could not be measured without damaging the cavity. It is expected that much higher Q could be achieved with a proper top substrate and an improved test setup.

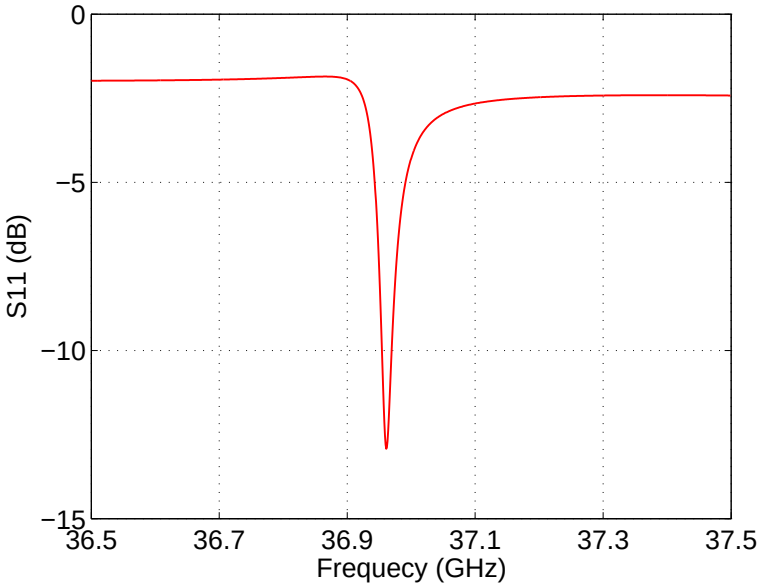

Figure 5.13 Simulated S_{11} magnitude response of the 37 GHz LIGA cavity resonator.

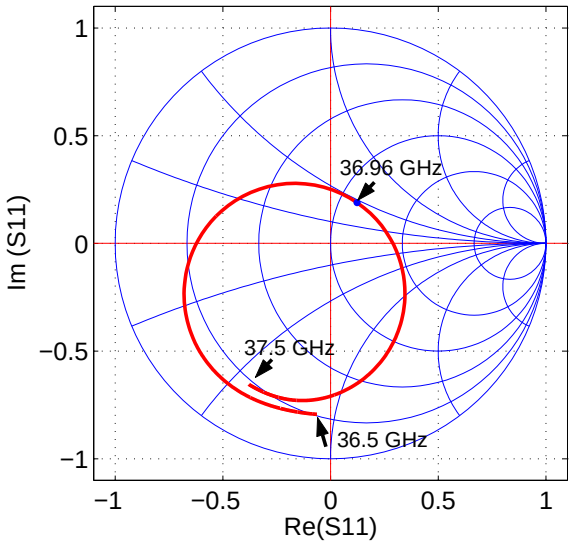

Figure 5.14 Simulated S_{11} response of the 37 GHz LIGA cavity resonator on the Smith chart.

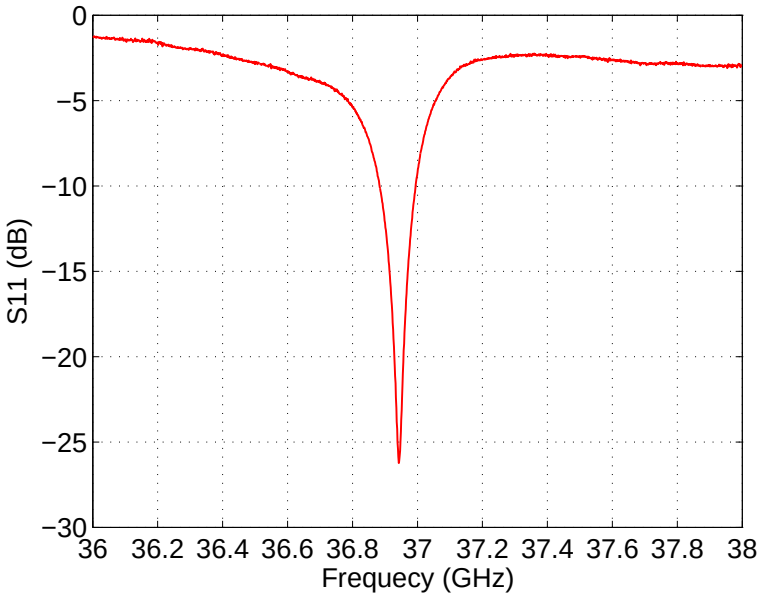

Figure 5.15 Measured S_{11} magnitude response of the 37 GHz LIGA cavity resonator.

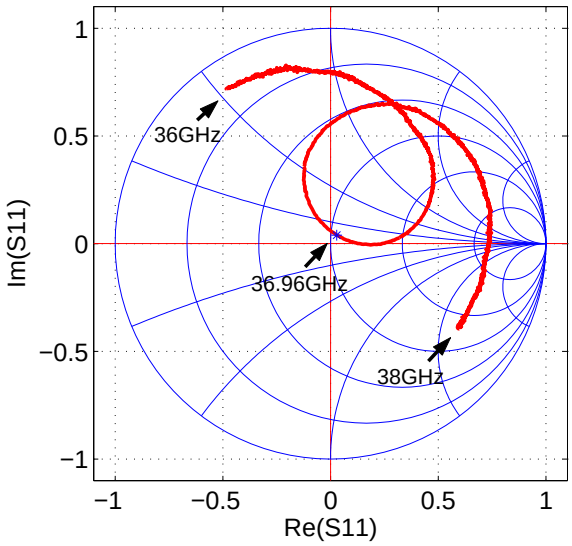

Figure 5.16 Measured S_{11} response of the 37 GHz LIGA cavity resonator on the Smith chart.

5.3 Summary

In this Chapter, the steps taken in the fabrication of resonant cavities using the LIGA technique are demonstrated. An implementation of a 1800 μm deep, 24 GHz microwave cavity is presented. Despite the rather crude test assembly for the sixth side made by clamping, the measured resonator has a high unloaded Q of 2122.2$\pm$85, indicating that LIGA cavities are especially promising for high performance, low-cost applications. Also, the possible reasons for the discrepancy between the HFSS simulated and measured results are discussed.

A 37 GHz resonator is also simulated and tested. Although the resonant frequency is as expected, the measured Q is much lower than the simulated Q at the resonance frequency around 37 GHz. The exact cause for this decrease is not well understood, but it is likely a combination of inappropriate top substrate and inaccurate test setup, which is suggested in Chapter 7 as a subject for future research.

Chapter 6

POST FILTER

6.1 General Filter Design

As an extension of the cavity resonator concept, the capability of realizing high performance filters using the LIGA process is investigated in this Chapter. A filter is a two-port circuit whose frequency response provides transmission at desired frequencies and attenuation at other frequencies. An ideal filter should perform this function without adding or generating new frequency components, and would also have a linear phase response. The transmission loss should be zero in the passband, and the transmission attenuation should be infinite in the stopband. Network synthesis is a popular filter design technique. It usually starts with finding the transfer function that satisfies the requirements of an application. From the function, the input impedance and the complex zeros and poles are found by various algebraic procedures, such as partial-fraction expansion. The element values of the circuit are then derived from the expansion of the input impedance. The lumped element filter constructed from these element values gives the desired frequency response. Network synthesis begins with low-pass filter prototypes normalized in terms of frequency and impedance. Then appropriate transformations are applied to convert the low-pass design to the desired filter type with the required operating frequency and impedance level.

The Chebyshev characteristic is a commonly used low-pass filter prototype and is used to illustrate the filter realization in this section. This filter class employs the Chebyshev polynomial and provides an equal ripple variation in the passband,

and decreases outside the passband. The transfer function of the Chebyshev low-pass prototype is defined as

$$|H(j\omega)|^2 = \frac{1}{1+\varepsilon^2 T_n^2(\omega)} \ , \tag{6.1}$$

where ε is a measure of the passband ripple and has the value $0 < \varepsilon < 1$; $T_n(\omega)$ is the Chebyshev polynomial of the nth order, which is defined as

$$T_n(\omega) = \begin{cases} \cos(n\cos^{-1}(\omega)) & |\omega| \leq 1 \\ \cosh(n\cosh^{-1}(\omega)) & |\omega| > 1 \end{cases} \ . \tag{6.2}$$

A low-pass filter prototype, which provides the Chebyshev transfer function, can be constructed with the cascade of series inductances and shunt capacitances, as indicated in Figure 6.1. The expressions for the element values g are found by expanding of the Chebyshev polynomial by its recursion formulas. The filter elements associated with the nth order Chebyshev functions can be found in a variety of references. The final results are given by [52]

$$\beta = \ln(\coth\frac{L_{Ar}}{17.37}), \tag{6.3a}$$

$$\gamma = \sinh(\frac{\beta}{2n}), \tag{6.3b}$$

$$a_k = \sin[\frac{(2k-1)\pi}{2n}] \quad k = 1, 2, ...n, \tag{6.3c}$$

$$b_k = \gamma^2 + \sin^2(\frac{k\pi}{n}) \quad k = 1, 2, ...n, \tag{6.3d}$$

$$g_0 = 1, \tag{6.3e}$$

$$g_1 = \frac{2a_1}{\gamma}, \tag{6.3f}$$

$$g_k = \frac{4a_{k-1}a_k}{b_{k-1}g_{k-1}}, \tag{6.3g}$$

$$g_{n+1} = \begin{cases} 1 & n \text{ odd} \\ \coth^2(\beta/4) & n \text{ even} \end{cases} \ , \tag{6.3h}$$

where L_{Ar} is the passband ripple specified by the requirement of the application; n is the order of the filter, which is the number of the reactive elements (resonators) in the filter circuit.

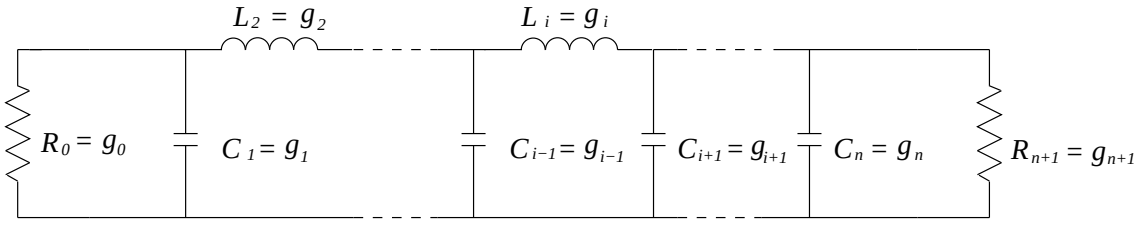

Figure 6.1 Low-pass filter prototype.

In the low-pass filter prototype, the source and load impedances and the cutoff frequency are normalized to unity. This design can be transformed into a bandpass filter by the frequency substitution

$$\omega' = \frac{\omega'_1}{\Delta}\left(\frac{\omega}{\omega_0} - \frac{\omega_0}{\omega}\right), \tag{6.4}$$

$$\Delta = \frac{\omega_2 - \omega_1}{\omega_0}, \tag{6.5}$$

$$\omega_0 = \sqrt{\omega_1 \omega_2}, \tag{6.6}$$

where ω' is the frequency of the low-pass prototype to be replaced; ω'_1 is the ripple band edge of the low-pass prototype, which is normalized to unity; ω_1 and ω_2 are the lower and upper band edge frequencies of the band-pass prototype respectively; Δ is the fractional bandwidth of the bandpass filter; ω_0 is the center frequency of the bandpass response.

The bandpass filter elements can be determined by the frequency transformation using Equation 6.4. Thus, the reactance X in the low-pass filter is transformed as

$$
\begin{aligned}
jX_n &= \frac{j}{\Delta}\left(\frac{\omega}{\omega_0}-\frac{\omega_0}{\omega}\right)L_n \\
&= j\frac{\omega L_n}{\Delta\omega_0}-j\frac{\omega_0 L_n}{\Delta\omega} \\
&= j\omega L_n' - j\frac{1}{\omega C_n'} \ , \qquad (6.7)
\end{aligned}
$$

which is a series LC circuit with element values

$$L_n' = \frac{L_n}{\Delta\omega_0} \ , \qquad (6.8)$$

$$C_n' = \frac{\Delta}{\omega_0 L_n} \ . \qquad (6.9)$$

Using the same process, the susceptance B in the low-pass filter can be transformed as

$$
\begin{aligned}
jB_n &= \frac{j}{\Delta}\left(\frac{\omega}{\omega_0}-\frac{\omega_0}{\omega}\right)C_n \\
&= j\frac{\omega C_n}{\Delta\omega_0}-j\frac{\omega_0 C_n}{\Delta\omega} \\
&= j\omega C_n' - j\frac{1}{\omega L_n'} \ , \qquad (6.10)
\end{aligned}
$$

which represents a parallel LC circuit with element values

$$L_n' = \frac{\Delta}{\omega_0 C_n} \ , \qquad (6.11)$$

$$C_n' = \frac{C_n}{\Delta\omega_0} \ . \qquad (6.12)$$

The corresponding bandpass filter structure transformed from the lumped-element low-pass prototype is shown in Figure 6.2.

Lumped element filters are generally suitable for applications at low frequencies and are difficult to implement for microwave applications. At microwave frequencies, the filter elements are usually realized by using distributed components,

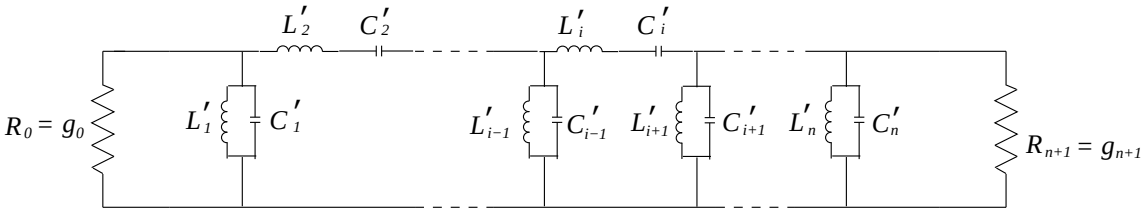

Figure 6.2 Bandpass filter structure.

such as transmission line sections. In addition, it is desirable to use only series or only shunt elements for practical microwave filter implementations. Therefore, it is convenient to modify the low-pass lumped filter prototype by using impedance inverters. Basically, an impedance inverter has the same function as a quarter-wavelength transmission line with characteristic impedance of K but ideally is independent of frequency. Therefore, the impedance inverter can be used to convert elements between series and shunt forms, by transforming a terminating impedance Z_b into an impedance Z_a looking into the inverter as

$$Z_a = \frac{K^2}{Z_b}. \tag{6.13}$$

Because of the property of the impedance inverter, a series inductance with an inverter on one side is equivalent to a shunt capacitance looking into the inverter. Using the impedance inverter, the shunt capacitors in Figure 6.1 can be transformed into series inductors, and the low-pass prototype can be represented using only inductances, as shown in Figure 6.3.

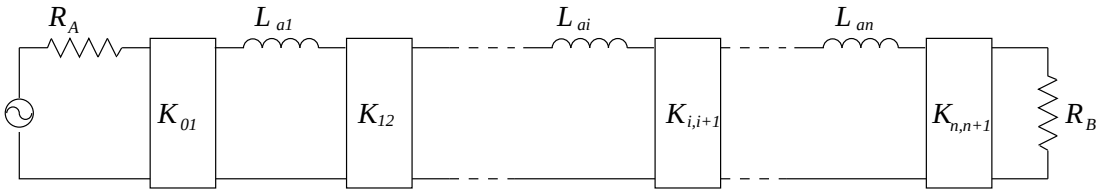

Figure 6.3 Modified low-pass filter prototype using impedance inverters and series inductances.

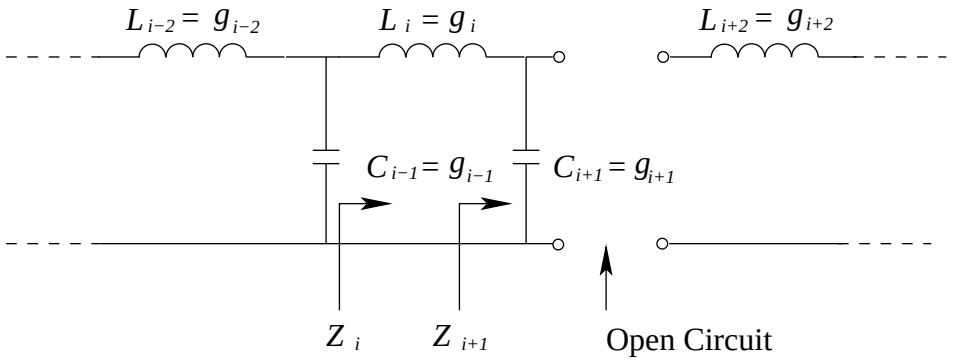

(a) Part of the low-pass prototype circuit with open end.

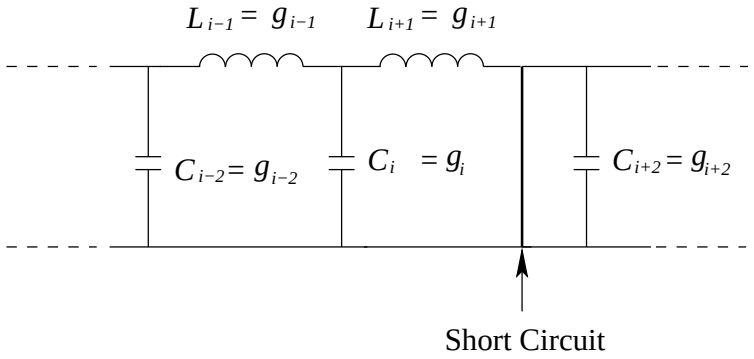

(b) Dual of the low-pass circuit.

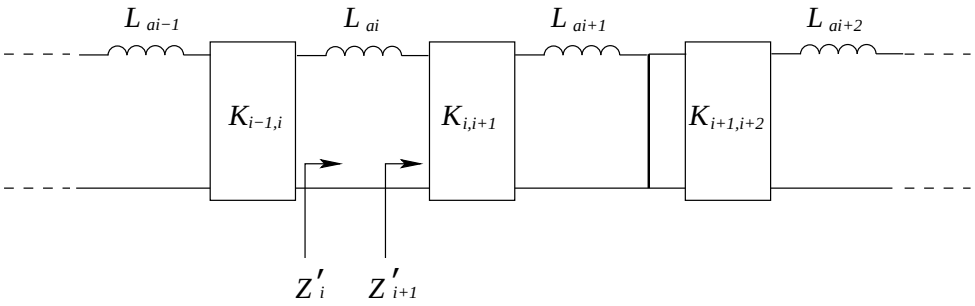

(c) Corresponding K-inverter form of the circuit.

Figure 6.4 Circuits used to derive the formula for internal K.

The value of R_A, R_B, and L_{an} can be chosen arbitrarily, provided that the desired K parameter is derived to give the identical frequency response to that of the original prototype as in Figure 6.1. Open- and short-circuits are introduced in order to simply the equations. The expression for K can be derived with the aid of the circuits shown in Figure 6.4. Figure 6.4(a) is a part of the low-pass prototype circuit (see Figure 6.1), which has an open end after the capacitor C_{i+1}. The dual circuit of Figure 6.4(a) is shown in Figure 6.4(b), in which the shunt capacitors become the series inductors, the series inductors become the shunt inductors, and the open circuit becomes a short circuit. The corresponding circuit representing by series inductors and K inverters is shown in Figure 6.4(c).

In the circuit shown in Figure 6.4(a), the impedance looking into inductor L_i is

$$Z_i = j\omega L_i + \frac{1}{j\omega C_{i+1}}. \tag{6.14}$$

In the circuit shown in Figure 6.4(c), the impedance looking into inductor L_{ai} is

$$Z_i' = j\omega L_{ai} + \frac{K_{i,i+1}^2}{j\omega L_{ai+1}}. \tag{6.15}$$

Z_i and Z_i' must be the same except for an impedance scaling factor L_{ai}/L_i. Using Equation 6.14, Z_i' can be rewritten as

$$\begin{aligned} Z_i' &= \frac{L_{ai}}{L_i} Z_i \\ &= \frac{L_{ai}}{L_i}\left[j\omega L_i + \frac{1}{j\omega C_{i+1}}\right] \\ &= j\omega L_{ai} + \frac{L_{ai}}{j\omega L_i C_{i+1}}. \end{aligned} \tag{6.16}$$

Hence, the impedance inverter can be derived in terms of L_{ai}, L_i, and the

prototype elements g_i and g_{i+1} as

$$\begin{aligned} K_{i,i+1} &= \sqrt{\frac{L_{ai}L_{ai+1}}{L_i C_{i+1}}} \\ &= \sqrt{\frac{L_{ai}L_{ai+1}}{g_i g_{i+1}}} \quad i = 1, 2, ..., n-1. \end{aligned} \tag{6.17}$$

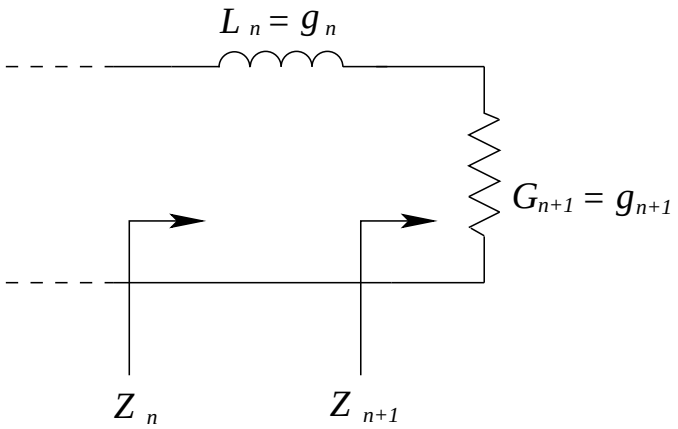

(a) Output end of the low-pass prototype circuit.

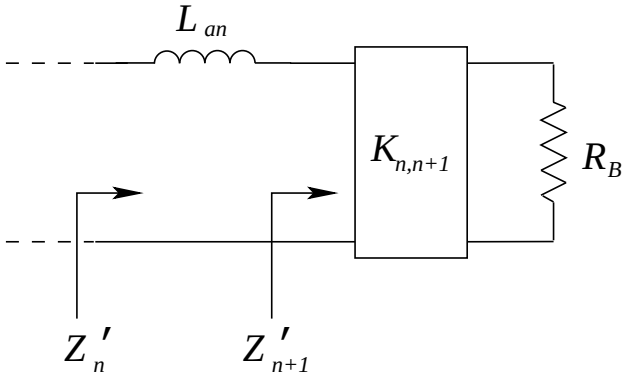

(b) Corresponding K-inverter form of the output end part circuit.

Figure 6.5 Circuits used to derive the formula for K at the end.

This formula is applicable to all the inverters except for those at the input

and output ends shown in Figure 6.3. The expression of K at the output end of the circuit can be determined, as shown in Figure 6.5, by considering the last two elements in Figure 6.1. The corresponding circuit form of Figure 6.5(a) with a K inverter is shown in Figure 6.5(b). Referring to the circuit in Figure 6.5(a), the impedance looking into L_n is

$$Z_n = j\omega L_n + \frac{1}{G_{n+1}}. \tag{6.18}$$

In Figure 6.5(b), the impedance is

$$Z'_n = j\omega L_{an} + \frac{K^2_{n,n+1}}{R_B}. \tag{6.19}$$

Z_n and Z'_n must be equal except for an impedance factor L_{an}/L_n. This leads to the result of K at the output end of the circuit in terms of L_{an}, load impedance, and low-pass prototype elements as

$$K_{n,n+1} = \sqrt{\frac{L_{an}R_B}{g_n g_{n+1}}}. \tag{6.20}$$

Similarly, the impedance inverter at the input end in Figure 6.3 is derived as

$$K_{01} = \sqrt{\frac{L_{a1}R_A}{g_0 g_1}}. \tag{6.21}$$

Then the low-pass to bandpass transformation can be applied to achieve a bandpass filter prototype. The series inductors L_{ai} in Figure 6.3 are replaced by series LC resonators with resonant frequency ω_0 by performing the frequency transformation with the aid of Equation 6.4. The reactance X of the series resonator can be written as

$$jX_a = j\frac{\omega'_1}{\Delta}\left(\frac{\omega}{\omega_0} - \frac{\omega_0}{\omega}\right) L_{ai}, \tag{6.22}$$

where L_{ai} is the series inductor in the low-pass prototype in Figure 6.3.

In order to establish the properties of series resonators, it is convenient to define a reactance slope parameter, which is independent of the forms of the resonator structures, as

$$\chi = \frac{\omega_0}{2}\frac{dX}{d\omega}\Big|_{\omega=\omega_0}. \tag{6.23}$$

Substituting from Equation 6.22, the reactance slope can be expressed in terms of L_{ai} as

$$\begin{aligned}\chi &= \frac{\omega_0}{2}\frac{d}{d\omega}\left[\frac{\omega_1'}{\Delta}\left(\frac{\omega}{\omega_0}-\frac{\omega_0}{\omega}\right)L_{ai}\right]\Big|_{\omega=\omega_0} \\ &= \frac{\omega_1'}{\Delta}L_{ai}\ ,\end{aligned} \tag{6.24}$$

which yields

$$L_{a1} = \frac{\chi_1\Delta}{\omega_1'}, \tag{6.25a}$$

$$L_{ai} = \frac{\chi_i\Delta}{\omega_1'}, \tag{6.25b}$$

$$L_{an} = \frac{\chi_n\Delta}{\omega_1'}. \tag{6.25c}$$

Substitution of these results in Equations 6.17, 6.20, and 6.21 leads to the representation of impedance inverters K in terms of slope parameters, terminating impedances and fractional bandwidth as

$$K_{01} = \sqrt{\frac{R_A\chi_1\Delta}{g_0g_1\omega_1'}}, \tag{6.26a}$$

$$K_{i,i+1} = \frac{\Delta}{\omega_1'}\sqrt{\frac{\chi_i\chi_{i+1}}{g_ig_{i+1}}}\quad i=1,2,...,n-1, \tag{6.26b}$$

$$K_{n,n+1} = \sqrt{\frac{R_B\chi_n\Delta}{g_ng_{n+1}\omega_1'}}. \tag{6.26c}$$

Therefore, the bandpass filter can be designed from the low-pass filter structure

show in Figure 6.1, whose response is determined by the prototype parameters g_0, g_1, ..., g_{n+1}. The corresponding bandpass filter is characterized by the slope parameters χ_1, χ_2, ..., χ_n, terminations R_A and R_B, and fractional bandwidth Δ. The terminations R_A R_B, and the fractional bandwidth Δ can be specified according to the design requirements. Then the desired filter response can be obtained by specifying the impedance inverter parameters K_{01}, K_{12}, ..., $K_{n,n+1}$ as presented in Equations 6.26a to 6.26c.

A generalized bandpass filter prototype using impedance inverters and series resonators is shown in Figure 6.6. The resonator can be represented by the series of inductor L_{ri} and capacitor C_{ri}. The reactance $X_i(\omega)$ of the resonator is

$$X_i(\omega) = L_{ri}\omega - \frac{1}{C_{ri}\omega}, \tag{6.27}$$

where L_{ri} and C_{ri} can be derived from Equation 6.22 as

$$L_{ri} = \frac{\omega_1' L_{ai}}{\Delta\omega_0}, \tag{6.28a}$$

$$C_{ri} = \frac{\Delta}{\omega_1' L_{ai}\omega_0}. \tag{6.28b}$$

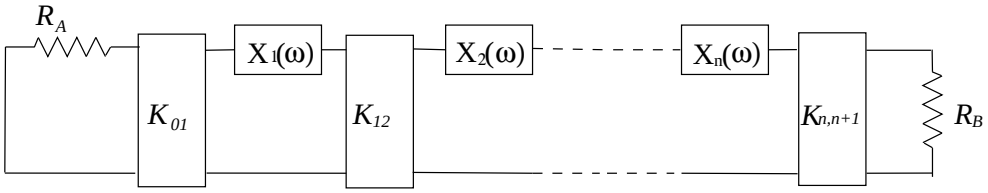

Figure 6.6 Generalized bandpass filter prototype using impedance inverters and series resonators.

For coupled cavity resonators, it is convenient to represent the resonant characteristics by coupling coefficients $k_{i,i+1}$ between adjacent resonators and external Q factor Q_{ext} at both ends of the resonators.

For the interior resonators in Figure 6.6, the coupling between resonators can be represented by a transformer with mutual inductance M, which replaces the

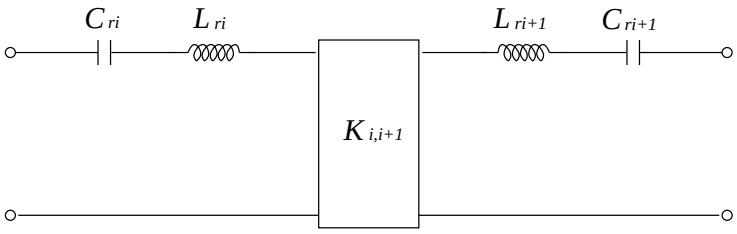

(a) A section of the bandpass filter.

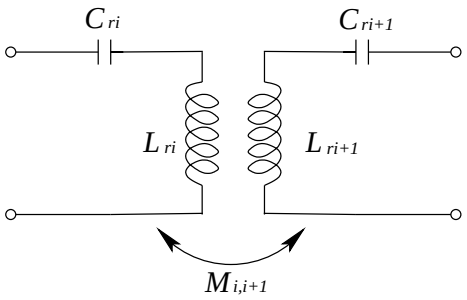

(b) Equivalent transformer coupled form.

Figure 6.7 Circuits used to derive the formula for coupling coefficient k.

ideal K inverter. Figure 6.7(a) shows a section of the bandpass filter consisting of the ith and $(i+1)$th resonators and the K inverter. Its equivalent circuit is the transformer coupled form shown in Figure 6.7(b). From the property of a transformer, the mutual inductance $M_{i,i+1}$ is related to the K inverter in Figure 6.7(a) as

$$K_{i,i+1} = \omega_0 M_{i,i+1}. \tag{6.29}$$

The general definition of the coupling coefficients for the circuit shown in Figure 6.7(b) is

$$k_{i,i+1} = \frac{M_{i,i+1}}{\sqrt{L_{ri} L_{ri+1}}}. \tag{6.30}$$

By substituting L_{ri} and M using Equations 6.28a and 6.29 respectively, and then applying Equation 6.17, the coupling coefficients of the interior resonators of the filter are given by

$$\begin{aligned} k_{i,i+1} &= \frac{K_{i,i+1}}{\omega_0 \sqrt{L_{ri} L_{ri+1}}} \\ &= \frac{\Delta}{\omega_1' \sqrt{g_i g_{i+1}}} \quad i = 1, 2, ..., n-1. \end{aligned} \tag{6.31}$$

The slope parameter for the series LC resonators can be derived based on Equations 6.23 and 6.27 as

$$\chi = \omega_0 L_{ri}. \tag{6.32}$$

Thus, the loaded Q, Q_l, of any series type resonator with a reactance parameter χ and a series resistance R can be expressed as

$$Q_l = \frac{\chi}{R}. \tag{6.33}$$

For the particular case in Figure 6.3, the impedance inverter K_{01} also reflects an impedance of K_{01}^2/R_A to the resonator at the input end, which results in a Q_l represented by

$$Q_l = \frac{\chi}{K_{01}^2/R_A + R}. \tag{6.34}$$

Assuming that the resonator is lossless ($R = 0$), then with Q_u approaching infinity, Q_l becomes Q_{ext}

$$Q_{ext} = \frac{\chi}{K_{01}^2/R_A}. \tag{6.35}$$

Hence, the external Q at the input and output ends of the band pass filter are

$$Q_{extA} = \frac{\chi}{K_{01}^2/R_A} = \frac{g_0 g_1 \omega_1'}{\Delta}, \tag{6.36a}$$

$$Q_{extB} = \frac{\chi}{K_{n,n+1}^2/R_B} = \frac{g_n g_{n+1} \omega_1'}{\Delta}. \tag{6.36b}$$

Therefore, a Chebyshev bandpass filter design, which is specified by the resonant frequency f_0, fractional bandwidth Δ, pass band ripple L_{Ar}, and filter order n, can start with finding the element values g_i for the low-pass filter prototype according to the design requirement. Then the design parameters for the bandpass filter prototype, including external Q, Q_{extA} and Q_{extB} that represent the degree of coupling with the external circuits and the coupling coefficients $k_{i,i+1}$ between each internal resonator, can be derived. The filter simulation procedure is performed based on the knowledge of Q_{extA}, Q_{extB}, and $k_{i,i+1}$, which is described in the next section.

For any practical resonators, loss exists due to finite conductivity of the metal, which is equivalent to parasitic resistance. As a result of the dissipative elements, pass band attenuation is introduced to the filter response. The effect of dissipation can be calculated by introducing the resistive elements into the filter prototype and computing the frequency transfer function with the dissipation included. From the resulting filter response, the increase in the midband attenuation in dB for a

bandpass filter can be estimated by

$$(\Delta L_A)_0 = 8.686 \frac{C_n \omega_1'}{\Delta Q_u} \text{ dB}, \tag{6.37}$$

where C_n is coefficient related to the passband ripple and the number of poles of the filter; Q_u is the unloaded Q of the resonator, with the assumptions that the Q's of all the resonators are the same.

The coupling coefficients between adjacent resonators can be determined by finding the resonant frequencies of the separate single resonators with electric and magnetic walls [53]. The method is described briefly as follows.

The coupling structures between two single mode identical resonant cavities can be modelled by the equivalent circuit shown in Figure 6.8(a). In this Figure, the coupling between the adjacent resonators is represented by a mutual inductance M, which is independent of the type of coupling mechanism. The coupling coefficient k between the resonators is defined as

$$k = \frac{M}{L}. \tag{6.38}$$

To illustrate the method conveniently, an alternative form of the equivalent circuit is employed by dividing the coupling inductance into two parts along the symmetry plane as shown in Figure 6.8(b). This structure leads to two separate resonant states. A single resonant circuit is formed by replacing the symmetry plane by a short circuit (electric wall), as shown in Figure 6.9(a). The resonant frequency f_e corresponding to the equivalent circuit is

$$f_e = \frac{1}{2\pi\sqrt{(L-M)C}}. \tag{6.39}$$

Similarly, the other resonant circuit is formed by replacing the symmetry plane by an open circuit (magnetic wall), as shown in Figure 6.9(b). The resonant

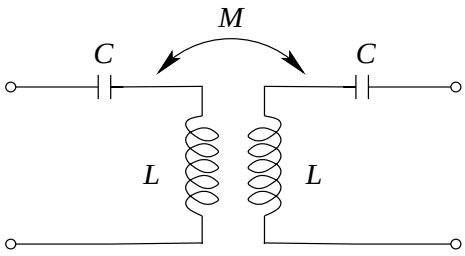

(a) Equivalent circuit.

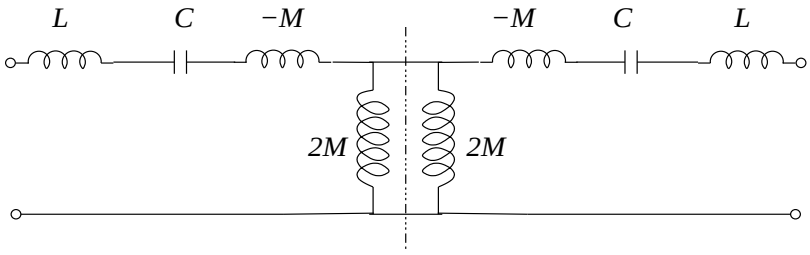

(b) Equivalent circuit by dividing the coupling inductance along the symmetry plane.

Figure 6.8 Two forms of the equivalent circuit of the coupled resonators.

frequency f_m is given by

$$f_m = \frac{1}{2\pi\sqrt{(L+M)C}}. \tag{6.40}$$

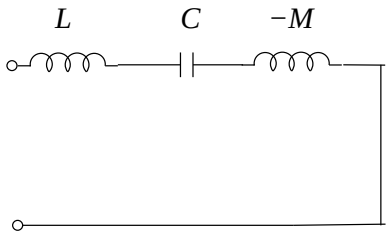

(a) Equivalent circuit with symmetry plane replaced by electric wall.

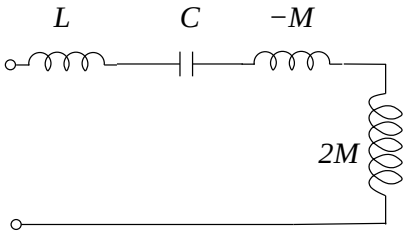

(b) Equivalent circuit with symmetry plane replaced by magnetic wall.

Figure 6.9 Equivalent circuits of the two separate resonators.

Using Equations 6.38 to 6.40, the coupling coefficient k is solved in terms of f_e and f_m as

$$k = \frac{M}{L} = \frac{f_e^2 - f_m^2}{f_e^2 + f_m^2}, \tag{6.41}$$

and the resonant frequency is

$$f_0 = \sqrt{f_e f_m}. \tag{6.42}$$

Therefore, the coupling coefficient can be decided by observing the splitting frequencies of the two coupled resonators. An example of the insertion loss for two identical waveguide resonators coupled by inductive posts is shown in Figure 6.10.

The resonant frequency f_0 of the individual resonator is 24 GHz. The frequency response of the two coupled resonators splits into two resonant states identified as f_e and f_m. f_e shifts towards higher frequency with the value of 24.22 GHz, while f_m shifts towards lower frequency with the value of 23.82 GHz.

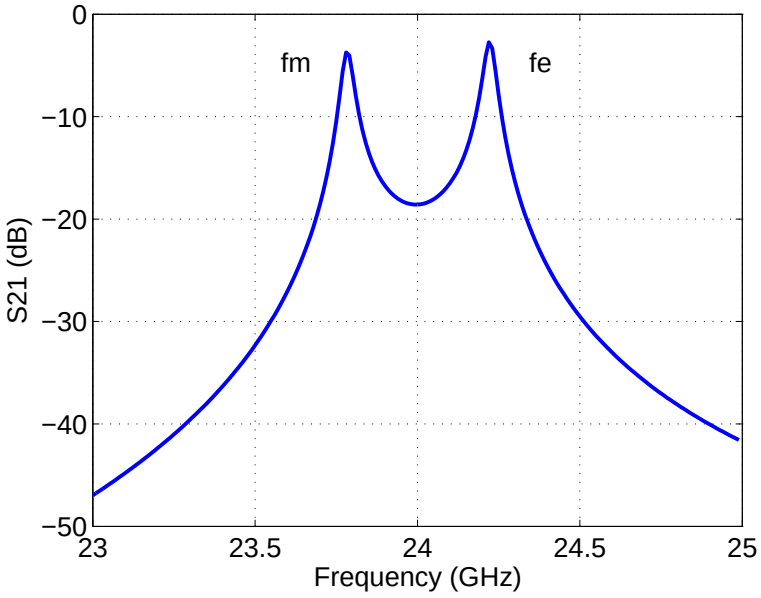

Figure 6.10 Insertion loss curve for two inductive post-coupled waveguide resonators.

6.2 Filter Simulation

The ideal impedance inverter K in the bandpass filter prototype can be realized with lossless inductors as shown in Figure 6.11. The inductance is related to the value of the K inverter by

$$K = \omega L. \tag{6.43}$$

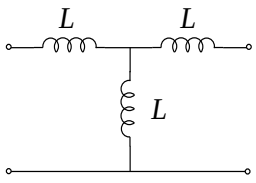

Figure 6.11 Inductor form of impedance inverter.

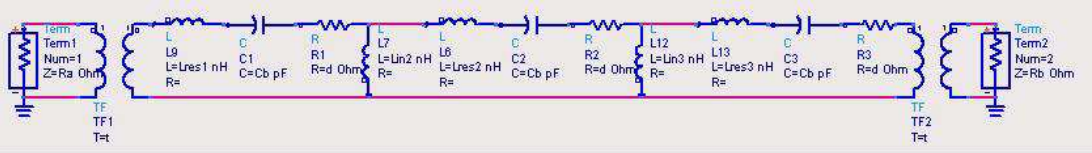

Figure 6.12 ADS model of lumped Chebyshev 3rd bandpass filter.

By replacing the K inverter with the lumped circuit, the third order lumped Chebyshev filter model is simulated with the aid of Advanced Design System (ADS). The complete ADS model of a third order Chebyshev bandpass filter is shown in Figure 6.12. The resonator sections are represented by the RLC series circuits, in which the inductor values are adjusted by subtracting the coupling inductors values at both sides from the impedance inverters. The input and output coupling in the ADS model is provided by ideal transformers, with the turns ratio carefully adjusted to produce the best filter response with $R_a = R_b = 50\ \Omega$.

The passband filter is designed at the center frequency of 24 GHz, with 2% bandwidth and 0.1 dB passband ripple. The component values in the ADS model are derived according to the Equations in Section 6.1. The response of the bandpass filter composed of lossless resonators is shown in Figure 6.13(a). To have a close look at the passband ripple performance, an expansion of S_{21} is provided in Figure 6.13(b). The simulation results from the ADS model satisfy completely the design objectives, which verifies the calculation procedure presented in Section 6.1 for the bandpass filter prototype.

For a practical microwave filter, the resonator components always have finite Q factors. This introduces loss to the filter model, and increases the pass-band attenuation. The effect of the finite resonator Q on the filter response is simulated by adding a series resistor to each resonator section in the ADS model shown in Figure 6.12. For a series resonator, the unloaded Q is related to the dissipative element R as

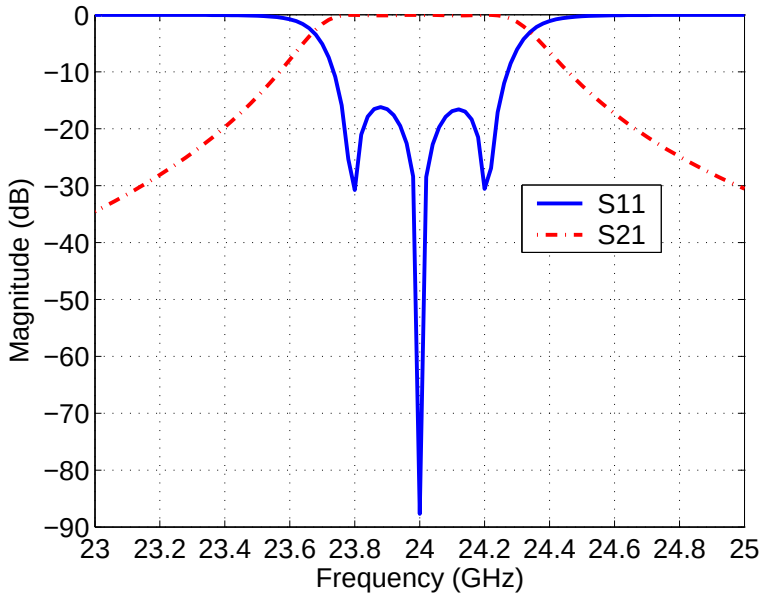

(a) S-parameter.

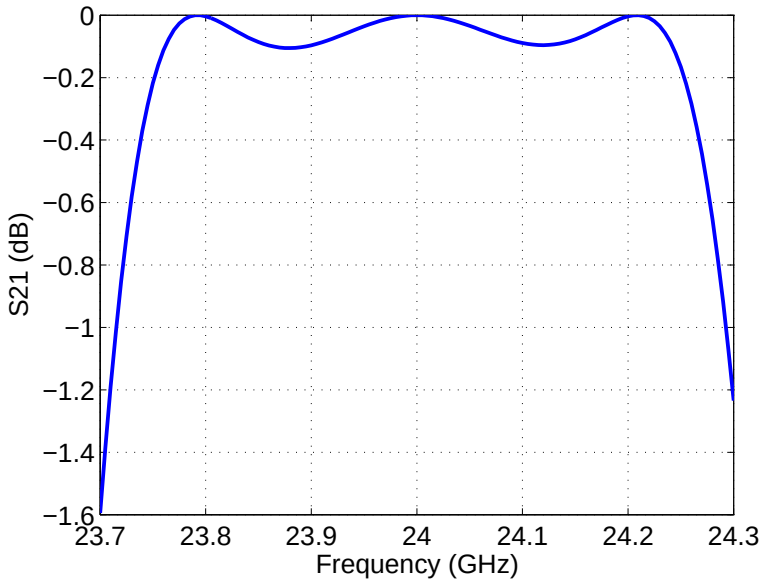

(b) Close-up of S_{21}.

Figure 6.13 Response of the bandpass filter composed of lossless resonators.

$$Q = \frac{\omega_0 L}{R}. \tag{6.44}$$

The values of the resistive elements associated with various sample Qs are calculated using Equation 6.44, and the results are listed in Table 6.1. Also the midband attenuation of the bandpass filter calculated using Equation 6.37 based on the corresponding Q are included in the Table. The lossy ADS models representing filters with varying Q values are simulated, and the responses generated from these models are shown in Figure 6.14. Figure 6.14(a) shows both the transmission and reflection performances of the filters. The expansion of S_{21} is shown in Figure 6.14(b). The out of band performances of these filters are similar, and the major differences occur in the passband. The insertion loss in the passband decreases with the increasing of Q. For example, the midband attenuation for the filter with element Q of 500 is 1.385 dB (see Table 6.1). When expressed in terms of power delivered to the load, such a filter transfers 72.7% of the available power from the source to the load, and 27.3% of the power is dissipated by the filter in the form of heat. In contrast, for a filter with element Q of 2000, the midband attenuation is 0.348 dB, which means 92.3% of the available power from the source is delivered to the load, and only 7.0% of the power is dissipated by the filter. The difference between $Q = 2000$ and $Q = 500$ results in about 27.0% increase in power delivered to the load by the filter at the center frequency. Also observed from these results is the increasing of the passband ripple with the decrease of the element Q, especially for filters with $Q < 2000$. In this case, the parameters for the bandpass filter prototype design derived using equations in Section 6.1 need to be modified to meet the original design specifications.

The lumped ADS models used to demonstrate the effect of finite element Q on the filter performance does not incorporate other influencing factors, such as the losses of the impedance converters and the loading systems. Thus, the insertion loss of a practical filter would be worse than the result simulated using ADS

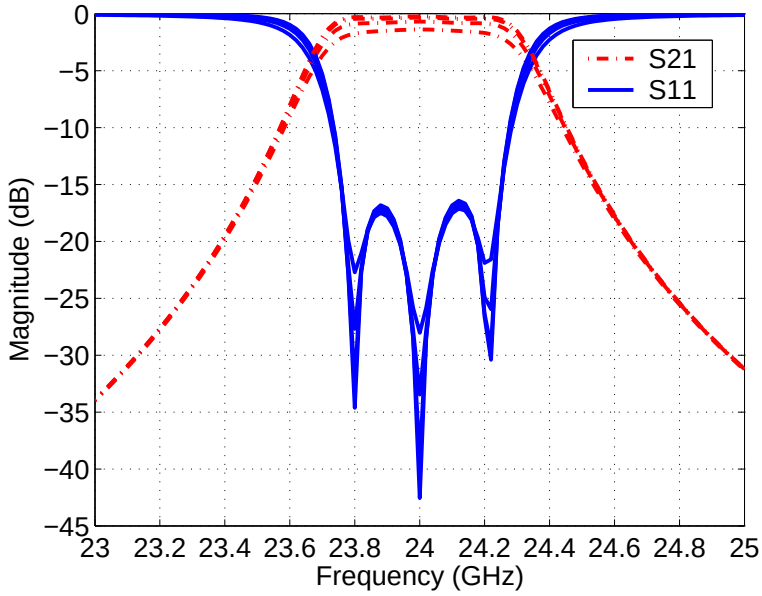

(a) S-parameter.

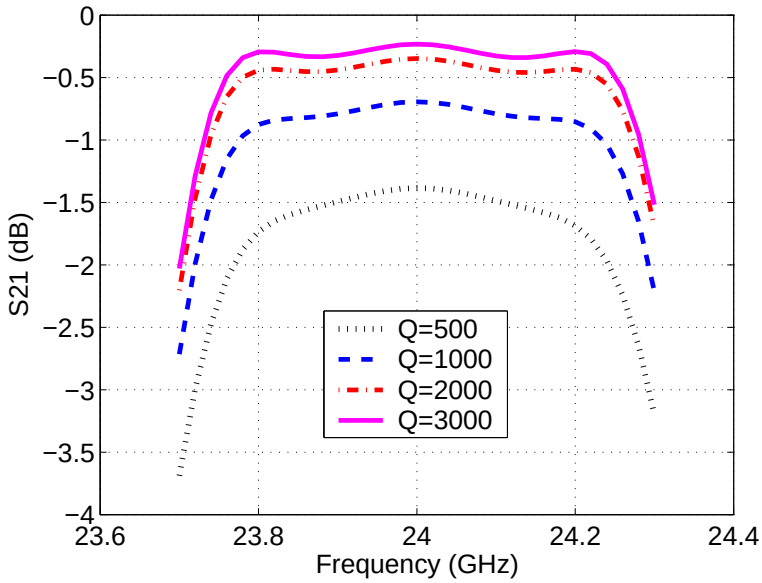

(b) Close-up of S_{21}.

Figure 6.14 Responses generated from the lossy ADS models representing filters with varying Q values.

Table 6.1 Values of the resistive elements and midband attenuation associated with the corresponding Qs.

Q	500	1000	2000	3000
$R(\Omega)$	0.1	0.05	0.025	0.0167
Attenuation calculated (dB)	1.390	0.695	0.347	0.232
Attenuation simulated (dB)	1.385	0.695	0.348	0.232

lumped model shown in Figure 6.12.

Practical impedance inverters in waveguides can be realized by many structures. A simple form of realization is metal posts spaced along the broad wall of the waveguide. A two-dimension top view of a post filter is shown in Figure 6.15. The equivalent circuit for shunt posts [54] in the waveguide is shown in Figure 6.16. This circuit configuration operates as an impedance inverter and a piece of transmission line with the electrical length of $\phi/2$ is connected to both ends of the impedance inverter. The electrical length $\phi/2$ is generally negative except for the case of large posts. The transmission line with the positive or negative electrical length can be added or subtracted from the adjacent $\lambda/2$-long transmission line of the resonators of the same characteristic impedance. Therefore, the electrical length θ of the resonator between the centers of the posts in Figure 6.15 is

$$\theta_i = \pi + \frac{1}{2}(\phi_{i-1,i} + \phi_{i,i+1}). \tag{6.45}$$

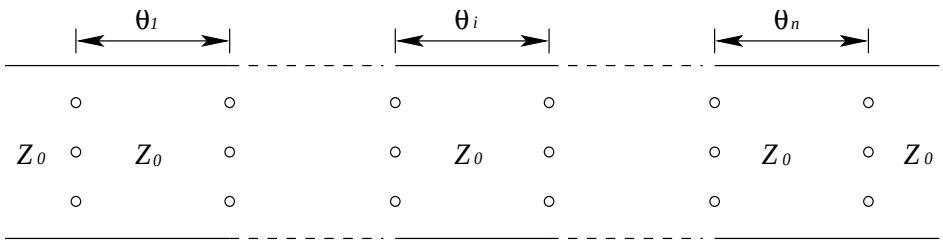

Figure 6.15 Top view of a post filter.

The configuration of the proposed waveguide filter is shown in Figure 6.17,

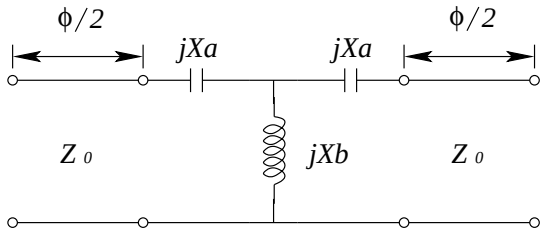

Figure 6.16 Equivalent circuit for shunt posts.

where the cavities are couple by five metallic cylindrical posts, which provide inductive couplings required between adjacent resonant cavities. Compared to the structure employing a single post located at the center of the broad wall, a symmetrically placed multiple post configuration provides better stop band performance by cancelling out some higher order modes, thus reducing their interaction [55]. Similar to the coupling structure employed by the cavity resonator shown in Figure 4.6, two coupling slots in the ground plane of the top Al_2O_3 substrate couple the energy from the input and output microstrip feed lines into the filter. The slots are located at approximately $L_1/4$ from the end of the cavities in order to get maximum coupling. The feed line length between the end of the open-circuited stub and the center of the slot is $\lambda_g/4$, which provides an electric short circuit at the slot and thus maximum current flow.

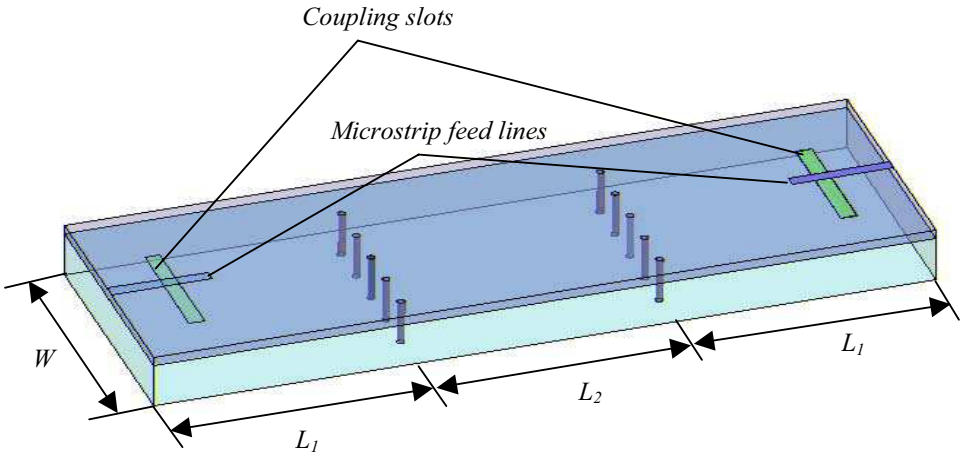

Figure 6.17 3-pole multiple post filter structure.

As demonstrated in Figure 6.14, for a 3-pole Chebyshev filter with resonator element Q of about 2700, which is potentially achievable by a LIGA fabricated resonator (see Section 4.3), the filter response only deteriorates slightly by the introduction of the dissipative elements due to the corresponding finite element Qs. Therefore, the parameters needed for the filter design can be calculated using the equations provided by the filter theory in Section 6.1 without corrections. Based on the desired filter characteristic, the element values for the low-pass filter prototype are: $g_0 = g_4 = 1$, $g_1 = g_3 = 1.032$, $g_2 = 1.147$. The coupling coefficients between the adjacent resonator sections for the bandpass filter are calculated to be $k_{1,2} = k_{2,3} = 0.018$. Since the filter geometry is symmetric, the input and output external Q factors are equal and found to be $Q_{extA} = Q_{extB} = 51.58$.

The design of the filter is accomplished with the aid of HFSS. Due to the symmetric property of the filter, a 2-pole filter HFSS model composed of two identical resonators coupled by 5 equally-spaced posts along the broad wall of the waveguide, as represented in Figure 6.18, is simulated to get the proper coupling coefficient $k_{1,2}$, $k_{2,3}$, and the middle resonator length L_2.

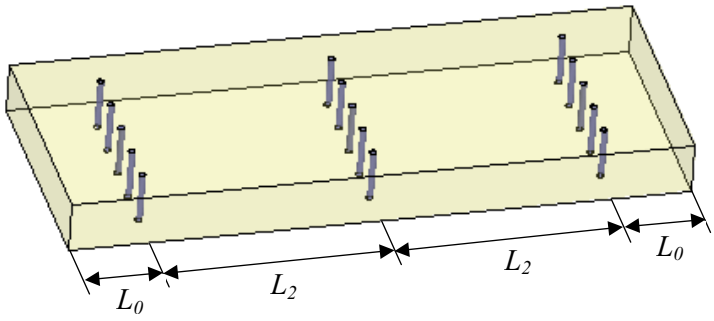

Figure 6.18 HFSS model for internal coupling coefficient k.

As known from the equivalent circuit for the shunt inductive posts, this type of impedance inverter implementation introduces a transmission line section, whose length is associated with the physical dimensions of the metallic posts. The electrical distance of the resonator between the centers of the posts is altered by

subtracting the lengths introduced at each end of the resonator from π, which is nominal for a waveguide resonator. Thus, while the diameters r_a of the posts are adjusted to provide the desired coupling coefficients between internal resonators, the resonator length L_2 has to be changed simultaneously. Based on the HFSS model shown in Figure 6.18, simulations are run for different post diameters r_a and resonator length L_2. The width W of the filter is chosen to be 8.829 mm, the same as the cavity resonator presented in Chapter 4. The coupling coefficient ($k_{1,2} = k_{2,3}$) and the center frequency (f_0) as a function of the length of the resonator (L_2) are shown in Figure 6.19(a) and Figure 6.19(b) respectively, in which the coupling coefficient and center frequency are obtained by locating f_e and f_m from the filter response and then calculating using Equations 6.41 and 6.42, respectively. Figure 6.19 demonstrates that reducing the multi-post diameter results in the increasing of the coupling coefficient k, while decreasing of the center frequency f_0. Based on the results in Figure 6.19, the post diameter $r_a = 0.12$ mm and resonator length $L_2 = 8.57$ mm are selected, which provide the desired coupling coefficient and center frequency.

The next step is to find the proper external Q for the input and output resonator sections, which is performed by adjusting the dimension of the coupling slot. The HFSS model used to extract Q_{ext} is shown in Figure 6.20. Q_{ext} can be obtained from the phase response of S_{11} [32]. In this case, the feed line needs to be de-embedded to the detuned-open position. The distance to the displacement of the detuned-open is subtracted from each phase point. The detuned-open positions are half wavelength apart on the microstrip feed line. The detuned-open position of the HFSS model can be found by observing the phase of S_{11}. At resonance, the phase of de-embedded S_{11} curve passes 0^o. As frequency increases, the phase angle of the input impedance decreases from 0^o to -180^o. Likewise, as the frequency decreases from the resonance along the impedance locus, the phase increases from 0^o to $+180^o$. With the aid of the post processing function provided by HFSS, the reference plane in the HFSS model can be rapidly de-embedded to

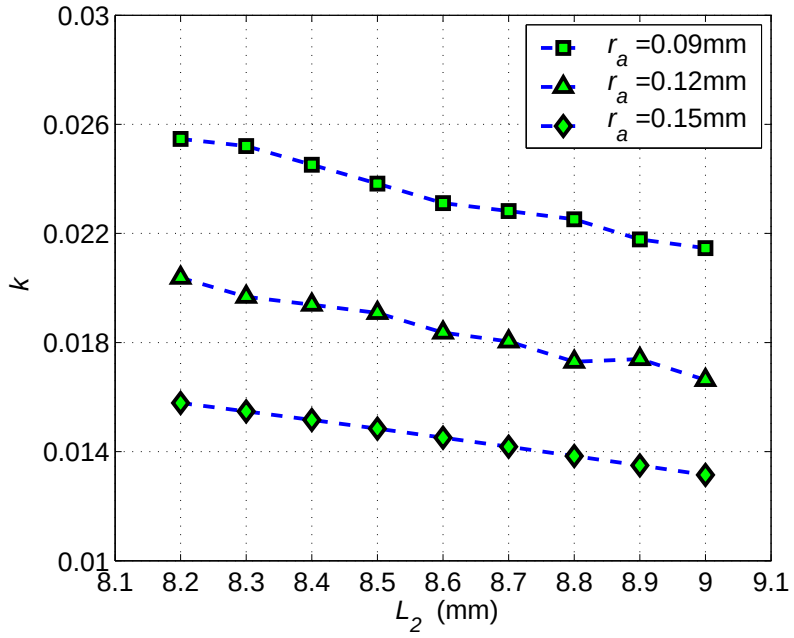

(a) Coupling coefficient.

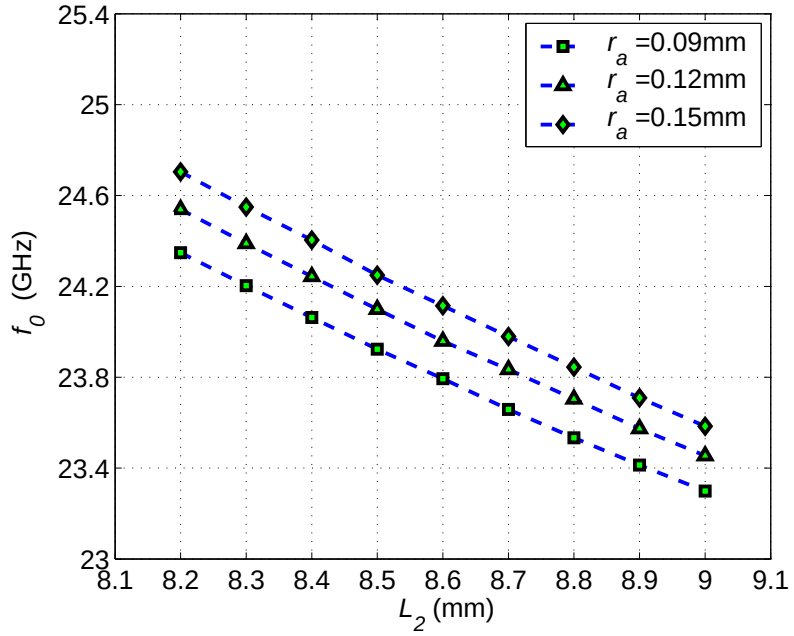

(b) Center frequency.

Figure 6.19 Coupling coefficient ($k_{1,2} = k_{2,3}$) and the center frequency (f_0) as a function of the length of the resonator (L_2) for different diameters of the posts.

any position. The correct de-embedded distance is found by moving the reference plane along the feeding transmission line iteratively. An example of S_{11} phase curve de-embedded to the detuned-open position is shown in Figure 6.21, with both the original port location data and the de-embedded data displayed. At the resonant frequency f_0, the phase curve crosses 0^o, and is symmetrical about the 0^o point.

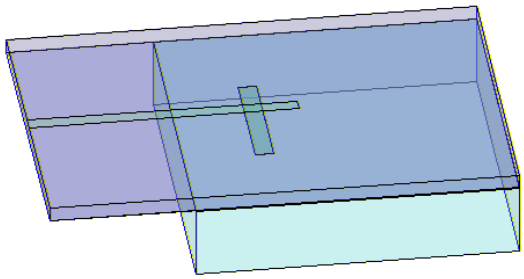

Figure 6.20 HFSS model for external Q Q_e.

Q_{ext} can be solved using the information given by the phase plot. In the overcoupled case ($k > 1$), the frequencies f_1 and f_2 corresponds to the points where the curve passed through $\pm 90^o$, as shown in Figure 6.21. For the coupling coefficient $k >> 1$, Q_{ext} is given by

$$Q_{ext} = \frac{f_0}{f_2 - f_1} \ . \tag{6.46}$$

An HFSS model as shown in Figure 6.20 is simulated. The simulation is run for slots of constant width (0.5 mm) but varying length. External Q is determined from the phase response of S_{11} using Equation 6.46. The external coupling as a function of slot length is shown in Figure 6.22. Nonlinear regression is used to determine a curve fitted to the data, and a slot of 4.45 mm $\times$ 0.5 mm is chosen.

The length of resonators (L_1) at the input and output ends of the filter is determined through the simulation of two post coupled cavities fed by microstrip lines via slots (see HFSS model in Figure 6.23). The dimension of the slots and di-

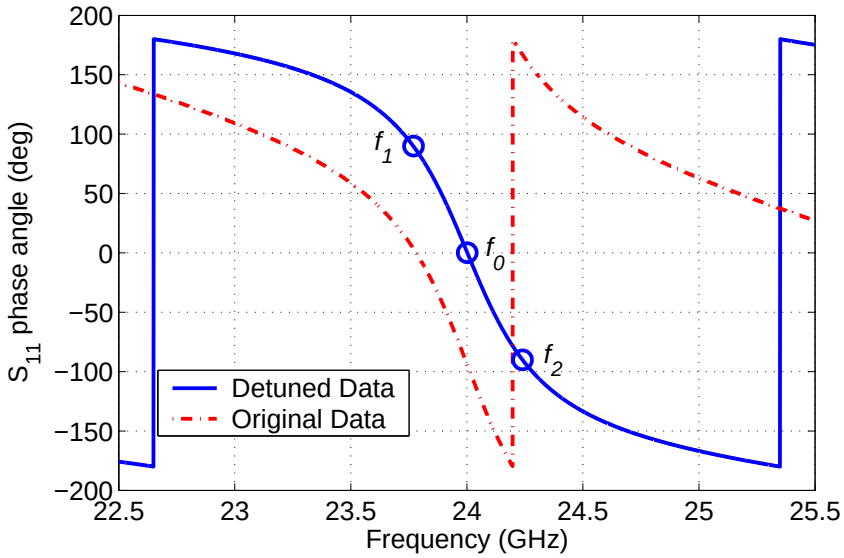

Figure 6.21 Example of de-embedded S_{11} phase angle.

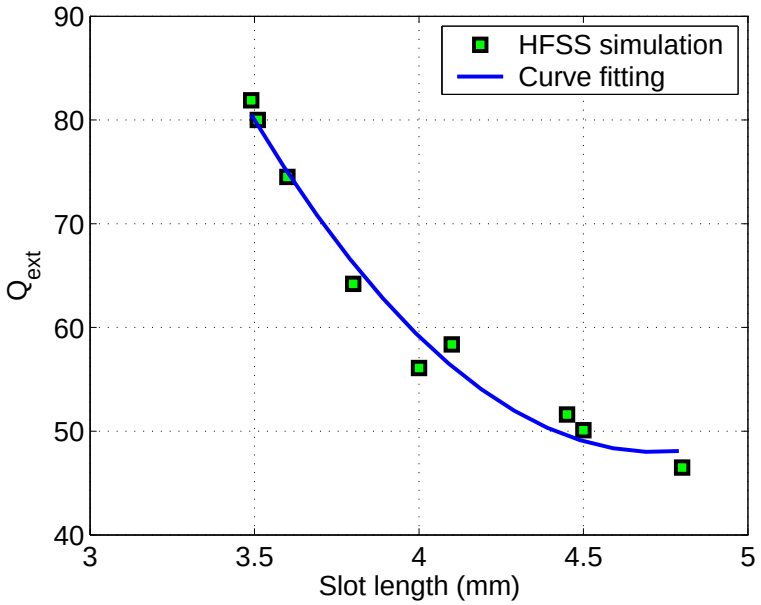

Figure 6.22 External Q versus slot length, curve fit to HFSS simulation results. Slot width is constant at 0.5 mm.

ameter of the posts are fixed with the values of $L_2 = 8.571$ mm and $r_a = 0.12$ mm, derived from the previous simulation, while the resonator length L_1 is varied to provide the desired center frequency. The center frequency, as determined by Equation 6.42, is plotted versus the length of resonators (L_1) in Figure 6.24. A cavity length of $L_1 = 8.68$ mm is chosen to provide the desired center frequency of 24 GHz.

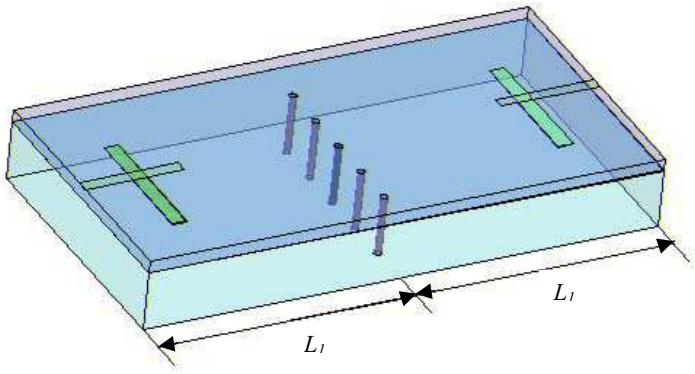

Figure 6.23 HFSS model for the length of resonators (L_1) at the input and output ends of the filter.

With the slot length and cavity size determined, the complete filter is modelled in HFSS. The simulated results are shown in Figure 6.25. The HFSS modelled filter is identical to Figure 6.17. The model consists of two parts. The top wafer is 400 μm thick Al_2O_3 and has two sections of microstrip feed line on the top side coupled to two slot apertures in the ground plane on the bottom side. The bottom waveguide section, including three cavities and coupling posts between adjacent cavities, could be fabricated using the LIGA process. Filter dimensions and detailed properties are listed in Table 6.2.

The filter structures composed of three cavities with metallic multi-post coupling proposed in this chapter would be extremely difficult to fabricate using traditional machining techniques, due to the extremely fine post structure and high vertical aspect ratio required. However, these types of structures could be ideal

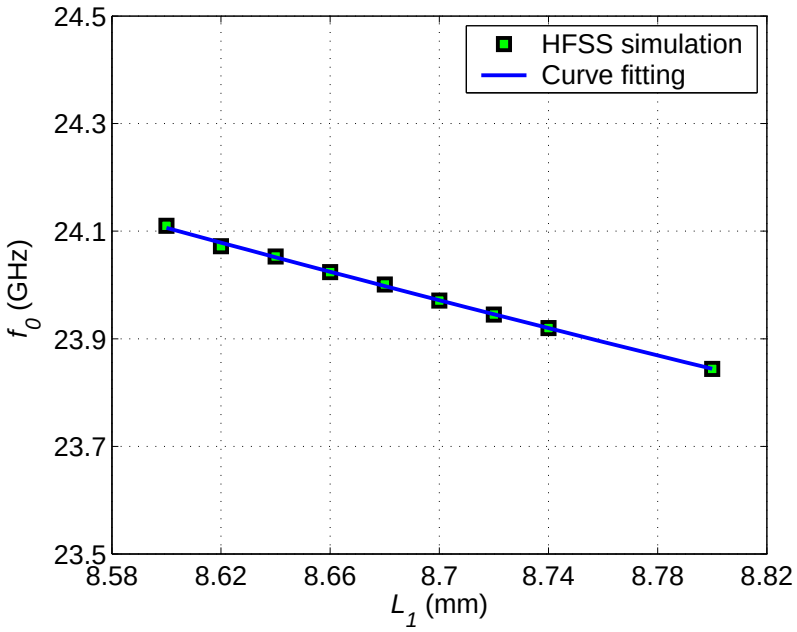

Figure 6.24 The center frequency as a function of the length of resonators (L_1) at the input and output ends of the filter.

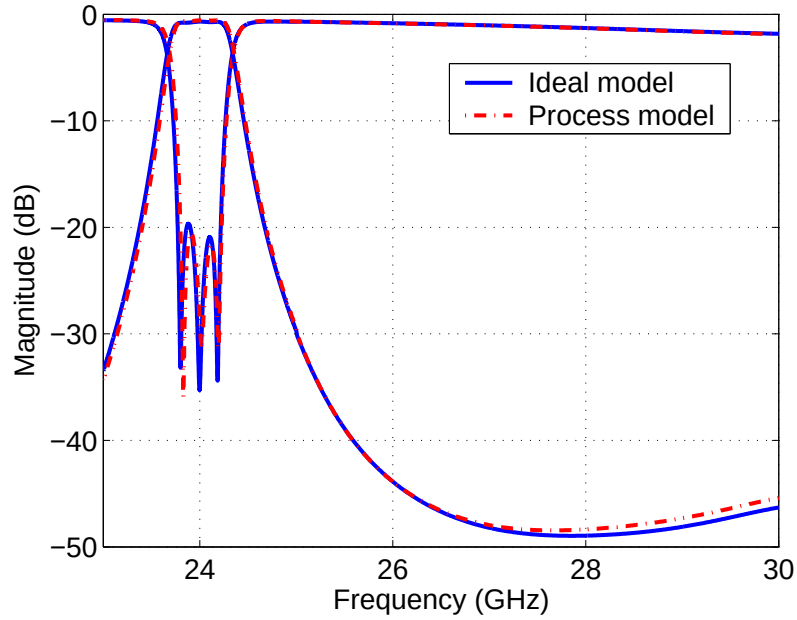

Figure 6.25 HFSS simulation results of 3-pole filters.

Table 6.2 Summary of dimensions and detailed properties of ideal filter model and process condition filter model

Parameter	Ideal filter	Process condition filter
Height of resonators (mm)	2	2
Length of input/output resonator L_1 (mm)	8.68	8.68
Length of the second resonator L_2 (mm)	8.571	8.571
Diameter of posts r_a (mm)	0.12	0.12
Center Frequency f_{res}(GHz)	24.013	24.026
Bandwidth (MHz)	424	434
Insertion loss (dB)	0.69	0.59
Ripple (dB)	0.1	0.1
Stop band attenuation (dB) (20% off f_{res})	48.38	47.6

for LIGA fabrication, which offers sub-micron features, aspect ratios of 100:1 or higher, resist thicknesses of up to 3 mm, and almost vertical and optically smooth sidewalls [56] [57]. To investigate the effect of the fabrication process on the performance of the filter, a filter model based on a measured PMMA resonant cavity structure fabricated using the LIGA technique [58] [59] is simulated. In this model, r.m.s roughness of 30 nm is applied to the inside surface of the closed waveguide as well as the post surface, and a size reduction at the top of the cavity body on lateral dimensions by 16 μm in the x direction and 12 μm in the y direction is also incorporated. The HFSS simulated response of the process condition model is also shown in Figure 6.25, for ease of comparison. Compared with the ideal model with 90^o vertical sidewalls and smooth waveguide and post surfaces, the center frequency of the process filter model is increased slightly due to slight polymer shrinkage in the guide top dimensions. The insertion loss is actually slightly better, at the expense of a broader bandwidth and lower stop band attenuation. The close results from the two models suggest that the LIGA fabrication process introduces minor deteriorations and high performance microwave filters with fine structure are possible.

6.3 Summary

A narrow band microwave filter suitable for LIGA fabrication was presented. The filter consisted of three resonant cavities coupled by symmetrically placed metallic posts. The simulation results from the HFSS model incorporating the practical fabrication tolerances measured from a LIGA fabricated PMMA resonator structure suggest that high performance filters can be potentially realized at microwave frequencies using the LIGA process. The performance of the filter can be further improved by employing even deeper cavities with higher Q values, as LIGA is capable of realizing tall and fine structures with large aspect ratios. Furthermore, inexpensive large-scale fabrication is possible by using LIGA replication techniques, such as hot embossing or injection moulding, which utilize a metal moulding tool formed by electroplating metal into X-ray patterned photoresist, without going back to the lithographic step.

Chapter 7

CONCLUSIONS

7.1 Summary and Conclusions

High performance microwave cavities for various circuits in the front-end of transceivers such as filters, diplexers, and oscillators have conventionally been built with rectangular or cylindrical metallic waveguides, which typically have low loss, high quality factor, and higher power handling capability. However such waveguide cavity based circuits made by traditional metal machining techniques tend to be costly, particularly for complex multiple cavity based circuits, and not well suited to high volume commercial applications and integration with planar microwave integrated circuits. As commercial transceiver applications progress toward higher microwave and millimetre-wave frequencies, the use of waveguide based circuits for compact, highly integrated transceivers is becoming feasible, along with an increasing need for cost effective batch fabrication processes for realizing complex metallic cavity circuits without sacrificing structural quality and performance. It is expected that significant advancements in both microwave performance and integration will be achieved through the development of novel technologies for realizing vertically oriented 3-D structures [60].

Silicon bulk micromachining has become one popular approach for fabricating microwave cavity resonators and filters using both anisotropic wet etching and also deep RIE etching techniques. However, the anisotropic wet etching approach does not produce rectangular cavities, but rather ones with non-vertical sidewalls, typically at 54.7 degrees relative to the horizontal plane. Deep RIE technology

can be used to realize cavities in silicon with better sidewall verticality, however the sidewall quality (roughness) varies with processing conditions and can be relatively rough, potentially leading to increased metal conductor loss and a decrease in Q-factor performance. Q factor also increases as a function of increasing cavity height. Unfortunately, due to the thickness limitation of standard silicon substrates, which is typically 525 μm or 650 μm, cavities fabricated on silicon wafers by etching cannot be easily made deeper, without resorting to stacking of multiple wavers which could result in alignment and interface problems, as well as giving "saw-tooth" varying sidewall profiles in the case of non-vertical anisotropic etched wafers.

LTCC is another option for fabricating 3-D circuits and modules with compact size and reduced weight. Realized by replacing solid metal sidewalls with rows of via holes, LTCC resonators introduce extra power dissipation through the posts. Multiple rows of vias are usually employed to produce a negligible leakage loss, which leads to a larger overall structure than an equivalent metallic cavity with solid walls. Although the radiation loss of the LTCC resonator could be minimized by employing multiple layers of vias, the dielectric loss is the major limitation in the Q possibly obtained by this technology, even for the extreme case that an air cavity is put inside the LTCC resonator.

Polymer-based fabrication is a promising alternative to silicon etching and LTCC technologies for the batch fabrication of ultra-deep microwave cavity structures. In particular, deep X-ray lithography, as part of the LIGA process, is a microfabrication technology for precisely structuring polymers, and is increasingly being applied to RF/microwave microstructures. In addition to precise patterning capabilities, deep XRL is able to structure ultra-deep cavities due to the penetration ability of hard X-rays. Cavities of several millimetres are possible in a single lithographic exposure, and with excellent sidewall quality, including verticality near 90 degrees and surface roughness on the order on tens of nanometres. These structured polymers are subsequently used as electroforming templates for

fabricating metal structures with correspondingly good sidewall quality.

The main objectives of the research were defined to be:

1. Investigate the advantage of realizing high Q cavity resonators using the LIGA technique over silicon micromachining and LTCC techniques.

2. Design one-port rectangular cavity resonator structures suitable for LIGA implementation at upper microwave and millimetre-wave frequencies, such as 24 GHz and 37 GHz.

3. Fabricate the resonators, which involves creating the suitable layout of the mask for LIGA cavities, a top substrate, and the assembly of the resonators.

4. Test the resonators and determine the unloaded Q, and compare with the simulation results.

5. Investigate the feasibility of realizing high performance filters as an extension of the LIGA cavity concept.

The first objective was satisfied by HFSS simulation of resonant cavity models representing different fabrication techniques. The simulation results demonstrate that smooth LIGA cavity structures result in promising Q improvement over silicon and LTCC structures, and the potential advantages of LIGA resonators are more dramatic with increasing cavity height and operating frequency.

A complete one-port cavity resonator structure with the external coupling circuit was designed and simulated. Sample 1.8 mm deep polymer cavity structures were fabricated using deep XRL. Excellent sidewall verticality is obtained with the PMMA structure, with only slight shrinkage at the top surface of 8.5 $\pm$ 2.5 μm in either lateral dimensions. This corresponds to sidewalls with verticality between 89.82^o and 89.9^o. Also the PMMA structure shows excellent sidewall surface quality, measured to be on the order of 26 $\pm$ 12 nm for structures of similar height using the deep XRL process at IMT [46]. The structured polymers are subsequently used as templates for metal electroforming to produce cavity resonators. The performance of the resonator was measured using a RT/duroid^{TM} 6010 soft substrate patterned with coupling structures to form the sixth side, thus

completing the cavity. Despite the rather crude test assembly for the sixth side made by clamping, the measured resonator has a high unloaded Q of 2122.2±85 at the resonant frequency of 24 GHz, indicating that LIGA cavities are especially promising for high performance, low-cost applications.

The feasibility of extending such high performance cavity structures to more complicated waveguide-based filter circuits at microwave frequencies was investigated using an application example of a multi-post coupled third order Chebyshev bandpass filter. The simulation results suggest that high performance filters can be potentially realized at microwave frequencies using the LIGA process in a single lithographic exposure.

This research has proved that LIGA is a promising technique for realizing high performance cavity resonators and filters at microwave and millimetre-wave frequencies.

Unlike the cavity structures made by other micromachining techniques, with which the Q factor of the rectangular resonant cavities is limited by the surface roughness of interior walls, cavity shape, or cavity height, tall cavity structures made by deep XRL demonstrate almost 90 degree sidewall verticality and excellent smoothness. As a result, the improved performance in Q factor can be achieved for the resonator employing the LIGA resonant cavity.

The relatively simple, single-step lithographic exposure also facilitates extension to more structurally complicated waveguides and multiple cavity-based circuits, such as the post coupled Chebyshev bandpass filter proposed in this research work. In addition to potentially batch fabricating such a filter lithographically by exposing the entire waveguide depth in a single exposure, the filter structures composed of three cavities with metallic multi-post coupling would be extremely difficult to fabricate using traditional machining techniques, due to the extremely fine post structure and high vertical aspect ratio required. However, these types of structures could be ideal for LIGA fabrication, which offers sub-micron features, aspect ratios of 100:1 or higher, resist thicknesses of up to 3 mm, and almost

vertical and optically smooth sidewalls [56] [57]. Also, representative LIGA sidewall roughness is used to predict very low loss and high performance, suggesting that complicated structures with multiple resonator circuits and high internal components with high aspect ratios are possible.

7.2 Future Work

7.2.1 Improving the Current Design

The resonator measured in this thesis employs a soft substrate as the sixth side of the cavity structure. Although it is cost effective and easy for laboratory fabrication, the substrate surface roughness and loss tangent are worse than those of alumina which introduces more conductor and dielectric losses. The Q_u performance could be further improved by using a fine polished and low loss Al_2O_3 substrate.

In this thesis, the alignment between the substrate and the cavity is made manually. Although simulation results show that the inaccurate alignment has limited effect on Q_u (for instance 1-2%), the issue could cause more impact on the performance of the bandpass filter, since misalignment would cause filter structure asymmetry. A more exact method of aligning can be accomplished with the aid of equipment such as an infrared aligner.

The resonators in this thesis are measured under rather crude assembly for the sixth side by clamping due to the equipment limitations. Better bonding between the feed wafer and the cavity could be offered by using conductive epoxy cured at a higher temperature, for example 80^oC. However the silver epoxy bonding can lead to an increase in the loss, since it can have conductivity values lower than that of gold at high frequencies above 20 GHz [61]. Alternatively, the thermal compression gold-to-gold bonding in a vacuum bond chamber is proved to be capable of providing a quality bond for high Q microwave components [18] [14].

Also the reasons that lead to the unexpectedly low Q during the 37 GHz resonator measurement need to be further investigated. It is expected that by

employing a thinner top substrate that could support only a Quasi-TEM mode at 37 GHz, a much higher Q close to the simulation result could be achieved.

7.2.2 Dual-mode Cavity Filters

Dual-mode filters employ coupling screws or square corner cuts in the cavity to produce degenerate mode coupling [62] [63] [64], such as TE_{011} and TE_{101}, in a single resonator. The coupling between pairs of dual modes in adjacent cavities provides an additional mechanism, producing full filter functions. Dual mode filters offer the desired features of smaller sizes and less mass than conventional single mode coupled filters. In order to generate the degenerate modes with the same resonant frequency, the waveguide cavity is required to be square, which means the height of the cavity, as well as the length of the cavity, has to be half the guide wavelength. At 37 GHz, the cavities are required to be approximately 5.7 mm in height. This height can only be achieved by many wafers stacked together if using silicon-based micromachining methods, however is potentially realizable using one step X-ray lithography.

Bibliography

[1] C. Eklund, R. B. Marks, K. L. Stanwood, and S. Wang, "IEEE Standard 802.16: a technical overview of the wirelessMAN^{TM} air interface for broadband wireless access," *IEEE Communications Magazine*, vol. 40, no. 6, pp. 97–107, June 2002.

[2] Y. Imanaka, *Multilayered Low Temperature Cofired Ceramics (LTCC) Technology*, Springer, New York, 2005.

[3] E. W. Becker, W. Ehrfeld, P. Hagmann, A. Maner, and D. Münchmeyer, "Fabrication of microstructures with high aspect ratios and great structural heights by synchrotron radiation lithography, galvanoforming and plastic moulding (LIGA process)," *Microelectronic Engineering*, vol. 4, no. 1, pp. 34–35, May 1986.

[4] M. J. Madou, *Fundamentals of Microfabrication: the Science of Miniaturization*, CRC Press, Boston, 2002.

[5] D. M. Pozar, *Microwave Engineering*, John Wiley & Sons, Inc., New York, NY, 1998.

[6] R. K. Hoffmann, *Handbook of Microwave Integrated Circuits*, Artech House, Inc., Norwood, MA, 1987.

[7] T. M. Weller, M. I. Herman, P. D. Wamhof, K. Lee, E. A. Kolawa, and B. H. Tai, "New results using membrane-supported circuits: a Ka-band power amplifier and survivability testing," *IEEE Transactions on Microwave Theory and Techniques*, vol. 44, no. 9, pp. 1603–1606, September 1996.

[8] C. T.-C. Nguyen, L.P B. Katehi, and G. M. Rebeiz, "Micromachined devices for wireless communications," in *Proceedings of the IEEE*, Piscataway, NJ, August 1998, pp. 1756–1768.

[9] E. Holzman and R. Robertson, *Solid-State Microwave Power Oscillator Design*, Artech House, Boston, 1992.

[10] J. Papapolymerou, J. Cheng, J. East, and L.P.B. Katehi, "A micromachined high-Q X-band resonator," *IEEE Microwave and Guided Wave Letters*, vol. 7, no. 6, pp. 168–170, June 1997.

[11] N. Maluf, *An Introduction to Microelectromechanical Systems Engineering*, Artech House, Boston, 2000.

[12] A. R. Brown, P. Blondy, and G. M. Rebeiz, "Microwave and millimetre-wave high-Q micromachined resonators," *International Journal of RF and Microwave Computer-Aided Engineering*, vol. 9, no. 4, pp. 326–337, July 1999.

[13] M. Stickel, G. V. Eleftheriades, and P. Kremer, "High-Q bulk micromachined silicon cavity resonator at Ka-band," *Electronics Letters*, vol. 37, no. 7, pp. 433–435, March 2001.

[14] L. Harle and L.P.B. Katehi, "A silicon micromachined four-pole linear phase filter," *IEEE Transactions on Microwave Theory and Techniques*, vol. 52, no. 6, pp. 1598–1607, June 2004.

[15] A. El-Tager, J. Bray, and L. Roy, "High-Q LTCC resonator for millimeter wave applications," in *IEEE MTT-S International Microwave Symposium Digest*, Philadelphia, PA, June 2003, pp. 2257–2260.

[16] J. Lee, S. Pinel, J. Papapolymerou, J. Laskar, and M. Tentzeris, "Low-loss LTCC cavity filters using system-on-pakage technology at 60 GHz," *IEEE*

Transactions on Microwave Theory and Techniques, vol. 53, no. 12, pp. 3817–3823, December 2005.

[17] P. Ferrand, D. Baillargeat, S. Verdeyme, J. Puech, M. Lahti, and T. Jaakola, "LTCC reduced-size bandpass filters based on capacitively loaded cavities for Q band application," in *IEEE MTT-S International Symposium Digest*, Long Beach, CA, June 2005, pp. 1789–1792.

[18] L. Harle and L.P.B. Katehi, "A vertically integrated micromachined filter," *IEEE Transactions on Microwave Theory and Techniques*, vol. 50, no. 9, pp. 2063–2068, September 2002.

[19] X. Gong, W. J. Chappell, and L.P.B. Katehi, "Multifunctional substrates for high-frequency applications," *Microwave and Wireless Component Letters*, vol. 13, no. 10, pp. 428–430, October 2003.

[20] T. L. Willke and S. S. Gearhart, "Novel micromachined LIGA microstrip transmission lines and filters," in *IEEE MTT-S International Microwave Symposium Digest*, San Francisco, CA, June 1996, pp. 1189–1192.

[21] T. L. Willke and S. S. Gearhart, "LIGA micromachined planner transmission lines and filters," *IEEE Transactions on Microwave Theory and Techniques*, vol. 45, no. 10, pp. 1681–1688, October 1997.

[22] K.-Y. Park, J.-C. Lee, J.-H. Kim, B. Lee, N.-Y. Kim, J.-Y. Park, G.-H. Kim, J.-U. Bu, and K.-W. Chung, "A new three-dimensional 30 GHz band-pass filter using the LIGA micromachined process," *Microwave and Optical Technology Letters*, vol. 30, no. 3, pp. 199–201, August 2001.

[23] T. L. Willke and S. S. Gearhart, "Micromachined thick-metal coplanar coupled-line filters and couplers," in *IEEE MTT-S International Microwave Symposium Digest*, Baltimore, MD, June 1998, pp. 115–118.

[24] A. Kachayev, D. M. Klymyshyn, S. Achenbach, and V. Saile, "High vertical aspect ratio LIGA micromachined microwave 3-dB coupler," in *Proceedings of International Conference on MEMS, NANO and Smart Systems*, Banff, Alberta - Canada, July 2003, pp. 38–43.

[25] R. S. Elliott, *An Introduction to Guided Waves and Microwave Circuits*, Prentice-Hall, Inc., New Jersey, 1993.

[26] D. M. Pozar, "Microstrip antenna aperture-coupled to a microstripline," *Electronics Letters*, vol. 21, no. 2, pp. 49–50, January 1985.

[27] C. A. Felippa, "A historical outline of matrix structural analysis: a play in three acts," *Computers and Structures*, vol. 79, no. 14, pp. 1313–1324, June 2001.

[28] O. C. Zienkiewicz and Y. K. Cheung, *The Finite Element Method in Structural and Solid Mechanics*, McGraw-Hill, London, 1967.

[29] Ansoft High Frequency Structure Simulator Manuals, *Ansoft HFSS*, Ansoft Corporation, Pittsburgh, PA, Version 3.3.25, January 2001.

[30] T. Itoh, *Numerical Techniques for Microwave and Millimeter-wave Passive Structures*, John Wiley & Sons, New York, 1989.

[31] K. J. Binns and P. J. Lawrenson, *Analysis and Computation of Electric and Magnetic Field Problems*, Pergamon Press, Oxford, New York, 1973.

[32] E. L. Ginzton, *Microwave Measurements*, McGraw-Hill, New York, 1957.

[33] K. Leong, J. Mazierska, M.V. Jacob, and D. Ledenyov, "Comparing unloaded Q-factor of a high-Q dielectric resonator measured using the transmission mode and reflection mode methods involving S-parameter circle fitting," in *IEEE MTT-S International Symposium Digest*, Seattle, WA, June 2002, pp. 1665–1668.

[34] K. Leong and J. Mazierska, "Precise measurements of the Q factor of dielectric resonators in the transmission mode - accounting for noise, crosstalk, delay of uncalibrated lines, coupling loss, and coupling reactance," *IEEE Transactions on Microwave Theory and Techniques*, vol. 50, no. 9, pp. 2115–2127, September 2002.

[35] D. Kajfez and E. J. Hwan, "Q-factor measurement with network analyzer," *IEEE Transactions on Microwave Theory and Techniques*, vol. 32, no. 7, pp. 666–670, July 1984.

[36] D. Kajfez, *Q Factor*, Vector Forum, Oxford, MS, 1994.

[37] D. Kajfez, "Linear fractional curve fitting for measurement of high Q factors," *IEEE Transactions on Microwave Theory and Techniques*, vol. 42, no. 7, pp. 1149–1153, July 1994.

[38] D. Kajfez, "Numerical determination of two-port parameters from measured unrestricted data," *IEEE Transactions on Instrument and Measurement*, vol. IM-24, no. 1, pp. 4–11, March 1975.

[39] S. P. Morgan, Jr., "Effect of surface roughness on eddy current losses at microwave frequencies," *Journal of Applied Physics*, vol. 20, 1949.

[40] C. L. Holloway and E. F. Kuester, "Power loss associated with conducting and superconducting rough interfaces," *IEEE Transactions on Microwave Theory and Techniques*, vol. 48, no. 10, pp. 1601–1610, October 2000.

[41] C. L. Holloway, "Equivalent boundary conditions for a perfectly conducting periodic surface with a cover layer," *Radio Science*, vol. 35, no. 3, pp. 661–681, May-June 2000.

[42] C. L. Holloway and E. F. Kuester, "Impedance-type boundary conditions for a periodic interface between a dielectric and a highly conducting medium,"

IEEE Transactions on Antennas and Propagation, vol. 48, no. 10, pp. 1660–1672, October 2000.

[43] A. R. Von Hipple, *Dielectric Materials And Applications*, Wiley, New York, 1954.

[44] E. Steinsland, T. Finstad, and A. Hanneborg, "Etch rate of (100), (111) and (110) single-crystal silicon in TMAH measured in situ by laser reflectance interferometry," *Sensor and Actuators*, vol. A86, no. 1-2, pp. 73–80, October 2000.

[45] M. J. de Boer, J.G.E. Gardeniers, H. V. Jansen, E. Smulders, M. Gilde, G.Roelofs, J.N. Sasserath, and M. Elwenspoek, "Guidelines for etching silicon MEMS structures using fluorine high-density plasmas at cryogenic temperatures," *Journal of Microelectromechanical Systems*, vol. 1, no. 4, pp. 385–401, August 2002.

[46] S. Achenbach, *Optimization of the Process Conditions for the Fabrication of Microstructures by Ultra Deep X-Ray Lithography (UDXRL)*, Ph.D. thesis, University of Karlsruhe, 2000.

[47] M. J. Hill, R. W. Ziolkowski, and J. Papapolymerou, "Simulated and measured results from a Duroid-based planar EBG cavity resonator filter," *IEEE Microwave and Guided Wave Letters*, vol. 10, no. 12, pp. 528–530, December 2000.

[48] M. J. Hill, R. W. Ziolkowski, and J. Papapolymerou, "A high-Q reconfigurable planar EBG cavity resonator," *IEEE Microwave and Wireless Components Letters*, vol. 11, no. 6, pp. 255–257, June 2001.

[49] H. Hsu, M. J. Hill, J. Papapolymerou, and R. W. Ziolkowski, "A planar X-band electromagnetic band-gap (EBG) 3-pole filer," *IEEE Microwave and Wireless Components Letters*, vol. 12, no. 7, pp. 255–257, July 2002.

[50] T. Euler and J. Papapolymerou, "Silicon micromachined EBG resonator and two-pole filter with improved performance characteristics," *IEEE Microwave and Wireless Components Letters*, vol. 13, no. 9, pp. 373–375, September 2003.

[51] S. D. Senturia, *Microsystem Design*, Kluwer Academic Publishers, Boston, 2001.

[52] G. Matthaei, L. Young, and E. M. T. Jones, *Microwave Filters, Impedance-Matching Networks and Coupling Structures*, McGraw-Hill, New York, 1964.

[53] K. A. Zaki and C. Chen, "Coupling of non-axially symmetric hybrid modes in dielectric resonators," *IEEE Transactions on Microwave Theory and Techniques*, vol. 35, no. 12, pp. 1136–1142, December 1987.

[54] N. Marcuvitz, *Waveguide Handbook*, Massachusetts Institute of Technology, Radiation Laboratory Series, New York: McGraw-Hill, 1951.

[55] L. Lewin, *Theory of Waveguides*, Butterworth & Co., London, 1975.

[56] F. J. Pantenburg, S. Achenbach, and J. Mohr, "Characterization of defects in very high deep-etch X-ray lithography microstructures," *Microsystem Technologies*, vol. 4, no. 2, pp. 89–93, February 1998.

[57] S. Achenbach, J. Mohr, and F.J. Pantenburg, "Application of scanning probe microscopy for the determination of the structural accuracy of high aspect ratio microstructures," *Microelectronic Engineering*, vol. 53, no. 1, pp. 637–640, June 2000.

[58] Z. Ma, D. M. Klymyshyn, S. Achenbach, and J. Mohr, "LIGA cavity resonator for K-band applications," in *International Conference on MEMS, NANO and Smart Systems (ICMENS'05)*, Banff, CAN, July 2005, pp. 106–109.

[59] Z. Ma, D. M. Klymyshyn, S. Achenbach, and J. Mohr, "Microwave resonators using hard X-ray lithography," *Microwave and Optical Technology Letters*, vol. 47, no. 4, pp. 353–357, November 2005.

[60] K. J. Herrick, J. G. Yook, and L.P.B. Katehi, "Microtechnology in the development of three-dimensional circuits," *IEEE Transactions on Microwave Theory and Technology*, vol. 46, no. 11, pp. 1832–1844, November 1998.

[61] M. J. Hill, J. Papapolymerou, and R. W. Ziolkowski, "High-Q micromachined resonant cavities in a K-band diplexer configuration," *IEE Proceedings - Microwaves, Antennas and Propagation*, vol. 148, no. 5, pp. 307–312, October 2001.

[62] H.-C. Chang and K. A. Zaki, "Evanescent-mode coupling of dual-mode rectangular waveguide filters," *IEEE Transactions on Microwave Theory and Techniques*, vol. 39, no. 8, pp. 1307–1312, August 1994.

[63] X.-P. Liang, K. A. Zaki, and A. E. Atia, "Dual mode coupling by square corner cut in resonators and filters," *IEEE Transactions on Microwave Theory and Techniques*, vol. 42, no. 7, pp. 1331–1336, July 1994.

[64] J.-F. Liang, X.-P. Linag, K. A. Zaki, and A. E. Atia, "Dual-mode dielectric or air-filled ectangular waveguide filters," *IEEE Transactions on Microwave Theory and Techniques*, vol. 42, no. 7, pp. 1331–1336, July 1994.

Appendix A

Relaxation Method

An interesting use of the relaxation method is concentrated on the solving of 2-D systems that can be described by Poisson's equation

$$\frac{\partial^2 w}{\partial x^2} + \frac{\partial^2 w}{\partial y^2} + W(x, y) = 0. \tag{A.1}$$

The relaxational solution to a differential equation consists of evaluating the wanted function w at a large number of chosen points within the specified region. In two dimensions the area is subdivided by a uniform net, so that on straight lines drawn in various directions, w is calculated equally spaced at the nodes of the net. An area could be geometrically covered by the meshes having one of the three different shapes, such as square, equilateral triangle or equiangular hexagon.

Figure A.1 shows the typical point of a relaxation net. In this figure, w_0 denotes the value of w at an interior point of a square-mesh net, w_1, w_2, w_3, and w_4 are the surrounding points, and h is the distance between two adjacent nodes.

The first step in solving Equation A.1 is to replace the derivatives by finite difference approximations. The two partial derivatives in Equation A.1 can be approximated by the combinations of the terms w_0 to w_4. The function w can be expanded near $x = x_0$ in a Taylor's series as

$$\begin{aligned} w &= w_0 + \left(\frac{dw}{dx}\right)_0 (x - x_0) + \frac{1}{2!}\left(\frac{d^2 w}{dx^2}\right)_0 (x - x_0)^2 \\ &\quad + \frac{1}{3!}\left(\frac{d^3 w}{dx^3}\right)_0 (x - x_0)^3 + \frac{1}{4!}\left(\frac{d^4 w}{dx^4}\right)_0 (x - x_0)^4 + \cdots, \end{aligned} \tag{A.2}$$

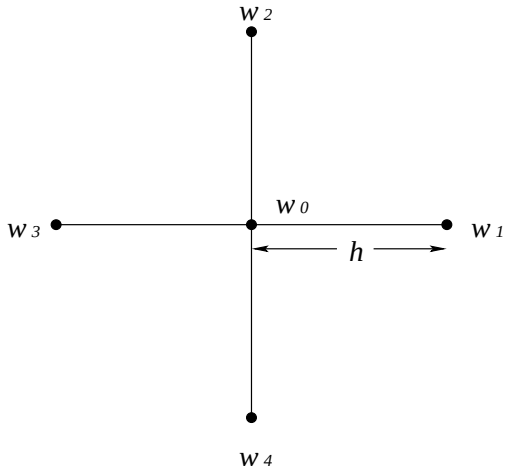

Figure A.1 Typical point of a relaxation net.

By substituting $w_1 = x + h$ and $w_3 = x - h$, the Taylor expansions at node 1 and 3 are obtained as

$$w_1 = w_0 + h\left(\frac{dw}{dx}\right)_0 + \frac{h^2}{2}\left(\frac{d^2w}{dx^2}\right) + \frac{h^3}{6}\left(\frac{d^3w}{dx^3}\right) + \frac{h^4}{24}\left(\frac{d^4w}{dx^4}\right)_0 + \cdots , \tag{A.3a}$$

$$w_3 = w_0 - h\left(\frac{dw}{dx}\right)_0 + \frac{h^2}{2}\left(\frac{d^2w}{dx^2}\right) - \frac{h^3}{6}\left(\frac{d^3w}{dx^3}\right) + \frac{h^4}{24}\left(\frac{d^4w}{dx^4}\right)_0 + \cdots . \tag{A.3b}$$

Adding these two equations together, the terms containing odd order of h are cancelled out. The summation becomes

$$w_1 + w_3 = 2w_0 + h^2\left(\frac{d^2w}{dx^2}\right) + O(h^4) , \tag{A.4}$$

where $O(h^4)$ is a term that containing the forth, sixth, and higher powers of h. This term becomes small enough to be ignored for a suitable small h, which is the distance between two adjacent nodes. By neglecting this quantity and rearranging

the equation, the finite-difference approximation to $(d^2w/dx^2)_{x_0}$ is derived as

$$h^2 \left(\frac{d^2w}{dx^2} \right)_{x_0} = w_1 + w_3 - 2w_0 \ . \tag{A.5}$$

Similarly, the approximation to the second derivative of w with respect to y is

$$h^2 \left(\frac{d^2w}{dy^2} \right)_{y_0} = w_2 + w_4 - 2w_0 \ . \tag{A.6}$$

Substituting Equation A.5 and A.6 into A.1, the Poisson's equation can be approximated at a typical node 0 by

$$\sum_{n=1}^{4} w_n - 4w_0 + h^2 W_0 = 0 \ , \tag{A.7}$$

in which there is an error of $O(h^4)$, and the effect of the error diminishes with the mesh interval h. The values of w's at each group of five nodes must satisfy Equation A.7 in order to get the solution to the corresponding differential equation. Otherwise, there exists a non-zero residual R_0, which is expressed as

$$R_0 = \sum_{n=1}^{4} w_n - 4w_0 + h^2 W_0 \ . \tag{A.8}$$

When applied to the eddy current equation, the finite difference approximation to Equation 3.87 is obtained as

$$\sum_{n=1}^{4} w_n - 4w_0 \left(1 + \frac{jh^2}{2\delta^2} \right) = 0 \ . \tag{A.9}$$

The relaxation method of solving Equation 3.87 starts by superimposing a square grid on the cross section of the desired region, as shown in Figure 3.14. First, a solution is assumed at each node of the given net, which satisfies the boundary conditions. Then the residual is calculated according to Equation A.8 at each node, which has the value zero for the boundary nodes, and R_0 for the internal

nodes. The node with the greatest residual value is found, and a modification is made to the corresponding w_0 to reduce this error. By doing this, the residuals at the immediately adjacent points are simultaneously changed. The desired solution would be obtained by successive corrections at the point where the residual is the largest until the residuals at all points are less than a given quantity. Theoretically there exists a set of w's for which the residual reaches zero. But in most numerical analysis algorithms, some limit of tolerance is adopted, and the analysis process is regarded as finished when all the error is below that value.

As an example of solving the 2-D region in Figure 3.14, the mesh interval is chosen to be $h = \frac{1}{2}\delta$. Representing w by a complex number as $w = u + iv$, the residual is found to be

$$R = (2\sum_{n=1}^{4} u_n - 8u_0 + v_0) + j(2\sum_{n=1}^{4} u_n - u_0 - 8v_0) \tag{A.10}$$

which is obtained by multiplying the left side of Equation A.9 by 2 to clear out the fractions.

The residual of the boundary nodes has the value of zero, and the error function R for all the internal nodes follows Equation A.10. It is apparent that changing the value w_0 of an internal node will affect the error function of itself as well as all adjacent internal nodes. Derived from the Equation A.10, the residuals are altered with respect to w_0 according to the following scheme

$\triangle w_0$	$\triangle R_0$	$\triangle R_{1,2,3,4}$
$+1$	$-8-j$	$+2$
$+j$	$+1-j8$	$+2j$

If w_1 or w_3 lies on one of the lateral boundaries of symmetry, then the corresponding $\triangle R$ is doubled, because the change in w_0 os reflected on the other side of the boundary.

The determination of when the computations are finished depends on the minimum correction accepted in w. For example, if w is regarded accepted with the

error between ± 0.5, then both the real and imaginary part of the residuals,defined by Equation A.10, should not exceed ± 4. By correction of the elements with the greatest residual values repeatedly, a set of solution for the whole 2-D cross section can be obtained.